



Copyright Undertaking

This thesis is protected by copyright, with all rights reserved.

By reading and using the thesis, the reader understands and agrees to the following terms:

1. The reader will abide by the rules and legal ordinances governing copyright regarding the use of the thesis.
2. The reader will use the thesis for the purpose of research or private study only and not for distribution or further reproduction or any other purpose.
3. The reader agrees to indemnify and hold the University harmless from and against any loss, damage, cost, liability or expenses arising from copyright infringement or unauthorized usage.

IMPORTANT

If you have reasons to believe that any materials in this thesis are deemed not suitable to be distributed in this form, or a copyright owner having difficulty with the material being included in our database, please contact lbsys@polyu.edu.hk providing details. The Library will look into your claim and consider taking remedial action upon receipt of the written requests.

**THIN FILM TRANSITION METAL CHALCOGENIDE
BASED GAS SENSORS**

NG NGAI HANG

M.Phil

The Hong Kong Polytechnic University

2018

The Hong Kong Polytechnic University

Department of Applied Physics

**Thin Film Transition Metal Chalcogenide
Based Gas Sensors**

NG Ngai Hang

*A thesis submitted in partial fulfillment of the
requirements for the Degree of Master of Philosophy*

June 2017



Certificate of originality

I hereby declare that this thesis is my own work and that, to the best of my knowledge and belief, it reproduces no material previously published or written, nor material that has been accepted for the award of any other degree or diploma, except where due acknowledgement has been made in the text.

_____ (Signature)

NG NGAI HANG (Name of candidate)



Abstract

This project was carried out to extend the scope of studies in investigating dynamic sensing mechanism and gas sensing properties of transition metal chalcogenides with photo-assisted technique.

Dynamic gas sensing mechanism of nanocluster-assembled ZnSe film under

UV illumination

Dynamic gas sensing mechanism was studied using the sensing result of oxygen on nanocluster-assembled ZnSe film. The film was fabricated using Supersonic Cluster Beam Deposition (SCBD) method followed by post-selenization. It was characterized by Raman spectroscopy, UV-Vis spectroscopy and XRD. AFM images of nanocluster-assembled ZnSe film show a porous morphology which plays critical role in gas sensing. The time-dependent conductivity σ_{ph} and gas sensor response S to oxygen at various concentrations were measured at different operation temperature. The sensor responses measured under UV illumination are varies from 306.2 to 0.3 when oxygen concentration increases from 0.01 % to 20 % at room temperature and from 177.4 to 1.7 when oxygen concentration increases from 0.02 % to 10 % at 80 °C. Results are well fitted to the proposed model derived by the sum of two exponential time-dependent terms. This model incorporated the mechanisms of photo generation and recombination of electron-hole pairs, adsorption and desorption of oxygen, and ionization of adsorbed oxygen. The rate constants and coefficients used in the model revealed the gas sensing details about the



change of the relative contribution of individual mechanisms, which vary with oxygen concentration and temperature. More precise of sensing response could be predicted according to the proposed model.

Gas sensing properties of nanocluster-assembled, multilayer and monolayer

MoS₂ films

Gas sensing properties of different structures of MoS₂ were studied. Large-area monolayer MoS₂ film was successfully produced using a one-step reactive DC magnetron sputtering. The crystalline and uniform monolayer film was obtained from the processes using a reactant gas containing 9 % H₂S in Ar, a substrate temperature of 500 °C with 3 °C/min ramping down to room temperature, a sputtering pressure of 15mTorr and deposition time of 25 min. Achievement of the desired MoS₂ phase was confirmed by Raman spectroscopy and XRD analysis. Indirect-to-direct bandgap transition was detected by PL spectrum at 1.91 eV. The film thickness was found to be reduced to monolayer of about 0.61 nm according to the XS-TEM image. Multilayer MoS₂ film was produced using sputtering of the same setting but a longer deposition time of 60 min, while nanocluster-assembled MoS₂ film was produced using SCBD method followed by post-sulfurization.

The dark sensor response of monolayer MoS₂ against 10 – 500 ppm H₂S is 1.25 - 25.68 %, while those of multilayer and nanocluster-assembled MoS₂ films are small and close to zero. Besides, photo-assisted monolayer MoS₂ film exhibits an enhanced gas sensor response of 4.04 - 52.07 % against H₂S varying in the same concentration range. It is also sensitive to 10 – 500 ppm NH₃ with



the sensor response of 53.8 - 247.4 %. In contrary, the sensor response to H₂ is weaker, and is found to change slightly of 0.4 - 6.3 % for 40 – 500 ppm. These results indicated that only monolayer MoS₂ film with a direct bandgap can give remarkable enhanced gas sensor response to H₂S, which are found to be symbiotic.



Publication List

1. **Ngai Hang Ng, Chung Wo Ong, Man Hon Wong, Meng Zhao, Ka Sheng Lau, "Gas sensing properties of nanocluster-assembled, multilayer and monolayer MoS₂ films" Sensors and Actuators B: Chemical (In press).**
2. **Ngai Hang Ng, Chung Wo Ong, Xu Ming Zhang, "Study of dynamic photo induced oxygen adsorption-desorption mechanisms of nanocluster-assembled ZnSe films", European Materials Research Society, Strasburg, spring 2017, France.**
3. **Meng Zhao, Man Hon Wong, Chung Wo Ong, Ngai Hang Ng, Hau Chung Man, "Tunability of Pd-nanogapped H₂ sensors made on SiO₂-coated Si micropillar arrays", Sensors and Actuators B: Chemical, (2017).**
4. **Man Hon Wong, Ngai Hang Ng, Meng Zhao, Ka Seng Lau, Hau Chung Man, Jeffery T. Cheung, and Chung Wo Ong. "Room-temperature polymer-coated supersonic cluster beam deposited ZnO film for O₂ gas and dissolved O₂ sensing." Sensors and Actuators B: Chemical (2017).**



Acknowledgements

I would like to express my special thanks of gratitude to my chief supervisor Dr. C.W. Ong, for his invaluable guidance and inspiration throughout my master degree study. I am grateful to his kindly support during the progress of my project that enriched my fundamental knowledge in both research and academic aspects. I also like to thank my co-supervisor Dr. Xuming Zhang for providing valuable suggestions and his cares.

Sincerely to my team colleagues, Mr. Man Hon Wong and Mr. Ka Seng Lau who pinpoint keen insights and complement own expertise with each other. Their supports over fabrication and measurement allowed me to move forward my work schedule. Special thanks to the support by Dr. Meng Zhao, from Jiangsu Key Laboratory of Micro and Nano Heat Fluid Flow Technology and Energy Application in School of Mathematics and Physics at Suzhou University of Science and Technology, who supplied the required substrates for my study. I am grateful to Mr. Wang Fa Cheng i, Mr. Hon Fai Wong and Ms. Sheung Mei Ng for their help and discussion when the research was ran into difficulties.

This research was funded by University Grant Committee (UGC) of Hong Kong Special Administrative Region, the People's Republic of China. Without this funding, this project will not able to be initiated and go smoothly. I am thankful to the equipment supported by Material Research Center (MRC) and the Department of Applied Physics in the Hong Kong Polytechnic University.

As last, I would like to dedicate this thesis to the by family, who encourage and show understanding to me to pursue a higher degree study.



Table of Contents

Certificate of originality	i
Abstract.....	ii
Publication List.....	v
Acknowledgements	vi
Table of Contents	1
List of Figure	xii
List of Table	xvii
Chapter 1 Introduction	1
1.1 Overview of gas sensor industry.....	1
1.2 Review of gas sensors	2
1.3 Trend of gas sensor design.....	4
1.3.1 High surface-to-volume ratio.....	4
1.3.2 Property of atomic layer thick material.....	4
1.3.3 Resistance to poisoning of sensor element.....	5
1.3.4 Low operating temperature with photo-assist.....	5
1.4 Aims and objective.....	7
Chapter 2 Background	9
2.1 Definitions of working parameters of gas sensors.....	9
2.2 Gas sensing materials	11



2.3	Gas sensing mechanism	13
2.3.1	Receptor function	13
2.3.2	Transducer function.....	15
2.3.3	Operation mode	18
2.4	Models of gas sensing mechanism	24
2.4.1	Temperature-dependent model.....	24
2.4.2	Grain size-dependent model	26
2.4.3	Time-dependent model.....	27
2.5	Adsorption and desorption mechanism	28
2.5.1	Adsorption Energy	28
2.5.2	Adsorption Models	29
2.6	Transition metal chalcogenide	35
2.6.1	Zinc selenide (ZnSe).....	36
2.6.2	Molybdenum disulphide (MoS ₂)	36
Chapter 3	Experimental Methods	39
3.1	Sample fabrication	39
3.1.1	Supersonic Cluster Beam Deposition (SCBD)	40
3.1.2	Post-chalcogenization and annealing	43
3.1.3	Reactive DC magnetron sputtering.....	45
3.1.4	More information on substrate selection and cleaning	47



3.2	Characterization	49
3.2.1	Raman spectroscopy.....	49
3.2.2	Photoluminescence (PL) spectroscopy	49
3.2.3	UV-VIS spectroscopy.....	50
3.2.4	X-Ray diffraction (XRD)	51
3.2.5	X-Ray reflectivity (XRR)	51
3.2.6	Transmission electron microscopy (TEM).....	52
3.2.7	Atomic force microscopy (AFM)	52
3.3	Gas sensing measurement.....	53
3.3.1	Measuring system.....	53
3.3.2	Gas sensing measurement cycle.....	55
Chapter 4	Dynamic gas sensing mechanism of nanocluster-assembled ZnSe film under UV illumination	58
4.1	Gas sensing mechanism	58
4.2	Nanocluster-assembled ZnSe film	60
4.2.1	Material selection.....	60
4.2.2	Material characterization	60
4.3	Theoretical modeling of gas sensing mechanism	65
4.3.1	Dynamic of carrier and hole density	65
4.3.2	Derivation of dynamic (time-dependent) photoconductivity	66



4.4	Experimental results and theoretical analysis	75
4.4.1	Dynamic (time-dependent) photoconductivity at room temperature	75
4.4.2	Dynamic (time-dependent) photoconductivity at 80 °C.....	81
Chapter 5	Gas sensing properties of nanocluster-assembled, multilayer and monolayer MoS ₂ films	87
5.1	Porous nanocluster-assembled MoS ₂ film.....	88
5.1.1	Surface morphology	88
5.1.2	Confirmation of the formation of the MoS ₂ compound	89
5.2	Multilayer and monolayer MoS ₂ films	90
5.2.1	Effect of H ₂ S content in the reactant gas.....	90
5.2.2	Substrate temperature	92
5.2.3	Sputtering pressure	95
5.2.4	Reduction of deposition time for reducing film thickness	97
5.3	Gas sensing properties of MoS ₂ films	101
5.3.1	H ₂ S sensing properties of MoS ₂ films	101
5.3.2	UV-assisted sensing of monolayer MoS ₂	103
Chapter 6	Conclusion	107
6.1	Summary	107
6.1.1	Study of dynamic gas sensing model.....	107
6.1.2	Gas sensing properties of MoS ₂ film	110



6.2	Further work	112
6.2.1	Improvement of gas sensing model	112
6.2.2	Gas sensing with other TMD material	113
6.2.3	Design of gas sensor	113
	Reference	115



List of Figure

Figure 2-1 Schematic diagram of receptor function and electron band energy due to surface adsorption of oxidizing (upper) and reducing gas (bottom).	15
Figure 2-2 Grain size effect on transducer function.	18
Figure 2-3 Temperature dependence of the sensor response of SnO ₂ sensor with different catalysts against H ₂ , CO, CH ₄ and C ₃ H ₈	20
Figure 2-4 Enhanced gas adsorption capacity under photoexcitation on the sensor's surface.	21
Figure 2-5 Enhanced redox reaction under photoexcitation on the sensor's surface.	22
Figure 2-6 Band-to-band transition in direct and indirect bandgap semiconductor.	23
Figure 2-7 Temperature dependent gas sensing model.	25
Figure 2-8 Adsorption energy against the distance from sensor's surface.	29
Figure 2-9 Temperature dependence of chemisorption and physisorption rate.	29
Figure 2-10 Potential theory of multilayer gas adsorption.	31
Figure 2-11 Adsorption mechanism under five different situations.	35
Figure 3-1 Schematic diagram of the configuration of a Supersonic Cluster Beam Deposition (SCBD) setup.....	41
Figure 3-2 Bombardment of the target by accelerated Ar ions.....	42
Figure 3-3 AFM image of nanocluster SCBD Mo film prepared with discharge voltages of 800 V (left) and 500 V (right).	43



Figure 3-4 Schematic diagram of the configuration of the furnace used for post-chalcogenization and annealing process.45

Figure 3-5 IDE patterned on SiO₂/Si substrate used for preparing MoS₂ films for electrical measurements.47

Figure 3-6 IDE pattern made on SiO₂/Si substrate and its dimensions.48

Figure 3-7 Sample holder of the gas sensing measurement system.....54

Figure 3-8 Software interface of the gas sensing measurement system.54

Figure 3-9 A typical measurement cycle for examining the oxygen sensing mechanism of nanocluster-assembled ZnSe film.....56

Figure 3-10 A typical measurement cycle for examining the gas sensor response of MoS₂ films against reducing gases.57

Figure 4-1 AFM images of an as-deposited nanocluster-assembled Zn metal film (left) and a post-selenized nanocluster-assembled ZnSe film (right).....61

Figure 4-2 Raman spectrum of as-deposited SCBD Zn and post-selenized SCBD ZnSe film.62

Figure 4-3 XRD spectrum of post-selenized SCBD ZnSe film.63

Figure 4-4 UV-VIS absorption spectrum of a post-selenized SCBD ZnSe film and the Tauc plot with $n=1/2$64

Figure 4-5 Schematic diagram of dynamic interactions involving photo generated electrons and holes, surface sorption and ionization of oxygen species under UV illumination.....66

Figure 4-6 (a, b) Recombination and adsorption rate constants k_r and k_A against oxygen concentration, (c, d) recombination and adsorption coefficients A_0 and A_1 against $1/k_r$ and $1/k_A$, respectively.74



Figure 4-7 Room-temperature photoconductivity of nanocluter-assembled SCBD ZnSe films measured at various oxygen concentrations.79

Figure 4-8 Estimated saturated photo response of nanocluster-assembled SCBD ZnSe films against various oxygen concentrations measured at room temperature.....79

Figure 4-9 (a) Charge carrier recombination rate constant k_r (b) adsorption-desorption rate constant k_A against oxygen concentration, (c) coefficient A_1 against $1/k_r$ and (d) coefficient A_2 against $1/k_A$ measured at room temperature.80

Figure 4-10 Photoconductivity of nanocluster-assembled SCBD ZnSe films against various oxygen concentrations measured at 80°C.83

Figure 4-11 Estimated saturated photo response of nanocluster-assembled SCBD ZnSe films against various oxygen concentrations measured at 80 °C.....83

Figure 4-12 (a) Charge carrier recombination rate constant k_r (b) adsorption-desorption rate constant k_A against oxygen concentration, (c) coefficient A_1 against $1/k_r$ and (d) coefficient A_2 against $1/k_A$ measured at 80 °C.84

Figure 4-13 Schematic diagram of gas sensing and adsorption-desorption mechanisms controlling the gas detection process. (a-c) grain size effect (d-f) transition of adsorption models (g-h) Ionization.85

Figure 5-1 AFM image of as-deposited SCBE Mo nanoclusters film over an area of 1 μm x 1 μm (top) and 500 °C post-sulfurized nanocluster-assembled MoS_2 film over an area of 500 nm x 500 nm (bottom).89

Figure 5-2 (a) Raman and (b) XRD spectra of as-deposited SCBD Mo film and the same film after post-sulfurization at 500 °C.....90



Figure 5-3 Raman spectra of MoS₂ films deposited with various H₂S concentration from 0 % to 9 % in argon.....92

Figure 5-4 (a) Raman and (b) XRD spectra of MoS₂ films deposited at various T_s from 300 to 700 °C. Insets: FWHM of Raman peaks and lattice spacing of the (002) planes.94

Figure 5-5 AFM image of a) substrate, b) MoS₂ film without ramping, and c) with ramping deposited at P_s=15 mTorr and T_s=500 °C.95

Figure 5-6 (a) Raman and (b) XRD spectra of MoS₂ films deposited at various P_s from 5 to 25 mtorr. Insets: FWHM of Raman peaks and lattice spacing of the (002) planes.96

Figure 5-7 (a) XRR spectra and (b) deposition rate of MoS₂ films deposited at various P_s from 5 to 25 mtorr.....97

Figure 5-8 (a) Raman and (b) photoluminescence spectra of MoS₂ films deposited with various deposition times from 60 min to 15 min at. C_{H₂S} = 9 %, T_s = 500 °C and P_s = 15 mtorr.98

Figure 5-9 Cross-section XS-TEM image of the monolayer MoS₂ film.....100

Figure 5-10 Energy dispersive X-ray spectroscopy (EDX) analysis of the monolayer MoS₂ film sample obtained using the TEM system.....100

Figure 5-11 Normalized photoconductivity response of nanocluster, multilayer and monolayer MoS₂ measured at ambient condition.101

Figure 5-12 Dark electrical conductivity of (a) nanocluster-assembled MoS₂ film for 30 – 500 ppm H₂S (b) multilayer MoS₂ film for 40 – 500 ppm H₂S (c) monolayer MoS₂ for 10 – 500 ppm H₂S at 80°C and (d) repeatability of the sensor response of monolayer MoS₂ against 100 ppm H₂S.103



Figure 5-13 Photo-assisted electrical conductivity of monolayer MoS₂ for (a) 10 – 500 ppm H₂S at 80 °C (b) 10 – 200 ppm NH₃ at 80 °C and (c) 40 – 2800 ppm H₂ at 80°C.105

Figure 5-14 Dark sensor response of (a-c) nanocluster, multilayer, and monolayer MoS₂ films against H₂S, and (d-f) photo-assisted sensor response of monolayer MoS₂ film against H₂S, NH₃ and H₂ at 80 °C.106



List of Table

Table 1-1 Comparison among different types of gas sensor.	2
Table 2-1 Chemical and electronic sensitization caused by addition of catalyst on the surface of an SnO ₂ gas sensor.....	19
Table 2-2 Models of gas sensing mechanism.	24
Table 2-3 Adsorption models.....	30
Table 2-4 Material properties of ZnSe, Multilayers MoS ₂ and Monolayer MoS ₂ .	36
Table 2-5 Summary of different synthesis methods for producing a few layers to monolayer MoS ₂	38
Table 3-1 Target and powder materials used for sample fabrication.....	39
Table 3-2 Reactant gases used in sputtering and gas sensing measurements....	40
Table 3-3 Optimized parameters of the SCBD processes using Zn and Mo targets.	43
Table 3-4 Comparison of various sputtering methods for producing ultrathin atomic-layer MoS ₂ films.....	45
Table 3-5 Types of bandgap and transition with respect to different values of n.	51
Table 4-1 Lists of parameters used for describing the mechanisms of photo-assisted oxygen sensing properties of nanocluster-assembled ZnSe films at room temperature and 80°C.	85



Chapter 1 Introduction

1.1 Overview of gas sensor industry

Human beings are insensible to odorless hazardous gases such as carbon monoxide and methane by merely using their own olfaction. This causes difficulties for them to escape from dangers in some types of workplaces such as coal mines. In the old days before effective gas sensors have been invented, mineworkers brought along with flame lights or canaries when they went into coal mines. They were used as sentinels for alerting mineworkers whenever flammable and toxic gases started to emerge in the workplaces. However, these measures are not good enough to prevent accidents from happening. One reason is that the lead time between notification and fatal disaster is usually very short. Along with increasing complexity of production processes in industrial aspect, more kinds of hazardous gaseous are used and produced. They can potentially cause serious pollution in broad areas to long-lasting threats and dangers to the public. These gaseous chemicals may even include greenhouse gases, which may become one of the causes for climate change.

As a consequence, many kinds of gas sensor were invented to meet the demand on preventing from hazard. The harmfulness of hazardous gases to human beings is further recognized. Many industrial regulations on gas safety have been set up. Standards such as OSHA, NIOSH or ACGIH have been implemented by industries and organizations in many countries. Many gas emission ordinances and global agreements were established, such as Oslo Protocol, Kyoto Protocol and the latest Paris Agreement for further reducing emission of gaseous pollutants into the air.



Furthermore, for solving the problem of exhaustion of fossil fuels in the coming future, activities for exploiting methane clathrate stored in shale and asteroid mining have become active. The problem of how to detect and prevent accidental leakage of hazardous gases to the atmosphere will be a new challenge. This foreseeable problem further motivates more material scientists and industries to look for new sensor materials for improving the present gas sensing technology.

1.2 Review of gas sensors

Many gas sensing techniques are referring to physiochemical principles. Gas sensors can be classified into different types depending on their operation principles. They can be classified into electrochemical, catalytic, optical and chemoresistive types of sensors. The specific features of different types of the sensor are summarized in Table 1-1.

	<i>Electrochemical</i>	<i>Catalytic</i>	<i>Optical</i>	<i>Chemoresistive</i>
Method	Chemical reaction	Catalytic oxidation	Photo absorption / Reflectometry etc.	Gas adsorption
Sensitivity	High	High	High	High
Selectivity	Good	Poor	Excellent/Good	Poor
Response time	Fast	Fast	Fast	Fast
Size	Medium	Medium	Large	Small
Lifetime	Short	Medium	Medium	Long
Cost	Medium	Low	High	Low

Table 1-1 Comparison among different types of gas sensor.

Electrochemical type gas sensor has high sensitivity and good selectivity. They are based on electrical signal from chemical reactions between electrolyte (or electrodes) and detected gas. However, electrolyte could be contaminated when used. The lifetime is limited to be around 1-2 years.



The operation of a catalytic type gas sensor is based on the oxidizing reaction between the target gases and sensing element which is usually heated up to high temperature. Some oxygen should be present in the detected area for sustaining the oxidation process. This type of gas sensor is highly sensitive to and has been widely used for detection of explosive and flammable gases. However, the function of the sensor would deteriorate once the sensing element or catalyst is poisoned.

Optical type gas sensor is designed to work on different mechanisms. One of them is based on analyzing an optical absorption spectrum of the detected gas molecules using light beam directly. Another type of optical gas sensor is based on detecting the change of optical property of the sensing material caused by adsorption of or reaction with the target gas. A common drawback of optical gas sensors is that the whole setup is expensive and bulky. However, the sensing performance of this type of sensors is excellent of a high sensitivity, high selectivity and fast response time.

The first breakthrough of gas sensing technology using chemoresistive semiconductor was demonstrated by Seiyama in 1960s¹. He measured the electrical response of ZnO film caused by reaction with toluene and propane at 485°C. He found that the resistance of other metal oxide semiconductors was sensitive to some gases as well. The finding quickly opened up a new approach of gas sensing technology. The mechanism of chemoresistive gas sensor is closely related to surface adsorption of target gas molecules. This process causes charge transfer between the sensor material and the gas molecules to result in a change of resistance. Device setup is simple and the production cost is low. It is thereby very popular in a variety of applications². Further technique such as adding noble metal



as catalyst improving the gas sensing performance is commonly used^{3,4}. In this project, chemoresistive type gas sensors were used.

1.3 Trend of gas sensor design

Researchers in the area of gas sensor technology constantly work on better material composition and structural architecture for improving the gas sensing performance. The following aspects are particularly concerned in the development of chemoresistive type gas sensors

1.3.1 High surface-to-volume ratio

Reducing the thickness of sensor element, or the grain size of polycrystalline film or cluster size of porous film can increase the film's surface-to-volume ratio. The sensor response is expected to be enhanced because of the following reasons: (i) the dynamic range of the variation of electrical conductivity is significantly enlarged when the volume fraction of the depletion region can be increased to be close to the total volume of the sensor, (ii) necking of the conduction path at the contact among adjacent clusters in a cluster-assembled film sensor occurs, and (iii) the time for gas molecules to diffuse across the sensing region is shortened. These considerations motivate us to select ultra-thin and porous films as samples in this study.

1.3.2 Property of atomic layer thick material

Nowadays, the thin film can be fabricated to have thicknesses controlled to atomic level. 2-dimensional materials in form of layer structure, such as graphene and MoS₂, exhibit different physical, optical and electrical properties from those of



the bulk materials when the thickness is reduced to single layer. The gas sensing properties of the material may also be affected significantly. This opens up a new area of gas sensor research.

1.3.3 Resistance to poisoning of sensor element

In many applications, the detector may be required for long-period monitoring of target gas. This may result in dissociation of the sensor material and the catalyst. In particular, metal oxide semiconductor based gas sensor usually work at elevated temperature and hence are more vulnerable to poisoning effect. The sensor may be unreliable and have short life time. One direction for getting better chemical sensors of reactive gases containing S, Se and Te is to use a sensor material containing the same chalcogen element. One example implemented in this study is to use MoS₂ sensor to detect H₂S, where S is the element in common on both sides. This approach may help to reduce the instability caused by reaction with target gas.

1.3.4 Low operating temperature with photo-assist

High operating temperature around several hundred °C is commonly required to activate the sensing mechanism in a chemoresistive sensor. However, the high temperature working condition could shorten the lifetime of the sensor. The sensor's performance would degrade much faster than the case when it is set to operate at room temperature. Besides, desorption of adsorbed gas molecule is also enhanced by rising temperature. Hence, the sensor response is also reduced once the operation temperature is over the optimum point. In addition, the high operation temperature required to be maintained and stabilized, thermal drift of the output is more likely to be a problem such that calibration is needed from time



to time.

In order to compensate the energy gain by heat in conventional chemoresistive sensor, photo-assist with above-bandgap illumination is used in gas sensor working at low temperature or even at room temperature. The drawbacks of thermal-assisted gas sensor can be alleviated to some extent.



1.4 Aims and objective

This project is aimed at investigating dynamic sensing mechanism and gas sensing properties of transition metal chalcogenides with photo-assisted technique.

Below are the objectives to achieve:

i. Synthesize porous nanocluster-assembled films using Supersonic Cluster Beam Deposition (SCBD)

Zinc selenide (ZnSe) and molybdenum disulfide (MoS_2) nanocluster-assembled films with high porous structures are synthesized by SCBD. We want to examine whether the expected large surface area-to-volume ratio of the sensor can markedly influence the gas sensing properties.

ii. Synthesize large-area monolayer MoS_2 film using reactive DC magnetron sputtering

We also aimed at synthesizing large-area uniform monolayer MoS_2 using PVD-based technique to examine the influence of band transition to gas sensing performance. The fabrication of MoS_2 film was conducted by reactive DC magnetron sputtering. The condition of the process for achieving monolayer MoS_2 film was optimized by adjusting the reactant gas, operating temperature, sputtering pressure and deposition time.

iii. Modeling the dynamic (time-dependent) photoconductivity response to oxygen of ZnSe film

To demonstrate the interaction between adsorption-desorption of the detected gas molecules and charge exchange mechanism of photo-assisted gas sensor, we derive a dynamic (time-dependent) model of photoconductivity response. It is applied to analyze the measurement



result of oxygen detection in nanocluster-assembled ZnSe film.

iv. Evaluate the gas sensing properties of MoS₂ films

We study the sensor response of monolayer MoS₂ film, multilayer MoS₂ film and nanocluster-assembled MoS₂ film to H₂S, H₂ and NH₃. Experiments in dark and under above-bandgap UV light illumination are designed. The observed results will be explained based on the influences of the nano-scaled structural features and indirect-to-direct band transition of MoS₂ films.



Chapter 2 Background

2.1 Definitions of working parameters of gas sensors

In this section, we summarize the definitions of important working parameters used for describing the performance of a gas sensor⁵.

- **Sensor response, S**

Sensor response is defined as the fractional change of output signal (e.g. resistance, electrical conductivity etc.) generated upon exposure to the detected gas. If the initial value of a physical quantity of the sensor is σ_0 and its new value in the detected gas is σ_s , the sensor response is:

$$S = \frac{\sigma_s - \sigma_0}{\sigma_0}$$

- **Sensitivity, $\partial S/\partial C$**

Sensitivity is defined as the change of sensor response per unit change of detected gas concentration C at a specific level of C .

- **Selectivity**

Selectivity is defined as the capability of resisting the interference leading to erroneous signal due to the coexistence of the gases other than the target one in the detected area.

- **Stability/Repeatability**

Stability/Repeatability is defined as the capability of sensor to maintain a stable sensing performance, (including sensor response, sensitivity, selectivity, response, and recovery time etc.) within an acceptable tolerance when working in either static mode or cyclic mode.



- **Detection limit**

Detection limit is defined as the maximum or minimum detectable concentrations of target gas before the sensor response get saturated or unresponsive.

- **Dynamic range**

Dynamic range is defined as the range of detectable gas concentration within the detection limit.

- **Linearity**

Linearity is defined as the degree of proportional proximity between the sensor response and detected gas concentration.

- **Resolution**

Resolution is defined as the minimum resolvable change of gas concentration detectable by the sensor.

- **Response/recovery time**

Response/recovery time is defined as the time interval for the sensor response to reach/recover 90% of the total change of the response.

- **Working temperature**

Working temperature is defined as the temperature setting for the sensor element to exhibit the desired sensing performance.

- **Hysteresis**

Hysteresis is defined as the deviation between the tracks of sensor response recorded in the loading and unloading processes in the test cycle.



- ***Life cycle***

Life cycle is defined as the duration or cycles of a sensor before malfunction.

2.2 Gas sensing materials

The above gas sensor performance indexes strongly depend on the properties of the sensing materials^{6,7}. Important factors associated with the sensing materials used are summarized as follows.

- ***Electronic structure***

Metal oxides are widely used for gas sensing. One of the reason is that the metal in the oxide structure could exhibit various oxidation states⁸. The d-orbital electronic configuration of metal is susceptible to perform oxidation or reduction. Metal oxides with d^0 or d^{10} configuration (such as ZnO, SnO₂ and TiO₂) were found to be good gas sensor materials because they can only work as oxidizing or reducing substance respectively during the gas detection. However, in general, most of these oxides have large bandgap and stable. The free charge carrier concentration at room temperature for reacting with detected gas is small. This feature results in weak interaction between the detected gas and the sensor material and hence this kind of sensor response required thermal assist. Metal with d^1 to d^9 configuration may perform reduction and oxidation which has less sensor response than d^0 and d^{10} . However, their surface physiochemical properties and the feasibility of being highly catalyzed making them to be very attractive in sensor applications. Noted that transition metal chalcogenide



exhibit certain similarity to metal oxide material. In particular some of them are found to exhibit indirect-to-direct electronic bandgap transition at monolayer thickness. In the present study, we focused on the transition metal chalcogenide materials with direct bandgap, ZnSe and MoS₂, to explore the photo-assisted technique in gas sensing effect.

- ***Dopant***

Doping level and type of dopant elements on sensor material can affect charge carrier concentration and conduction type (n or p). This alters the electrical response of the reactant gas molecules which are adsorbed on the material surface.

- ***Crystal structure***

A sensor material could be in single crystal, polycrystalline or amorphous form. Different structure would have different grain size, concentration of grain boundaries and defects. They affect the number of adsorption site, the volume fraction of the depletion region, diffusion rate and mobility of the detected gas in the material structure. These would alter the sensor response significantly. The mechanism was discussed in section 2.3.

- ***Thickness and surface-area-to-volume ratio***

The number of adsorption site on the sensor's surface affects the sensor response which commence with adsorption mechanism. Thus, the surface-area-to-volume ratio is one of the dominant factors of sensor performance. Sensor with bulk or thick sensor material has a small ratio but low resistance, hence the dynamic range of sensor response is small but the electrical measurement would involve less electrical noise. In contrast,



sensor of small characteristic dimension result higher response. However, excessive increasing in surface-area-to-volume ratio may eliminate the dynamic range of detection as the depletion layer would readily occupies whole film and cause no necking effect⁹.

- ***Composite sensor materials***

A sensor with a hetero-nanostructure could exhibit synergistic effect to result in improved sensing performance¹⁰.

- ***Environment***

Many environmental conditions have significant influences on the sensor performance. For example, moisture in the environment can be adsorbed on the sensor's surface and reduces the efficiency of gas adsorption. Increase in the working temperature can alleviate the influence of moisture by evaporation and activate the reaction between the detected gas and sensor material. Another important example is above-bandgap light illumination on a semiconductor sensor, which can increase photo generated electrons and holes to result in significant change in the gas sensing properties of the device.

2.3 Gas sensing mechanism

In general, the working principle of chemoresistive gas sensor is based on three major aspects. They are (i) receptor function, (ii) transducer function and (iii) operation mode^{11,12}. The key concepts of each item are summarized in this section.

2.3.1 Receptor function

Receptor function is referred to the reaction between the detected gas and the

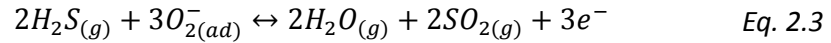


sensor material. For a semiconductor-based chemical sensor, the sensor's surface adsorbs gas molecules and usually involves oxidization and reduction. Figure 2-1 shows the receptor processes schematically conducting on the sensor's surface by oxygen and H₂S detection as examples. The adsorbed oxygen can be ionized when they absorb enough activation energy from the sensor material. This process is referred to chemisorption. Accumulation of charge on the sensor's surface generates a space charge region and change of electron band energy. The reaction leading to chemisorbed oxygen radicals can be expressed as:



Electron trap states at energy level E_t which is below the conduction band energy level E_C , is created. These localized states may accommodate some amount of electrons. The electrical conductivity of the sensor element is reduced as a consequence. On the other hand, a self-bias electric field is built up and generates a depletion region which represented by Debye length λ_D . The variation of Debye length with the change of oxygen concentration causes further change of electrical resistivity due to the morphology of sensor material. This is referred to transducer function of which be explained in the next section.

For H₂S, detection, H₂S could be adsorbed on the sensor's surface and ionized to become radicals as similar as oxygen. However, it may react with the adsorbed oxygen radicals instead. It works as a reducing agent by providing electrons to the adsorbed oxygen radicals and produce H₂O and SO₂. Electrons originally trapped by oxygen radicals are released to the sensor material. This process can be described as:



The charge carrier concentration in the sensor material increases to result in an increase of electrical conductivity. The Debye length is narrower and lead to change of transducer function as well. However, the by-products may bias the sensor accuracy as the sensing mechanism also applied on every gases. Therefore, good ventilation and prevention of moisture in gas sensing device are required to minimize the tolerance.

The above two mechanisms produce opposite sensing signals. Which of them dominates would depend on factors like the reactivity of gas and the architectural details of the material structure.

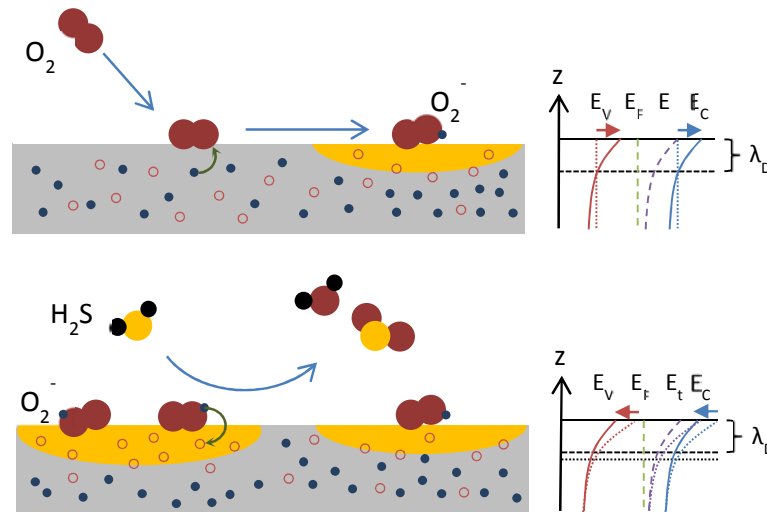


Figure 2-1 Schematic diagram of receptor function and electron band energy due to surface adsorption of oxidizing (upper) and reducing gas (bottom).

2.3.2 Transducer function

Transducer function refers to the influence of the morphology of the sensor's



structure on the receptor function. The effect is mainly from the subtle geometrical characters of the sensor element, such as the diameter of grains and film thickness. For a polycrystalline sensor element, potential barriers are generated at the grain boundaries when gas molecules are adsorbed and trap electrons at that region. In 1991, a model of grain size effect was firstly introduced to interpret the mechanism of transducer function involved in gas detection¹³. The dominant mechanism of resistive-type gas sensing process depends on the relative dimensions between the Debye length λ_D (which also depends on detected gas concentration) and diameter of grain D as shown in Figure 2-2. Three cases are specified as follows.

- $D \gg 2\lambda_D$

When the grain size is much larger than the depletion region or happened at a very low detected gas concentration, the depletion region cannot penetrate throughout a grain. The intergranular potential barrier is thereby determined by the physical condition of the grain boundary only such as density of lattice mismatch and defects. These factors are the intrinsic properties of the material and are not related to the detected gas concentration. The resistive response in this case is caused by the grain boundary control and the receptor function due to gas adsorption.

- $D > 2\lambda_D$

When the grain size is just larger the depletion region, the depletion region can extend from the bulk surface to reach the intergranular region among the grains. The gain and the lateral width of intergranular potential barrier are thereby affected by the adsorption of detected gas molecules. The charge carriers require higher energy to cross over the potential barrier and



hence the overall electrical conductivity of the sensor element would decrease. The sensor working at this case is under neck control. The resistive sensor response due to this mechanism would be changed more readily by detected gas concentration.

- $D \leq 2\lambda_D$

When the grain size is smaller than the depletion region or happened at a very high detected gas concentration, most of the grains are completely depleted. The gain of potential energy to intergranular and inner-grain potential is the same. The intergranular potential barrier is thereby unaffected by further adsorption of detected gas molecules. The height of potential barrier is ultimately controlled by the grain size. The resistive response is under saturation and only very low response to detected gas concentration due to receptor function.

In summary, the resistive response could be maximized by realizing the condition of $D > 2\lambda_D$. Therefore, for detecting ultra-low concentrated gas, a polycrystalline gas sensor of smaller average grain size is preferred. In contrast, the gas sensing properties of a single crystal or an amorphous sensor are mainly dominated by the receptor function. The performance of resistive response may be different from the polycrystalline ones¹⁴.

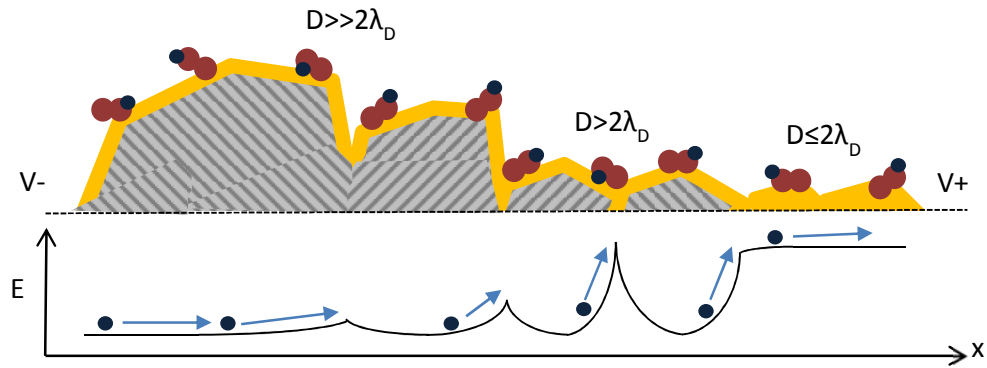


Figure 2-2 Grain size effect on transducer function.

2.3.3 Operation mode

The operation mode of a gas sensor represents the working condition of the device, which determines the dynamic behavior of the sensor through adjusting its receptor and transducer functions. For instance, sensitivity and selectivity of a sensor can be adjusted and improved by catalytic effect, thermal- and photo-excitation^{15,16}. These effects are summarized as follows.

Catalyst

Catalytic effect on gas sensing have been widely studied since the chemoresistive gas sensing effect was discovered^{3,4,17-19}. A small amount of noble metal such as palladium or platinum is dispersed on the surface of sensor material. The catalyst acts as an activator or sensitizer. The catalytic reactions and related chemical-electrical interactions are summarized in Table 2-1²⁰⁻²².

The catalyst acts to activate and spillover the adsorbed reducing gases. Redox reaction changes the adsorbed gas concentration at the sensor's surface and the oxidation state of metal respectively. The reaction rate is accelerated to result in a change of the sensor response.

Figure 2-3 gives an example showing the change of the gas sensing properties of SnO₂ sensor for different temperature settings and catalysts⁴. It shows clearly that the sensor response against H₂, CO, CH₄ and C₃H₈ is adjustable according to the working temperature and the types of noble metals added on the SnO₂ sensor's surface.

Type	Chemical	Electronic
Model		
Role of metal	Activation and spill-over of sample gas	Electron donor or acceptor
Origin of gas-sensitive properties	Change of adsorbed oxygen concentration	Change of oxidation state of metal
Example	Pt-SnO ₂	Ag ₂ O-SnO ₂ , PdO-SnO ₂ , CuO-SnO ₂

Table 2-1 Chemical and electronic sensitization caused by addition of catalyst on the surface of an SnO₂ gas sensor²².

Thermal energy

Change of sensor response due to absorption of thermal energy can be explained by two mechanisms. First, energy is required to activate redox reaction between reducing and adsorbed oxidizing gas molecules, such that the reducing gas concentration can be reflected on sensor response. Many redox reactions cannot conduct at room temperature, so that the sensor can be increased its sensor response by heated up to suitable operation temperature²³. Second, heating results in desorption of gas molecules and moisture from the surface. Physisorbed gases are desorbed first due to low adsorption energy. The sensor response would be increased because of the enhanced reactions with the chemisorbed gas molecules.

However, further increase in the working temperature would cause desorption of the chemisorbed gases. The sensor response would be decreased. For example, as shown in Figure 2-3, the sensor response of a SnO₂ sensor for a reducing gas increases with increasing temperature at first, and then drops with further increase in temperature.

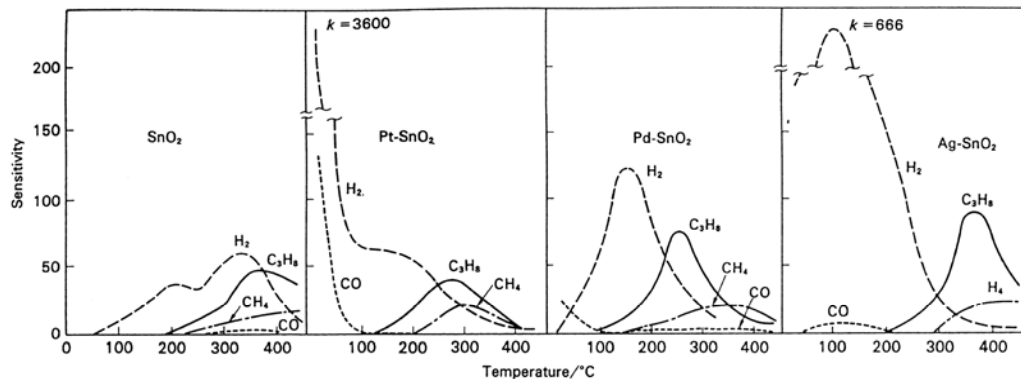


Figure 2-3 Temperature dependence of the sensor response of SnO₂ sensor with different catalysts against H₂, CO, CH₄ and C₃H₈⁴

Photoexcitation

Illuminating a semiconductor with above-bandgap photon energy generates electron-hole pairs. The increase in charge carrier concentration enhances the conductivity. Reports showed that the gas sensor response of ZnO thin film at room temperature can be enhanced by exposing it to pulsed laser^{24,25}. This phenomenon are explained by two hypothesizes. It is firstly suggested that the isothermal adsorption capacity of reactant gas on semiconductor can be increased by photoexcitation shown in Figure 2-4^{26,27}. Charge carrier concentration on the material surface is increased by light, and the photoexcited electrons enhance

adsorption and ionization of gas molecules on the sensor's surface.

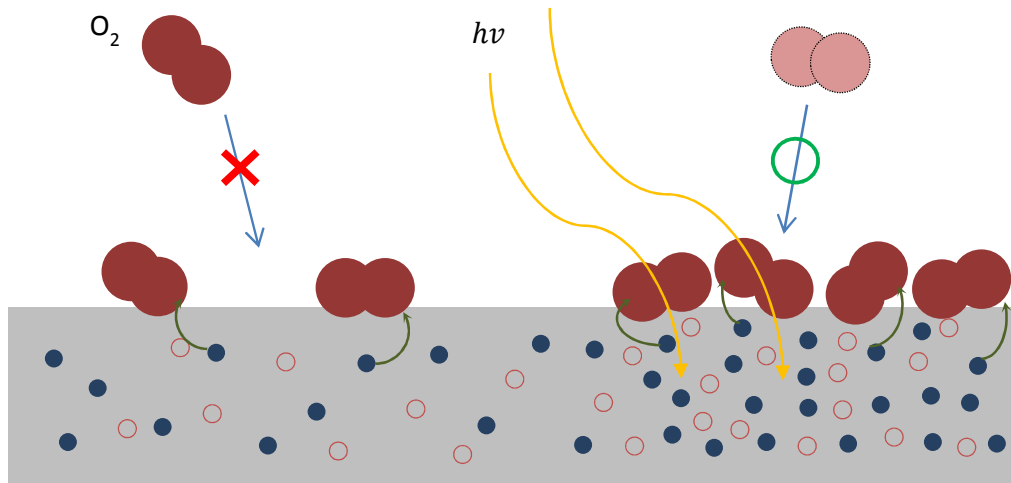


Figure 2-4 Enhanced gas adsorption capacity under photoexcitation on the sensor's surface.

Another hypothesis is that the adsorbed gas molecules are more readily ionized due to photoexcitation. The photon generates charge carriers to accelerate charge exchange by enhancing ionization and deionization of the chemisorbed oxidizing gases²⁸. The photon energy also provides sufficient energy to activate the redox reaction between reducing gas and adsorbed oxidizing gas. Figure 2-5 shows the ionization and deionization of chemisorbed gas under photo illumination. The reaction rate is increased and hence the sensor response is increased.

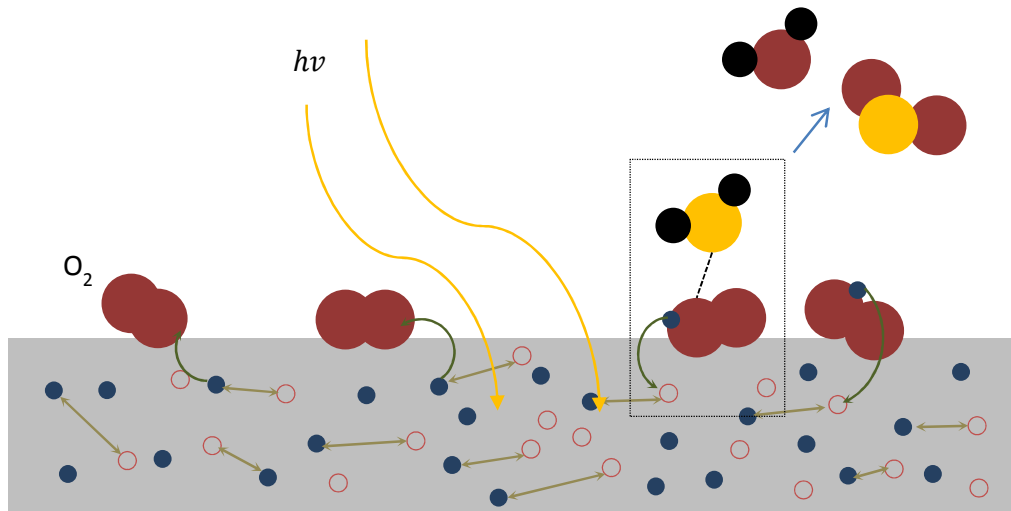


Figure 2-5 Enhanced redox reaction under photoexcitation on the sensor's surface.

Gas sensor with photo-assist has enhanced sensor response. Direct bandgap semiconductor sensor is preferred because the photo generation of electrons can be more effective under light illumination. As shown in Figure 2-6, light induced transition of an electron from the valence band to the conduction band in a direct bandgap structure only needs to obey the condition of the energy conservation, but the one in an indirect bandgap structure needs to obey conservation of both energy and crystal momentum and hence is less efficient.

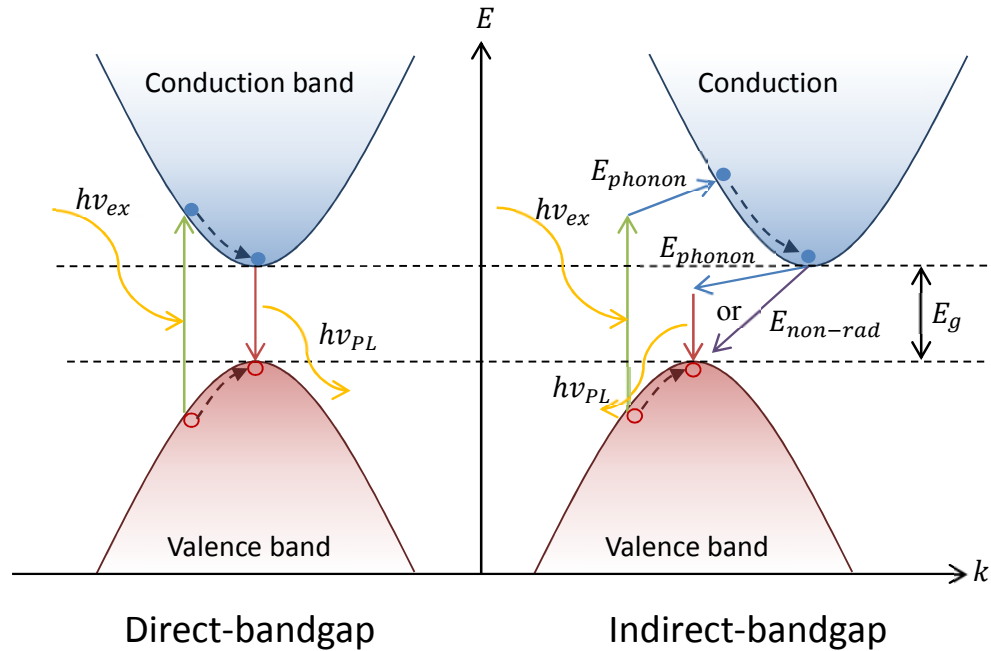


Figure 2-6 Band-to-band transition in direct and indirect bandgap semiconductor.

Lifetime of carrier $\tau(N)$ under recombination depends on the electronic band structure and can be expressed as follow²⁹:

$$\frac{1}{\tau(N)} = A + BN + CN^2$$

where N , A , B and C are charge carrier density, radiative coefficient, non-radiative coefficient and Auger recombination coefficient.

Radiative recombination of electrons and holes in a direct bandgap is very fast. Photons of energy equal to the bandgap energy will be emitted. On the other hand, electrons and holes recombination via non-radiative recombination process in an indirect band structure is much slower. The process involves the generation of a phonon to obey the conservation of momentum.

According to the characteristics of the two processes, semiconductors with direct bandgap, ZnSe and MoS₂, were selected in this study.



2.4 Models of gas sensing mechanism

This section summarized several gas sensing models which have been used to describe the influence of some factors to the gas sensing performance of a gas sensor. Table 2-2 lists some cases with the respective influencing factor. The influence in the first two cases is through the transducer function. The results of the last two cases are empirical. In each case, there is just one influencing factor, and hence is not applicable to more complicated case in general. We aim at building up a more complete model for explaining our measurements results.

Model domain	Basis	Equation
Temperature ³⁰	Transducer function	$\sigma = \sigma_0 e^{-\frac{E_F - E_{t_0} + kT \ln \frac{N_0}{N_F} + \frac{(kT)^2}{E_0} \ln(ac)}{kT}}$ Eq. 2.4
Grain size ¹¹	Transducer function	$\sigma = \begin{cases} \sigma_0 e^{-\frac{q^2 N_F^- R^2}{2\epsilon\epsilon_0 kT}}, & \text{when } D > 2\lambda_D \\ \sigma_0 e^{-\frac{k_B (R)}{k(2\lambda_D)}}, & \text{when } D \leq 2\lambda_D \end{cases}$ Eq. 2.5
		Eq. 2.6
Grain size ³¹	Receptor function	$\sigma \propto \frac{1}{V} \int n(r) dV$ Eq. 2.7
Temperature ³²	Empirical	$\sigma = \frac{\sigma_0}{\left(1 + A_1 c^{1/2} e^{-\frac{E_1}{kT}}\right)} + c^{1/4} A_2 e^{-\frac{E_2}{2kT}}$ Eq. 2.8
Time ³³	Empirical	$I(t) = \int_0^\infty F(r) e^{-rt} dr$ Eq. 2.9
		$I = I_0 + I_1 e^{-\frac{(t-t_0)}{\tau}^\beta}$ Eq. 2.10

Table 2-2 Models of gas sensing mechanism.

2.4.1 Temperature-dependent model

A temperature-dependent gas sensing model was introduced in late 80s of the last century³⁰. This model is based on the transducer function of gas sensing mechanism. It is not applicable to the case of $D > 2\lambda_D$. Neck control at the contact regions among the grains dominates the gas sensing process as shown in Figure 2-7.

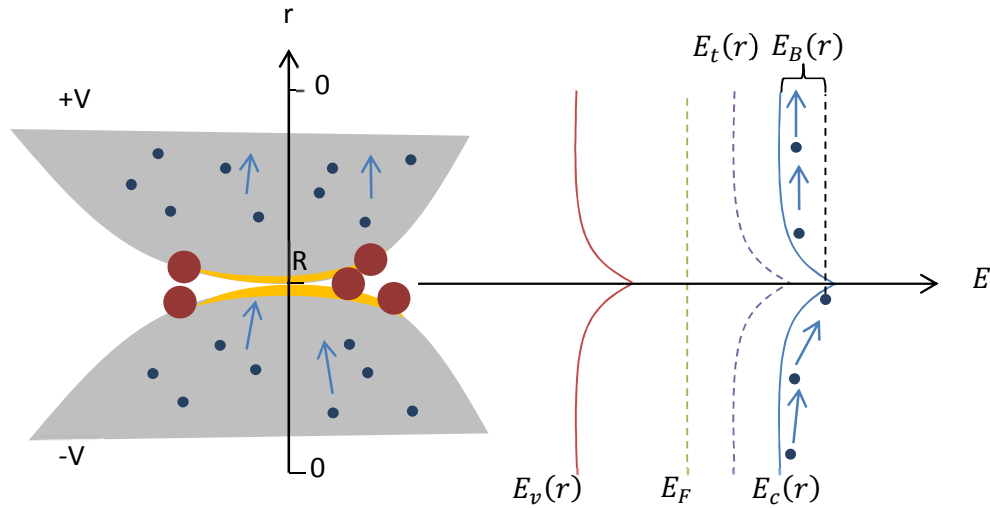


Figure 2-7 Temperature dependent gas sensing model.

In this model, a potential barrier generated at the intergranular region due to detected gas adsorption. The barrier height is a function of the radius R of the contact area. The electrical conductivity of the sensor would then vary in the form of a Maxwell-Boltzmann distribution function according to the variation of $E_B(R)$ at temperature T .

$$\sigma = \sigma_0 e^{-\frac{E_B(R)}{kT}} \quad \text{Eq. 2.11}$$

In addition, the height of the potential barrier is considered to be correlated with the number of adsorbed gas ions N_t^- . N_t^- can be expressed in terms of Energy level of trap state $E_t(R)$, the Fermi level E_F and the concentration of adsorbed gas molecules N_t by:

$$N_t^- = N_t e^{-\frac{(E_t(0)+E_B(R)-E_F)}{kT}} \quad \text{Eq. 2.12}$$

N_t can be estimated by Clifford's adsorption model³⁴:

$$N_t = N_0 (ac)^{\frac{kT}{E_0}} \quad \text{Eq. 2.13}$$

where N_0 is the number of adsorption site, a is the sensor coefficient, c is the gas



concentration, kT is the thermal energy and E_0 is the characteristic energy constant. Thus, the temperature-dependence of the electrical conductivity response to the detected gas is obtained in the form of a single exponential function:

$$\sigma = \sigma_0 e^{-\frac{E_F - E_{t_0} + kT \ln \frac{N_0}{N_t} + \frac{(kT)^2}{E_0} \ln(ac)}{kT}} \quad \text{Eq. 2.14}$$

2.4.2 Grain size-dependent model

Barsan and Weimar derived another model according to grain size effect¹¹. The model is applied to the cases of $D > 2\lambda_D$ or $D \leq 2\lambda_D$ with separated set of formulas. The derivation is similar to that of the above mentioned temperature-dependent model, but the potential barrier energy is calculated based on charge accumulation in the form of Poisson's distribution.

$$\frac{\delta^2 E_B(r)}{\delta r^2} = \frac{q^2 N_t^-}{2\epsilon\epsilon_0} \quad \text{Eq. 2.15}$$

$$E_B(R) = \begin{cases} \frac{q^2 N_t^-}{2\epsilon\epsilon_0} R^2, & \text{when } D > 2\lambda_D \\ k_B T \left(\frac{R}{2\lambda_D} \right), & \text{when } D \leq 2\lambda_D \end{cases} \quad \text{Eq. 2.16}$$

$$\text{where, } \lambda_D = \sqrt{\frac{\epsilon\epsilon_0 k_B T}{q^2 N_t^-}}$$

The electrical conductivity response of the sensor was found to be in form of Maxwell-Boltzmann distribution function *Eq. 2.11*, and hence:

$$\sigma = \begin{cases} \sigma_0 e^{-\frac{\frac{q^2 N_t^-}{2\epsilon\epsilon_0} R^2}{kT}}, & \text{when } D > 2\lambda_D \\ \sigma_0 e^{-\frac{k_B T \left(\frac{R}{2\lambda_D} \right)}{k}}, & \text{when } D \leq 2\lambda_D \end{cases} \quad \text{Eq. 2.17}$$

Noted that when $D \leq 2\lambda_D$, there is no dependency to the detected gas concentration in grain size effect anymore. Electron energy band are nearly flat and



no effective barrier can be observed³¹. Therefore, the conductivity of gas sensor is assumed to be dominated by the number of trapped charges controlled by the receptor function.

$$\sigma \propto \frac{1}{V} \int n(r) dV \quad \text{Eq. 2.18}$$

The number of carrier electron $n(r)$ can be obtained by the doping level N_D and potential barrier energy $E_B(r)$

$$n(r) = N_D e^{-\frac{E_B(r)}{kT}} \quad \text{Eq. 2.19}$$

Since the donor level N_D is equal to the number of adsorbed gas ions N_t^- , thus the conductivity can be derived.

2.4.3 Time-dependent model

An empirical model was introduced by fitting persistent photocurrent of ZnO sensor under oxygen detection³³. Decay of photocurrent $I(t)$ was derived by inverse Laplace transformation with rate constant r and weighting factor $F(r)$.

$$I(t) = \int_0^{\infty} F(r) e^{-rt} dr \quad \text{Eq. 2.20}$$

Result showed that the rate constant can vary in a very board extent over a several orders of magnitude. No distinctive exponential component can be resolved from the decaying curve of current after turning off the light. Therefore, a stretched single exponential decay function is used to fit the data, which is in the form of:

$$I(t) = I_0 + I_1 e^{\left(\frac{t-t_0}{\tau}\right)^\beta} \quad \text{Eq. 2.21}$$

Both the characteristic decay time τ and stretched power β depend on temperature and activation energy. However, this is mainly an empirical approach of analysis without giving a more fundamental explanation on the mechanism.



2.5 Adsorption and desorption mechanism

The dynamics of adsorption and desorption of gas molecules is an essential part of the whole gas sensing process. The derivation of the gas sensor model in this study involved the consideration of the adsorption mechanism. Some models are summarized as follows.

2.5.1 Adsorption Energy

The surface of a thin film gas sensor can have a strong affinity to a detected gas. As such, the gas molecules would be captured and accumulated on the surface. This phenomenon is called adsorption. In the reverse process, the adsorbed molecules are detached, and is referred to as desorption. There are two major types of adsorption processes. They are the chemisorption and physisorption as presented in Figure 2-8. These two processes involved energies falling in two different ranges, with that of the former to be higher. Chemisorption occurs at the first single-layer of the film surface, involving adsorption energy in the range of 50-500 kJ/mole. This energy level is high enough to cause charge exchange between the sensor's surface and the molecules. Chemical bonds or ionization of adsorbed gas molecule would be formed. If the gas molecule is at a farther distance from the sensor's surface, the force of interaction is much weaker and only results in Van der Waals interaction. Physisorption would take place in this situation. The adsorption energy is in the range of 5-50 kJ/mole. Although the physisorbed molecules are not ionized, the adsorption energy can still be able to affect the depletion region of the sensor.

Both kinds of adsorption processes are sensitive to thermal energy. As

chemisorbed molecule requires activation energy to initiate the chemical reaction, chemisorption is mostly endothermic and more significant with increasing operation temperature³⁵. Figure 2-9 shows that the adsorption rate of gas molecules changes with increasing temperature. For chemisorption, the adsorption rate increases first and then drops after reaching a maximum. For physisorption, it drops all the way with increasing temperature.

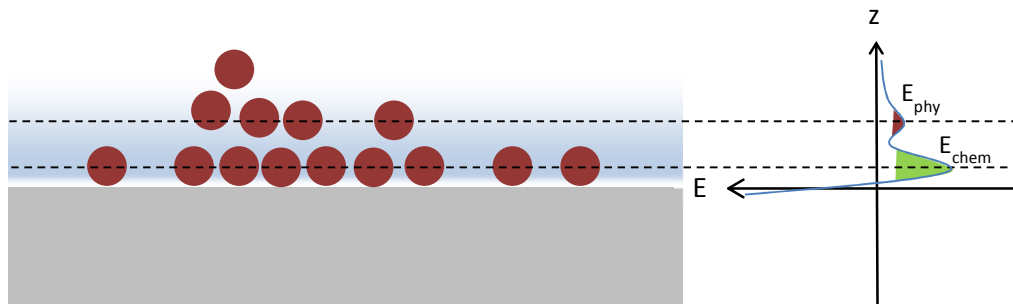


Figure 2-8 Adsorption energy against the distance from sensor's surface.

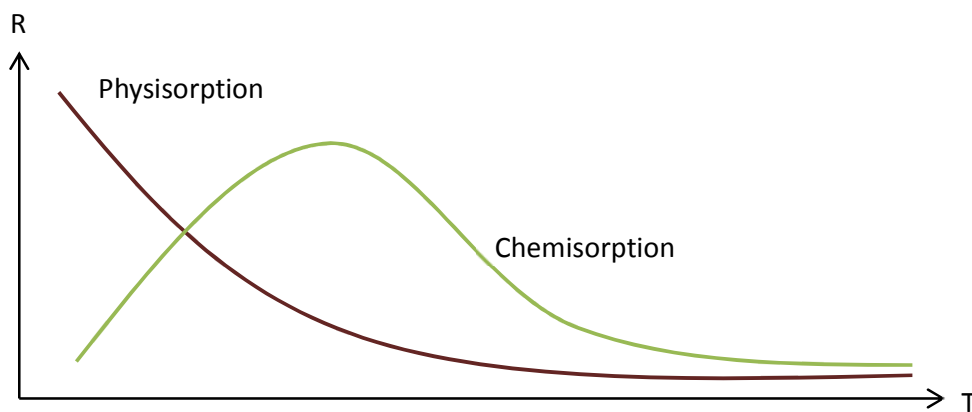


Figure 2-9 Temperature dependence of chemisorption and physisorption rate.

2.5.2 Adsorption Models

Table 2-3 lists some popular models describing the surface adsorption of gas.



They are used for evaluating the equilibrium surface coverage θ of the surface by a gas at a concentration of c . More detailed explanation for each model is given in the text³⁶.

Adsorption models	Basis	Equation
Henry's Law ³⁷	Homogeneous adsorption	$\theta = k_H c$ Eq. 2.22
Freundlich ³⁸	Empirical	$\theta = k_F c^{\frac{1}{n}}$ Eq. 2.23
Dubinin-Radushkevich ³⁹	Potential Theory ⁴⁰	$\theta = e^{-k_{DR}\epsilon^2}$ Eq. 2.24
Langmuir ⁴¹	Kinetic basis	$\theta = \frac{k_L c}{1 + k_L c}$ Eq. 2.25
BET ⁴²	Kinetic basis	$\theta = \frac{k_{BET} c}{(1 - c)[1 + c(k_{BET} - 1)]}$ Eq. 2.26

Table 2-3 Adsorption models.

Henry's Law

In this model, the desorption rate of a gas from sensor's surface is assumed to depend linearly on the concentration of adsorbed gas a , while the adsorption rate depends on the ambient concentration of the gas c . At equilibrium, the two rates are equal, such that:

$$k_d a = k_a c \quad \text{Eq. 2.27}$$

In addition, the surface coverage θ represents the ratio of the adsorbed molecule concentration a to the concentration of the adsorption sites a_0 , such that:

$$\theta = \frac{a}{a_0} \quad \text{Eq. 2.28}$$

Combining the two expressions Eq. 2.27 and Eq. 2.28, one get Henry's equation for gas adsorption isotherm as³⁷:

$$\theta = \frac{k_a}{k_d a_0} c = k_H c \quad \text{Eq. 2.29}$$

This reflects that the surface coverage of adsorbed gas is proportional to the partial



pressure of the detected gas in the ambience. Note that this model is limited to the case of homogenous adsorption, and conditions such as under adsorption site saturation and high gas concentration are not put into consideration.

Freundlich adsorption isotherm

Freundlich introduced an empirical equation to describe heterogeneous surface adsorption of a gas³⁸. The surface coverage of a gas at high concentration range is estimated by a power function.

$$\theta = k_F c^{\frac{1}{n}} \quad \text{Eq. 2.30}$$

n is a constant depending on the temperature of system, while k_F is related to the interaction between adsorbed gas and material surface. Although the equation describes the variation of gas adsorption, it is not applicable to the case of saturation at high gas concentration.

Dubinin-Radushkevich adsorption isotherm

In order to illustrate the chemisorption and physisorption in adsorption model, Eucken and Polanyi introduced a potential theory to describe the adsorption of more than one layers of gas molecules⁴⁰. The schematic plot is given in Figure 2-10 to show the equi-free energy surfaces inside the adsorbed gas layers.

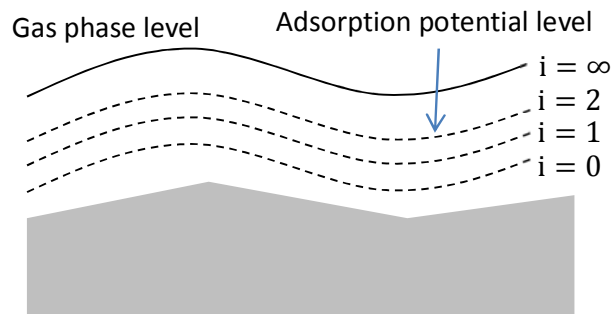


Figure 2-10 Potential theory of multilayer gas adsorption.



The adsorption potential ε_i of i^{th} layer is expressed in terms of the gas concentration c , and temperature T_i :

$$\varepsilon_i = RT_i \ln \left(1 + \frac{1}{c} \right) \quad \text{Eq. 2.31}$$

By assuming that the ratio of adsorption potential between adjacent layers is constant β :

$$\frac{\varepsilon_i}{\varepsilon_{i-1}} = \beta \quad \text{Eq. 2.32}$$

Thus, Dubinin and Radushkevich proposed an empirical exponential decay equation based on the potential theory to describe the multilayer gas adsorption of a porous material³⁹. If the affinity constant of an adsorbed gas is given as β_a and the adsorption potentials of the first and second layer are ε_1 and ε_2 , the convergence of adsorbed gas θ is derived by using the Maxwell distribution and is found to have the form of:

$$\theta = e^{-k \frac{\varepsilon_1}{\beta_a} \frac{\varepsilon_2}{\beta_a}} \quad \text{Eq. 2.33}$$

$$\theta = e^{-k \beta \frac{\varepsilon_1^2}{\beta_a^2}} \quad \text{or} \quad \theta = e^{-k_{DR} \varepsilon^2} \quad \text{Eq. 2.34}$$

However, the equation is based on a model composed of multilayer adsorption at an environment with a low gas concentration. It is not useable for single-layer adsorption situation.

Langmuir adsorption isotherm

In Langmuir's model, equations are derived based on theoretical consideration of the kinetics of gas adsorption⁴¹. This theory only considers the case of single-layer adsorption. Some assumption has been made such as the adsorbed gases would not be dislocated to adjacent adsorption sites but is desorbed from the sites.



The adsorption rate depends on the fraction of the empty adsorption sites $(1 - \theta)$ and the surrounding gas concentration c . Both adsorption and desorption rates are correlated with respective Boltzmann factors specified by the corresponding activation energies, in the form of $e^{-\frac{E}{RT}}$ and $e^{-\frac{E'}{RT}}$. At equilibrium, adsorption and desorption rate are equal:

$$k_d c (1 - \theta) e^{-\frac{E}{RT}} = k_a \theta e^{-\frac{E'}{RT}} \quad \text{Eq. 2.35}$$

The surface coverage of adsorbed gas θ is solved as:

$$\theta = \frac{k_L c}{1 + k_L c} \quad \text{Eq. 2.36}$$

where

$$k_L = \frac{k_d}{k_a} e^{-\frac{E-E'}{RT}} \quad \text{Eq. 2.37}$$

This model describes an ideal single-layer adsorption and saturation of homogeneous surface. In real situation, the activation energy and the number of adsorption site would deviate from the results of the ideal case due to the roughness of the sensor's surface.

Brunauer, Emmet and Teller (BET) adsorption isotherm

Brunauer, Emmet and Teller further derived a multilayer adsorption equation based on the Langmuir adsorption model⁴². Consider the surface coverage of each layer i , the overall surface coverage can be expressed as:

$$\theta = \frac{\sum_{i=0}^{\infty} i \theta_i}{\sum_{i=0}^{\infty} \theta_i} \quad \text{Eq. 2.38}$$

At equilibrium, the rate of desorption must be equal to the rate of adsorption between adjacent layers:



$$k_{a,i+1}\theta_i c + k_{d,i}\theta_i = k_{a,i}\theta_{i-1}c + k_{d,i+1}\theta_{i+1} \quad \text{Eq. 2.39}$$

Assume that the heat of adsorption for multilayers ΔQ_m is the same but different from that of the first layer ΔQ_0 . The ratio of the adsorption rate constant $k_{a,i}$ and desorption rate constant $k_{d,i}$ of all layers are the same except for that of the first layer adsorption.

$$\frac{k_{d,1}}{k_{a,1}} = S_0 e^{-\left(\frac{\Delta Q_0}{RT}\right)} \quad \text{Eq. 2.40}$$

$$\frac{k_{d,i}}{k_{a,i}} = S_m e^{-\left(\frac{\Delta Q_m}{RT}\right)} = g \quad \text{Eq. 2.41}$$

The correlation of surface coverage of each layer to first layer can be expressed by:

$$\theta_i = \left(\frac{c}{g}\right)^{i-1} \theta_1 = \frac{k_{d,1}}{gk_{a,1}} \left(\frac{c}{g}\right)^i \theta_0 = \frac{e^{-\left(\frac{\Delta Q_0 - \Delta Q_m}{RT}\right)}}{g_0} \left(\frac{c}{g}\right)^i \theta_0 \quad \text{Eq. 2.42}$$

$$\theta_i = k_{BET} x^i, \quad \text{where } x = \frac{c}{g}$$

where g_0 represent the entropic factor, which confines the interaction by considering the entropy change, namely:

$$g_0 = \frac{S_0}{S_m} = e^{-\left(\frac{\Delta S_0 - \Delta S_m}{RT}\right)} \quad \text{Eq. 2.43}$$

By summing up the contributions from all the layers, the surface coverage θ is:

$$\theta = \frac{\sum_{i=0}^{\infty} i\theta_i}{\sum_{i=0}^{\infty} \theta_i} = \frac{k_{BET} \sum_{i=1}^{\infty} i(x)^i}{1 + k_{BET} \sum_{i=1}^{\infty} (x)^i} = \frac{k_{BET} \left(\frac{x}{(1-x)^2}\right)}{1 + \frac{k_{BET}x}{1-x}} \quad \text{Eq. 2.44}$$

Consider the boundary condition when the gas concentration $c = 1$, there would have an infinite number of adsorption sites to be present on the sensor's surface:

$$\sum_{i=0}^{\infty} \theta_i = 1 + \frac{k_{BET}x}{1-x} = \infty, \text{ when } g = 1 \quad \text{Eq. 2.45}$$

Therefore, the result of θ obtained from the BET model is:

$$\theta = \frac{k_{BET}c}{(1-c)[1+c(k_{BET}-1)]} \quad \text{Eq. 2.46}$$

Brunauer also demonstrated five adsorption types as shown in Figure 2-11. The first type (i) represents the first layer adsorption which can be described using the Langmuir model. The second type (ii) represents multilayers adsorption after the saturation of the first layer. This process can be interpreted using the BET model. However, in some cases gas molecules could have been accumulated at higher layer while the first layer adsorption has not been saturated yet. This is defined separately as the third type of adsorption (iii) which occurs when the absorption energy for higher layers is equal or larger than the first layer. The fourth (iv) and fifth (v) types describe the effective capillary condensation phenomenon, in which that the pores are readily saturated by adsorbed molecules.

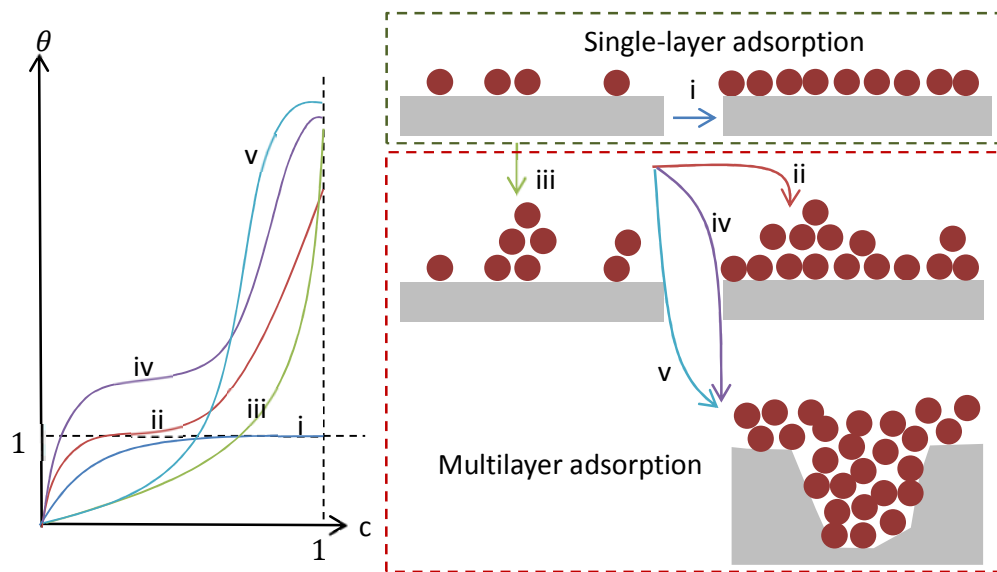


Figure 2-11 Adsorption mechanism under five different situations.

2.6 Transition metal chalcogenide

In this study, we selected gas sensing materials to aim at satisfying the requirements of two targets with photo-assist. The first is for exploring the gas



sensing mechanisms and examining whether the experimental observations can match with the predictions of some theories. Another target is to explore the gas sensing properties of two dimensional transition metal chalcogenide thin films which have emerged in the past decade but the research on their gas sensing properties is still at the early stage. Table 2-4 is an overview of the properties of the materials selected to be used in this project.

	ZnSe	Bulk MoS₂	Monolayer MoS₂
Band Transition	Direct	Indirect	Direct
Bandgap Energy	2.7 eV	1.2 eV	1.9 eV
Carrier lifetime	1-4 ns ⁴³	1 ns ⁴⁴	~50 ps ⁴⁴
Semiconductor Type	Intrinsic	Intrinsic	Intrinsic/depend on substrate ⁴⁵
Melting point	1525 °C	1185 °C	3427 °C ⁴⁶

Table 2-4 Material properties of ZnSe, Multilayers MoS₂ and Monolayer MoS₂.

2.6.1 Zinc selenide (ZnSe)

ZnSe exhibits good optoelectronic properties and has been widely used in devices such as laser diodes^{47,48} and photo detectors⁴⁹. Although it is unstable for being readily oxidized at temperature >300 °C⁵⁰, Park reported that ZnSe exhibits remarkable gas sensing properties to NO₂ when under above-bandgap photo illumination at room temperature⁵¹. Compared with another popular gas sensing material ZnO, the direct bandgap of ZnSe is narrower and the lifetime of photo-generated charge carriers is shorter⁴³. One may postulate that ZnSe could also have strong gas sensing capability due to its high carrier concentration and fast recombination rate.

2.6.2 Molybdenum disulphide (MoS₂)

MoS₂ is a widely studied TMD material because it exhibits an indirect-to-direct



bandgap transition when the thickness of the layered structure is reduced to single atomic layer. One of the important evolutions is an increase of bandgap from 1.2 eV (indirect) to 1.9 eV (direct). The mobility of ultrathin MoS₂ was found to be 200 cm²V⁻¹s⁻¹ ^{52,53}, and the current on/off ratio is as high as 1x10⁸ ⁵⁴. Bulk MoS₂ is an intrinsic semiconductor, however, monolayer MoS₂ can be n-type or p-type by proper selection of substrates⁴⁵. Significant improvement in physical, optical and electrical properties had been observed⁵⁵. These functionalities claimed to have potential applications in many aspects, including optoelectronics⁵⁶, photodetector⁵⁷ and sensors⁵⁸.

Although MoS₂ has attracted great scientific interest, production of large area uniform ultrathin or monolayer MoS₂ for large scale production is still a challenging problem. Up to date, most researchers applied mechanical/chemical exfoliation and chemical vapor deposition (CVD) for producing film samples, but they are mostly composed of flakes with lateral dimension of a few microns^{45,59-62}, which are too small to satisfy general application requirements. Studies using physical vapor deposition (PVD) are demonstrated to obtain large-area atomic-layers MoS₂⁶³⁻⁶⁶. However, most of them required post processing to get the desired stoichiometry and in most cases the samples are few monolayers thick. Table 2-5 shows the summary of synthesis methods of atomic-layers MoS₂.



Method	Precursor	Substrate	Layers	Post process
Mechanical exfoliation ⁶⁷	MoS ₂	SiO ₂ /Si	1	-
Chemical exfoliation ⁵⁹	MoS ₂	SiO ₂ /Si	5-20	-
Chemical exfoliation ⁶⁰	Li x MoS ₂	SiO ₂ /Si	1-5	-
CVD ⁶¹	MoO ₃ , S	SiO ₂ /Si	1-3	-
e-beam evaporation ⁶²	Mo, H ₂ S	SiO ₂ /Si	2-12	-
PLD ⁶³	Mo	Sapphire	2-3	Sulfurization
RFMS ⁶⁴	MoS ₂	SiO ₂ /Si	2-9	Sulfurization
DCMS ⁶⁵	Mo	Sapphire/Silica	3-4	Sulfurization
Reactive DCMS ⁶⁶	Mo, S	Sapphire	1	-

Table 2-5 Summary of different synthesis methods for producing a few layers to monolayer MoS₂.

Layered MoS₂ has been shown to show very good gas sensing effect against H₂, NO₂, NH₃ and triethylamine⁶⁸. The sensitivity was claimed to be as high as many commercial sensor products⁶⁹⁻⁷². We thereby believed that MoS₂ should have a great potential in detecting sulphur-containing reducing gases such as H₂S.



Chapter 3 Experimental Methods

3.1 Sample fabrication

Two physical vapor deposition (PVD) techniques were used to fabricate thin film samples of different structural architectures. The first is the supersonic cluster beam deposition (SCBD) followed by post-chalcogenization. It is a deposition method for producing thin film composed of nanoclusters in nano scale. The second is reactive DC magnetron sputtering, which is favorable for producing large-area uniform film samples. Table 3-1 shows the specifications of the materials used in sample preparation. Mo and Zn rods were used as the targets in SCBD process. S and Se powders were used in post-sulfurization and post-selenization processes. MoS₂ was used as the target in magnetron sputtering process. Table 3-2 shows the specifications of the gases used in gas sensing measurements. They include Ar, synthetic air, H₂S, H₂ and NH₃.

Target	Shape	Purity	Source
Mo	3mm Rod	99.99%	China New Metal Material Technology Co. Ltd.
Zn	3mm Rod	99.99%	
S	Powder	99.99%	
Se	Pellet	99.99%	
MoS ₂	2" plate	99.5%	HeFei Ke Jing Material Technology Co. Ltd.

Table 3-1 Target and powder materials used for sample fabrication.



Gas	Concentration	Balanced gas
Ar	99.999 % UHP	N/A
Synthetic Air	21 % O ₂	N ₂
H ₂ S	9 %	Ar
H ₂	3.78 %	Ar
NH ₃	1 %	Ar

Table 3-2 Reactant gases used in sputtering and gas sensing measurements.

3.1.1 Supersonic Cluster Beam Deposition (SCBD)

In a SCBD process, a low energy and low degree of coalescence deposition technique is used for creating nano-sized clusters. The SCBD system consists of three chambers, i.e. pulsed microplasma cluster source (PMCS) chamber, expansion chamber and deposition chamber. Figure 3-1 shows the schematic diagram of an SCBD system. The background pressure was 1×10^{-6} torr. A Mo or Zn rod target was mounted in the PMCS chamber. High pressure argon (Ar) gas pulses were jetted on the target surface at certain frequency. Meanwhile, electric pulses with the same repetition rate of the gas pulses were applied to the target with a phase shift. Microplasma was generated on the target surface to ablate the material from it. The ablated species aggregate and condense to form nanoclusters. The nanoclusters were carried by the Ar flow to enter the expansion chamber. The gas flow in the expansion chamber experiences a supersonic expansion and passes through an aerodynamic filter set. The nanoclusters beam is then collimated to become a fine aligned stream. The nanoclusters of lighter masses will be scattered and be removed. The selected nanoclusters continue to proceed and enter the

deposition chamber. In this chamber, the nanoclusters are deposited on a quartz substrate of dimensions of 10 mm x 5 mm x 1 mm. A nanocluster-assembled porous film is thus produced.

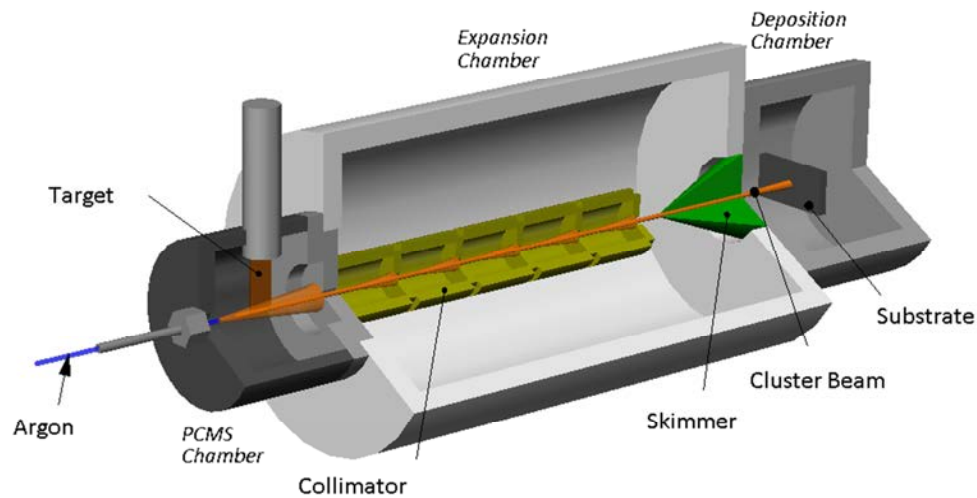


Figure 3-1 Schematic diagram of the configuration of a Supersonic Cluster Beam Deposition (SCBD) setup.

The size of nanoclusters is expected to be one of the most important parameters affecting the gas sensing properties, and hence is particularly concerned in this project. The nanocluster size produced in SCBD process varies with the settings of processing parameters. The formation of the nanoclusters in SCBD is based on the bombardments of Ar ions in the microplasma on the cathode target. The energy and momentum transfer of the Ar ions bombarding on the target are expected to affect the size of the nanoclusters.

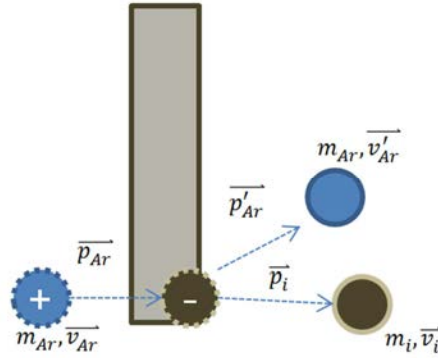


Figure 3-2 Bombardment of the target by accelerated Ar ions.

Figure 3-2 illustrates the physical process of ion bombards on the target surface. Based on the principle of conservation of energy in collision problem, the total energy and momentum in the process remain unchanged. The average kinetic energy gained by argon ions E_{Ar} is the sum of kinetic energy of the gas and electrical potential energy due to the attraction by the cathode:

$$\Delta E_{Ar} = \frac{3PV}{2n} + qV_E$$

Hence, it is predicted that the average kinetic energy of sputtered nanoclusters would decrease if the pressure and voltage drop. High enough pressure is required to ensure that the nanoclusters can move fast enough during the supersonic expansion process. Hence, the applied voltage is the only factor which can modulate the size of nanoclusters.

Figure 3-3 shows the AFM images of as-deposited Mo nanoclusters produced with the applied peak voltages at 800 V and 500 V. The size of nanoclusters was found to drop by about half, namely from 76 – 110 nm to 34 – 44 nm. This indicates that the use of lower discharge voltage is required for producing smaller nanoclusters, which are more desired for making a sensor with a larger

sensor response. Further decrease of discharge voltage for a Mo target will not provide sufficient energy for plasma formation in PCMS chamber. Therefore, similar to Zn, we fixed the minimum discharge voltage throughout the study to obtain minimum size of nanoclusters. The value of the parameter is shown in Table 3-3.

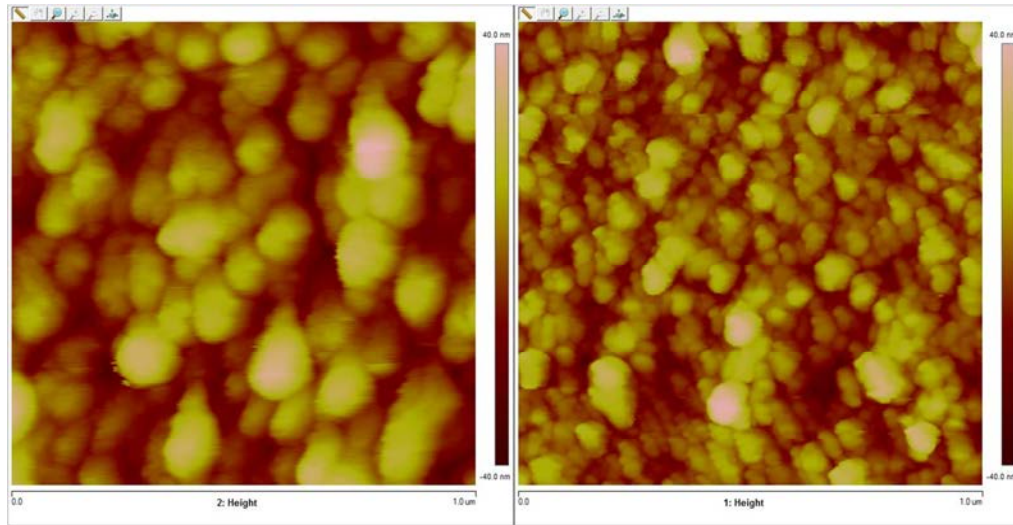


Figure 3-3 AFM image of nanocluster SCBD Mo film prepared with discharge voltages of 800 V (left) and 500 V (right).

	Zn	Mo
<i>Pulse frequency</i>	4 Hz	2 Hz
<i>Peak voltage</i>	800 V	500 V
<i>Electric pulse width</i>	120 us	80 us
<i>Ar gas pressure</i>	2.25×10^4 torr	2.25×10^4 torr
<i>Ar gas pulse width</i>	372 us	277 us

Table 3-3 Optimized parameters of the SCBD processes using Zn and Mo targets.

3.1.2 Post-chalcogenization and annealing

The as-deposited SCBD films consist of metal nanoclusters, so that chalcogenization must follow. Since SCBD is a low energy deposition technology, the nanoclusters are loosely packed. Their connection is supposed to be based on very



weak van der Waals force. Annealing of chalcogenized films enhance the crystallization and connection among the nanoclusters. This may help to improve the functional properties of film, including the desired photo-assisted gas sensor response.

Configuration of the tube furnace used for post-chalcogenization of metal films is shown in Figure 3-4. The quartz tube was set to have two separated heat zones and evacuated for removal of oxidizing gases. A continuous flow of 30sccm Ar gas was then admitted into the tube using a mass flow controller. The pressure in the quartz tube was maintained at a constant level of 200 mTorr. Chalcogen source was heated up to the melting point (Sulphur: ~ 120 °C; Selenium: ~ 190 °C) in the first heat zone to generate vapor of chalcogen source.

For selenization of nanocluster-assembled ZnSe films, one considers that the melting point of Zn is low. Hence, the SCBD Zn film in the second heat zone was first heated at 300 °C with a ramp rate of 3 °C per min. The selenization process lasted for 60min. The film was then further annealed at 500 °C for 30 min which refer to the condition used by Garcia⁷³.

For sulfurization of nanocluster-assembled MoS₂ film, one considers that the undesired product of sulfides which has lower melting point, like MoS, can be created. Hence, sulfurization of Mo film was conducted at high temperature of 500 °C for 30 min.

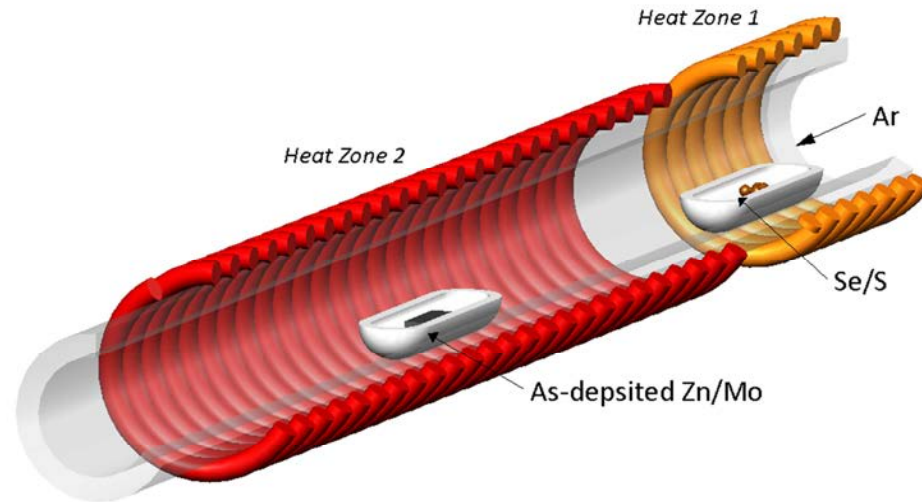


Figure 3-4 Schematic diagram of the configuration of the furnace used for post-chalcogenization and annealing process.

3.1.3 Reactive DC magnetron sputtering

Sputtering was used for synthesizing large-area uniform MoS_2 films. Table 3-4 shows a comparison of different sputtering techniques. High-power impulse magnetron sputtering (HIPIMS) was not used, because it involves energetic bombardments which may cause defects in the deposited film. Reactive DC magnetron sputtering has the low and flexible bombardment energy and hence is chosen for this study.

	DC	HIPIMS	RF	Pulsed-RF
Target	Conductive material	Conductive and insulating material	Conductive and insulating material	Conductive and insulating material
Bombardment Power	Low – High	Extremely high	medium	High
Deposition rate	Fast	Fast	Slow	Slow

Table 3-4 Comparison of various sputtering methods for producing ultrathin atomic-layer MoS_2 films.



A 2-inch MoS₂ plate with low resistance of <50 ohm was used as target for DC sputtering. We notice that dissociation of the MoS₂ material during sputtering may affect the composition of the as-deposited film. Therefore, we introduced H₂S into the sputtering chamber to aim at supplement the sulfur content of the film. We hope to obtain as-deposited film of the desired structure through a one-step reactive sputtering process.

During the sputtering process, the chamber was first evacuated to a background pressure of 10⁻⁶ Torr. H₂S in Ar gas was then admitted into the chamber. The flow was fixed at 10 sccm. Interdigitated electrodes (IDE) on SiO₂/Si substrate shown in Figure 3-5 was used to reduce the resistance of specimen for easing electrical measurements. We tried to find out the best condition for producing large-area and uniform MoS₂ film from multilayer to monolayer. The first parameter to be investigated was the H₂S gas concentration. It was varied from 0 % to 9 % for adjusting the S content in MoS₂ film. The second parameter to be optimized is the substrate temperature. It was varied from 300 °C to 700 °C. Other than crystallization property, the setting of substrate temperature is expected to affect the film flatness and possibly the internal stresses of film. The substrate was cooled down with a ramp rate of 3 °C per min after the end of sputtering process to prevent accumulation of thermal stresses and subsequent cracking of the film. The third parameter is the sputtering pressure which was varied from 5 mTorr to 35 mTorr. At last, the deposition time was adjusted to vary the thickness of MoS₂ film over a range of 60-15 min covering atomic layer thickness level. The combinations of reactive gas concentration, substrate temperature, sputtering pressure, power and deposit time were optimized in the trial runs in section 5.2 in Chapter 5.

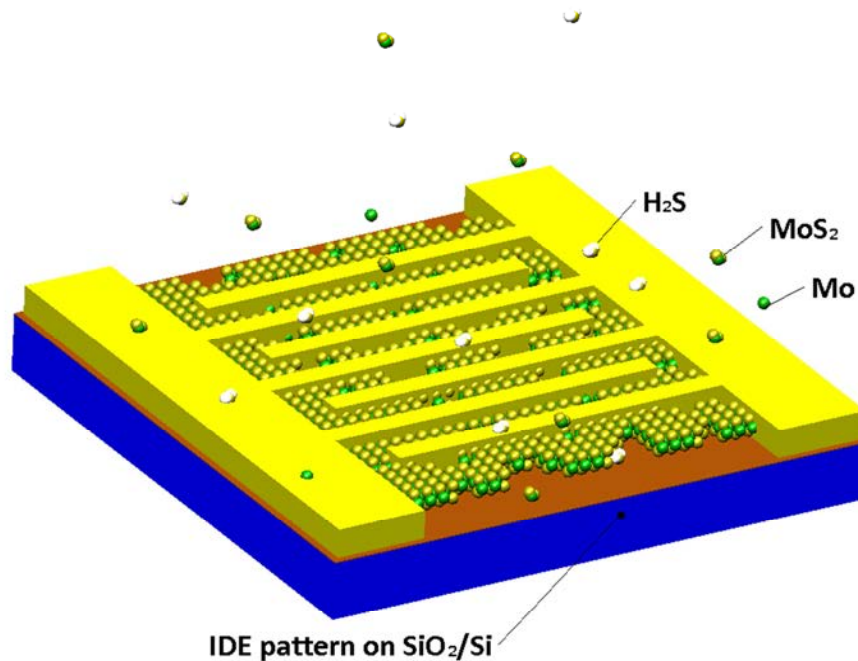


Figure 3-5 IDE patterned on SiO₂/Si substrate used for preparing MoS₂ films for electrical measurements.

3.1.4 More information on substrate selection and cleaning

Two kinds of substrates were used for deposition, quartz plate and SiO₂/Si wafer patterned with interdigitated electrodes (IDE).

Quartz plate is a common electrical insulating material and is transparent over a wide range of light wavelength from few hundreds to thousand nanometers. It is convenient to measure the deposited film electrical and optical properties on quartz with little substrate interference. Electrodes were added simply by painting silver pastes at diagonal edges of film.

On the other hand, thin film or atomic layer thick MoS₂ film has high resistance and impedance. It would be a problem for effective electrical measurements. Therefore, SiO₂/Si wafers patterned with IDE with narrow electrodes was used. The

IDE pattern was designed and fabricated in the Jiangsu Key Laboratory of Micro and Nano Heat Fluid Flow Technology and Energy Application in School of Mathematics and Physics at Suzhou University of Science and Technology. As shown in Figure 3-6, the IDE pattern has 50 pairs of fingers, each having a length of 2.5 mm and a width of 10 μm . The gap between two adjacent fingers is 15 μm .

All substrates were cleaned with the same process. First, it was soaked in acetone and cleaned with an ultrasonic cleaner for 30min. Second, the solvent was replaced by ethanol and cleaned with ultrasonic for additional 30 min. The solvents were renewed several times to remove the dirt attached to substrate during the process. Finally, the substrate was dried with dry Ar gas and stored in vacuum chamber for further uses.

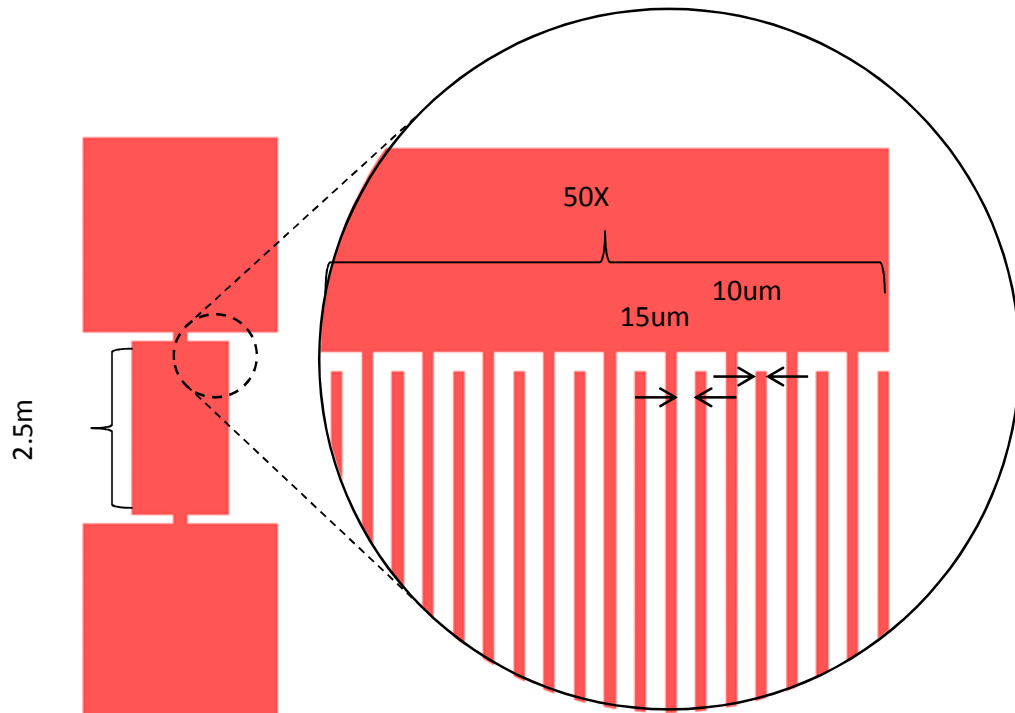


Figure 3-6 IDE pattern made on SiO_2/Si substrate and its dimensions.



3.2 Characterization

3.2.1 Raman spectroscopy

Raman spectroscopy was used to observe the energy absorption by the vibration of molecule's bond. Results can be used to identify the chemical formula and microstructure of the specimen. Moreover, the change of band structure due to the presence of internal stresses or any other conditions could also be detected.

In our study, a Horiba Jobin Yvon H800 Raman spectrometer was used to carry out the measurements. The exciting light source of the system is monochromatic diode laser giving a 50 mW 488 nm blue light. A grating of 1800 slit was selected and the resolution of wavenumber is 0.1 cm^{-1} . The wavenumber was scanned over a range from 0 to 600 cm^{-1} . Prior to the measurement, a clean silicon wafer was examined to calibrate the initial position of slit by referring to the characteristic peak of silicon at 520 cm^{-1} .

3.2.2 Photoluminescence (PL) spectroscopy

Photoluminescence (PL) of a material under photo excitation can give information on its band structure. Crystalline semiconductor with direct bandgap usually shows strong and narrow PL peak. On the other hand, an indirect bandgap semiconductor cannot give a strong PL peak.

The Horiba spectroscopy mentioned in Raman spectroscopy was also used for observing PL spectrum of samples. The configuration used for PL measurement was similar to that used for the Raman scattering experiments. The wavelength was set to scan over a range from 600 to 700 nm.

By observing the PL signal, the indirect-to-direct bandgap transition of MoS_2



film can be observed when the thickness is reduced into one atomic layer. The PL peak will shift from 1.2 eV (1033 nm) to 1.9 eV (652 nm). However, the peak associated with an indirect bandgap is too weak to be observed.

Note that the bandgap energy of another investigated material ZnSe is about 2.7 eV. It is larger than the photon energy provided by the laser, i.e. 2.5 eV. Estimation on the band structure of ZnSe relies on the results of UV-VIS absorption experiments.

3.2.3 UV-VIS spectroscopy

Optical absorbance and transmittance of ZnSe films were measured using a Shimadzu UV-2500PC spectrophotometer. The absorption spectra may contain the information of energy band structure on exciton absorption. The incident light beam has energy spectrum covering a range from 1.5 eV to 4.0 eV. It is suitable for investigating the bandgap energy of ZnSe at 2.7 eV. According to Tauc's report⁷⁴, the band structure of a semiconductor can be estimated from the Tauc plot,

$$\alpha hv = C(hv - E_g)^n$$

where α is the absorption coefficient, E_g is the bandgap energy, and hv is the photon energy. Classification of direct or indirect transition processes can be made according to the value of power factor n , using the guidelines as summarized in Table 3-4. Experimentally, the best estimate of n can be achieved by checking the linearity of the plots of $(\alpha hv)^{1/n}$ against hv . Bandgap energy can be estimated from the intercept between the extrapolation of the linear part of the curve and the hv -axis.



n	Types of bandgap and transition
1/2	direct bandgap, allowed transition
3/2	direct bandgap, forbidden transition
2	Indirect bandgap, allowed transition
3	Indirect bandgap, forbidden transition

Table 3-5 Types of bandgap and transition with respect to different values of n.

3.2.4 X-Ray diffraction (XRD)

XRD signal can be used to identify the lattice structure and crystallinity of the samples. Some ideas on the elemental composition can be achieved according to the stoichiometry of the phases formed in the sample. The peak shift from the standard positions of respective single crystal can be used to estimate the variation of lattice constants, and hence the information on the internal strain can be derived.

Rigaku Smartlab X-Ray Diffractometer, equipped with a 9 kW rotating Cu anode of K-alpha1 X-Ray beam radiation source, was used to carry out XRD experiments. The X-ray beam from the source was filtered by passing through a crystal collimator and a 0.5° parallel slit. We used the θ -2 θ scanning mode to conduct the test. The range of 2 θ covers a range from 10° to 50°. The resolution was set at 0.01° with scanning speed of 2° per min.

3.2.5 X-Ray reflectivity (XRR)

The film thickness can be determined by observing the interference of Fresnel reflection between the sample and substrate surface using the Rigaku Smartlab X-Ray Reflectometer. It is a non-destructive method. A 2theta-omega scan at low



angle from 0° to 10° was used to determine the film thickness. The detectable range of film thickness covers from few nm to 1000 nm, but the roughness of film surface and film-substrate interface must be less than 5 nm. The thickness of MoS_2 films prepared by sputtering was determined using XRR. However, SCBD films are too rough for XRR to be used in thickness measurement.

3.2.6 Transmission electron microscopy (TEM)

Some of the MoS_2 film samples were expected to be monolayer thick. Thickness in this range is hardly determined by using XRR or surface profiler. Instead, we applied cross-section high resolution TEM to observe the film thickness directly. A TEM JEOL Model JEM-2100F was used in the experiment. The film of specimen was cut into half and was glued together using M-bond 610 glue. The specimen was grinded down to few microns by sand paper and then was ion milled to thickness which is thin enough for performing cross section (XS-) TEM imaging.

3.2.7 Atomic force microscopy (AFM)

The morphology of films was observed using a Bruker NanoScope 8 Scanning Probe Microscope (SPM). To minimize the mechanical damages generated by the tip during measurement, the system was set to operate in a non-contact mode where the cantilever was oscillating with a rate near to its resonance frequency. The van der Waals force between the tip and the detected surface can reduce the driving frequency. This effect is feedback to the system to obtain the surface profile of film. The scanning rate was confined to 0.5 Hz per line and the resolution of 256 per line. Slow scanning speed avoids wearing off of the tip especially for testing a film with rough surface like that of a SCBD film.



3.3 Gas sensing measurement

3.3.1 Measuring system

A self-assembled gas sensing system was used to measure the electrical response of samples. Detail of the system was described elsewhere⁷⁵. Figure 3-7 shows the sample holder, which is equipped with a heater and a 20 mW 365 nm UV light source positioned 2mm above the film. A sample was held with a pair of spring probes, which also worked as electrodes. The electrodes were connected to a Keithley 6517A electrometer. Figure 3-8 shows the control panel created by Labview program displayed on the screen. It shows all parameters adjusted for setting up a gas sensing test. In an experiment, the concentration and the total flow rate of the target gas in the balancing gas were set and adjusted by using mass flow controllers. The gas components in the mixture are provided from three gas sources. Two of them are gas cylinders which provide the detected gas and the balancing gas. Another one is from an Owlstone Vapor Generator (OVG-4) of volatile organic compound vapors (VOC). Besides, very low gas concentration in range of ppb for measurement can be produced in mixing chamber. Moisture can also be introduced by using another built-in water chamber in the system.

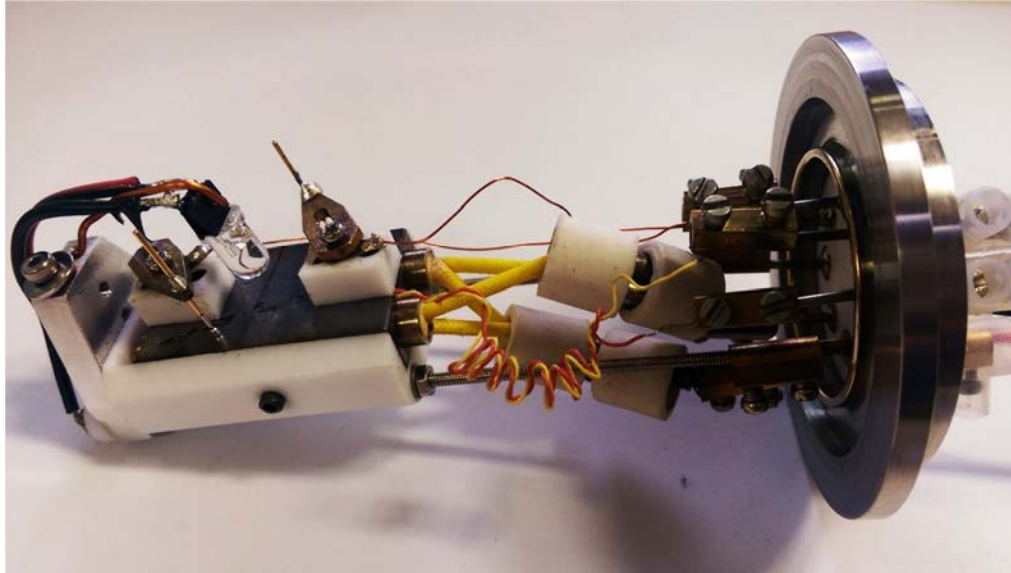


Figure 3-7 Sample holder of the gas sensing measurement system.

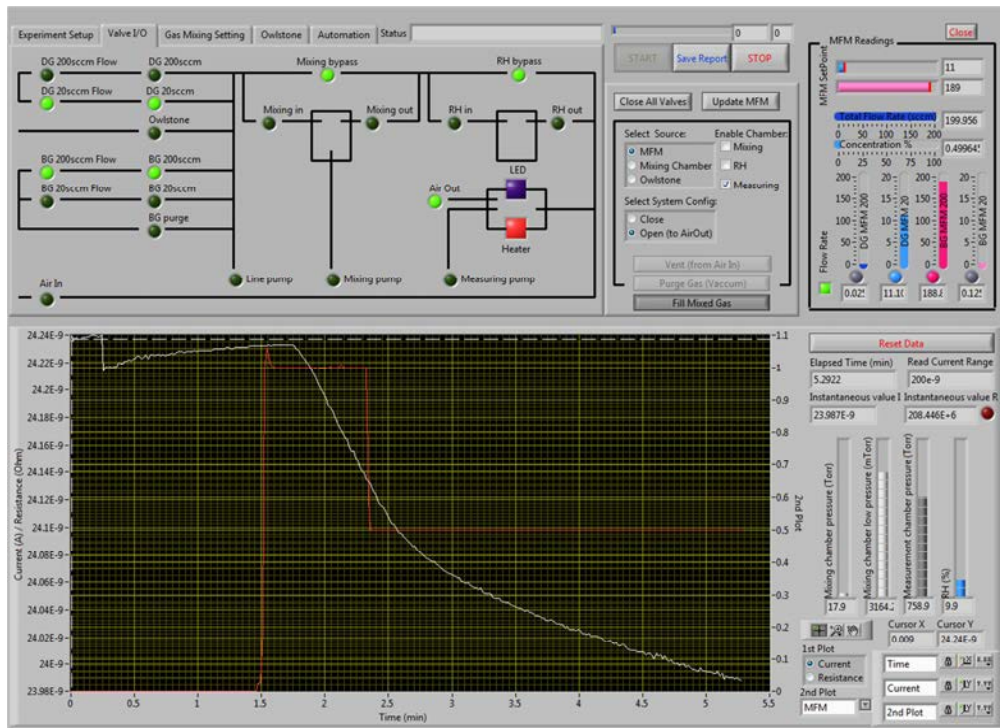


Figure 3-8 Software interface of the gas sensing measurement system.



3.3.2 Gas sensing measurement cycle

In gas sensing measurement, conductivity of film sensor is measured by applying a constant 5 V bias. Two cyclic measurement modes were adopted to fulfill the purpose of the study. They are (i) cyclic gas exchange mode and (ii) cyclic light on-off mode.

Cyclic light on-off mode

This mode was mainly used for investigating the sensing mechanism of photo-assisted oxygen detection in nanocluster-assembled ZnSe film. In this mode, light of photon energy above the direct bandgap of ZnSe was used. With the sample placed in a steady flow on the detected gas, the light source was on and off in a cyclic manner.

Figure 3-9 shows the workflow of a light on-off cycle started from evacuating the measuring chamber to remove most of the surface adsorbed gas molecules. The chamber was then filled up with a flow of mixture containing oxygen and Ar. The total flow rate is 200 sccm. The UV light source was switched on when the pressure reaching one atmospheric pressure. The dynamic (time-dependent) change of the photocurrent was monitored for 60 min. The UV light source was then switched off. The system was reset to the beginning state to prepare for the next cycle of measurement. The concentration of oxygen was varied in the new cycle of the test.

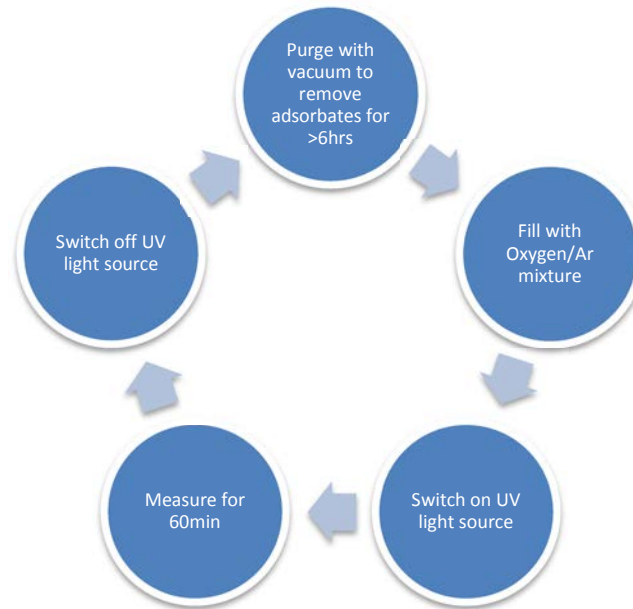


Figure 3-9 A typical measurement cycle for examining the oxygen sensing mechanism of nanocluster-assembled ZnSe film.

Cyclic gas exchange mode

In our study, this mode was used for investigating the gas sensing properties of MoS₂ films to reducing gases, including H₂S, H₂ and NH₃ under real situation of application. According to the mechanism for detecting reducing gas with semiconductor gas sensor (Section 2.3 in Chapter 2), pre-adsorption of oxygen radicals on the sensor's surface is prior to the reaction with the detected reducing gas. Therefore, in our test, we kept the sensor sample to be in a constant flow of synthetic air. The detected gas sample was admitted into the chamber periodically to generate the sensor response.

The workflow of a measurement process in this mode was presented in Figure 3-10. At the very beginning, the measurement chamber was evacuated and waited for the dark current to stabilize. This step ensured that most of the unknown



adsorbates on the film surface have been removed. Then, a continuous flow of 200 sccm synthetic air was admitted into the chamber. The sample was heated up to 80 °C to reduce the moisture on the surface. An above-bandgap UV light beam was turned on and shine on the film surface directly. Until the current of the film became stable, the sample gas mixture of target gas balanced by synthetic air was admitted into the chamber. The change of the current was recorded for 15 min. The condition was then reset by admitting synthetic air into the chamber. Repeated cycles with varies gases and concentrations were conducted.

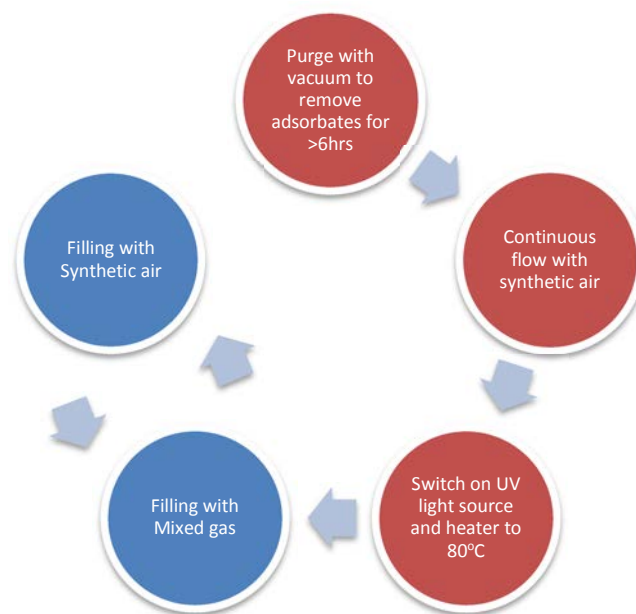


Figure 3-10 A typical measurement cycle for examining the gas sensor response of MoS₂ films against reducing gases.



Chapter 4 **Dynamic gas sensing mechanism of nanocluster-assembled ZnSe film under UV illumination**

The scope of this part of study is for analyzing the sensing mechanism of electrical response of photo-assisted semiconductor gas sensor. A new theoretical model is proposed to interpret the physiochemical mechanism on oxygen detection in nanocluster-assembled ZnSe film gas sensor under UV illumination.

4.1 Gas sensing mechanism

The sensing mechanism should be a joint effect of many complicated physiochemical processes. According to section 2.3 in Chapter 2, it can be considered with three parts: receptor function, transducer function and operation mode.

Receptor function

Receptor function describes the charge exchange between adsorption of gas molecules and the semiconductor sensor material⁷⁶. Adsorption isotherms of gases are modeled with several well-known models³⁶. For low detected gas concentration, the mechanism associated with the Langmuir adsorption isotherm dominates. It is applicable in the case of having one layer of chemisorbed gas molecules. For case of higher detected gas concentration, multilayer adsorption occurs. The first layer reach full coverage and further physisorption of gas will be presented on higher level of layer. It is modeled by the BET adsorption isotherm developed by Brunauer, Emmet and Teller⁴². For even higher gas concentration, the



theory was further revised to include the capillary effect for describing condensation of a gas in mesoporous film. This is mostly applied to discuss the gas-liquid transition phenomenon⁷⁷.

Transducer function

Transducer function is essentially affected by the microstructure of sensor elements, which can be demonstrated by grain size effect. Depletion region is established at the sensor's surface and potential barrier is generated at the intergranular region due to gas adsorption on the surface. The electrical conductivity of the sensor element is altered to give further sensor response depending on the gas concentration¹³.

Operation mode

The operation mode affects the performance of sensor referring to the setting of operation conditions, including operation temperature, catalyst incorporation and photo-assist. Many theoretical and empirical models have been developed for explaining the dependences of the dynamic changes of sensor response on these operation conditions^{11,30-33}.

For the consideration on operation temperature, it can alter the adsorption-desorption condition of the gas molecules^{24,25}. A rise in temperature increases the reaction rate between adsorbed oxidizing gas and detected gas. It also prevents the condensation of moisture on the sensor's surface which is highly affecting the sensor response. We performed gas sensing tests at both the room temperature and 80 °C, in order to interpret the difference in terms of the surface adsorption-desorption mechanism.

For the consideration on applying photo-assist, it is found to be effective in gas



sensor enhancement at lower operation temperature²⁶⁻²⁸. This technique could lead to the advantages of lowering the power consumption and reduction of thermal noise and drift of the output. In this study, we use above-bandgap photo-assist to amplify the sensor response in nanocluster-assemble ZnSe.

4.2 Nanocluster-assembled ZnSe film

4.2.1 Material selection

For this part of the project, we selected highly porous nanocluster-assembled ZnSe films prepared by supersonic cluster beam deposition (SCBD) for gas sensing measurement and mechanism analysis.

A porous film material with a higher surface-to-volume ratio would have a larger amount of adsorption sites. It results stronger ability in absorbing gas molecules and gas sensing signal (refer to section 2.3). SCBD is an effective method of producing films of high porosity and surface corrugation⁷⁸. The benefits of using SCBD oxide films in gas sensing have been demonstrated in literature⁷⁹

ZnSe is an well-known optoelectronic semiconductor having a narrower direct bandgap of 2.7 eV and a short carrier lifetime compared to another popular gas sensor material ZnO⁴³. It was also reported to be sensitive to NO₂ gas under UV illumination⁵¹. It would therefore be a potential material capable of giving a fast and strong resistive response in oxygen detection.

4.2.2 Material characterization

Synthesis detail of nanocluster-assembled ZnSe film was discussed in section 3.1 in Chapter 3. Figure 4-1 shows the AFM images of an as-deposited SCBD Zn metal

film and a post-selenized ZnSe film. One sees clearly that the film is an assembly of nanoclusters and has a high porosity. The thickness is about 145 nm. The mean diameter of pristine Zn nanoclusters in the as-deposited film is about 33.6 nm and is enlarged to 52.8 nm after selenization. Moreover, the surface roughness dropped from 14.8 nm to 7.06 nm. It indicates that the nanoclusters congregate to some extent and hence the structure is smoothed as a consequence.

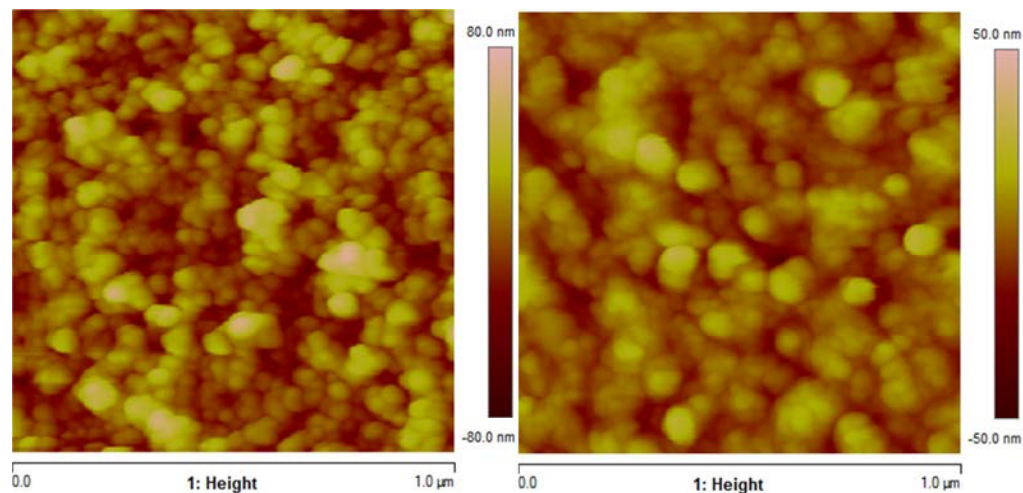


Figure 4-1 AFM images of an as-deposited nanocluster-assembled Zn metal film (left) and a post-selenized nanocluster-assembled ZnSe film (right).

Achievement of ZnSe phase was confirmed according to the results of Raman spectroscopy, XRD and UV-VIS spectroscopy analyses. All the data confirmed the presence of ZnSe and no other crystal phase can be identified after post-selenization of nanocluster-assembled Zn film.

Figure 4-2 shows three characteristic Raman peaks of the ZnSe phase at the positions of 205.66 cm^{-1} , 251.32 cm^{-1} and 500.45 cm^{-1} . They are attributed to the transverse and longitudinal vibrational modes of the Zn-Se crystal structure. Other than the broad feature from the quartz substrate as seen in the low wavenumber

region, no other recognizable structural information can be found. It is concluded that post-selenization can activate the reaction between the as-deposited pristine Zn and selenium vapors to produce film structure composed of rather pure ZnSe phase.

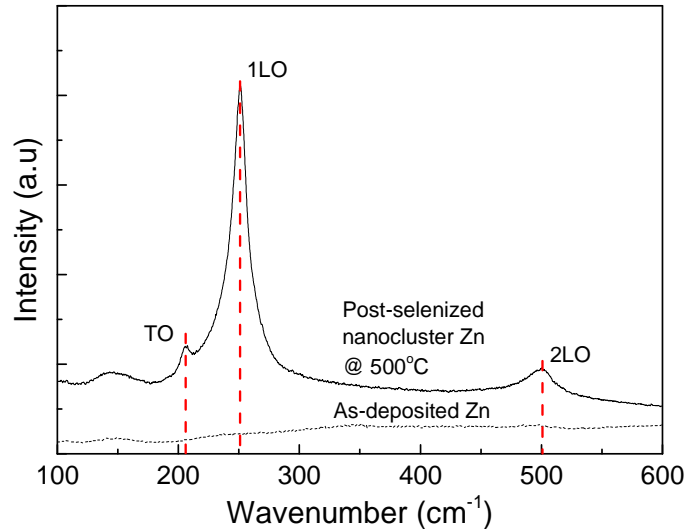


Figure 4-2 Raman spectrum of as-deposited SCBD Zn and post-selenized SCBD ZnSe film.

The crystal structure of the film was further examined using XRD. As shown in Figure 4-3, there are two diffraction peaks at $2\theta = 27.22^\circ$ and 45.18° in the spectrum of post-selenized ZnSe film. The corresponding lattice spacing are 0.33 nm and 0.20 nm, respectively, and are attributable to the (111) and (220) planes of ZnSe crystal. This provides further evidence confirming the success in crystallizing ZnSe nanoclusters in the film structure.

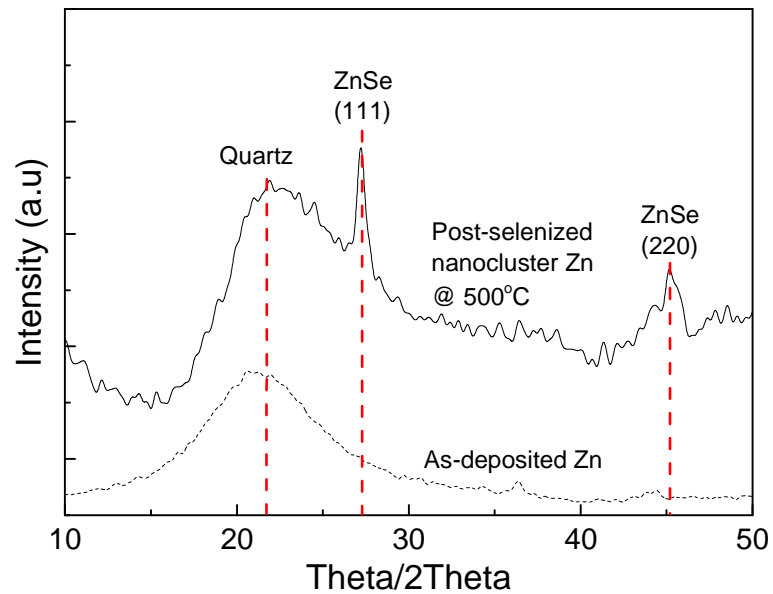


Figure 4-3 XRD spectrum of post-selenized SCBD ZnSe film.

The UV-VIS absorption spectrum of the post-selenized SCBD ZnSe film was measured. Figure 4-4 shows the result of fitting a Tauc plot to the data with $n = 1/2$. A linear trend is seen in the photon energy range > 3.0 eV is seen. The nanocluster ZnSe film is thereby believed to have a direct bandgap. The extrapolation of the linear part cut the $h\nu$ -axis at 2.8 eV, which represents the estimated bandgap energy of the material. It is slightly larger than the standard one of the bulk crystal, possibly due to the influence of quantum confinement effect of the film structure.

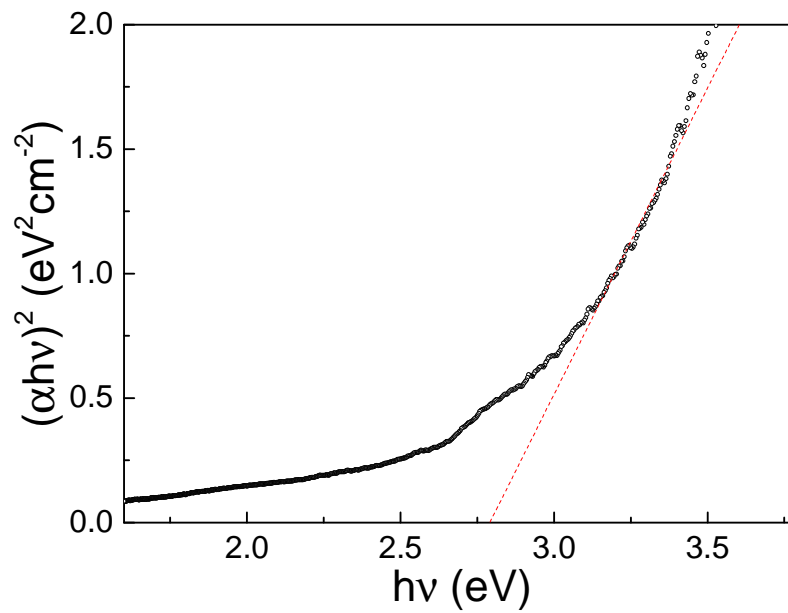


Figure 4-4 UV-VIS absorption spectrum of a post-selenized SCBD ZnSe film and the Tauc plot with $n=1/2$.



4.3 Theoretical modeling of gas sensing mechanism

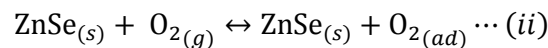
4.3.1 Dynamic of carrier and hole density

As shown in Figure 4-5, the dynamic photo-assisted gas detection process can be described with a simplified model consisting of (a) photo generation and recombination of electron-hole pairs, (b) oxygen adsorption and desorption, and (c) ionization of the adsorbed oxygen species.

Electron-hole pairs are generated when electrons absorb photons of above-bandgap energy $h\nu$ in the valence band and are excited to the conduction band. The reverse process is the recombination of electron-hole pair where electron e^- from the conduction band drops to a vacancy in the valence band and combines with a hole. These processes can be illustrated by following equation:



Next, when an oxygen molecule is adsorbed, it can form an acceptor-like trap state with energy E_a below the conduction band edge. On the contrary, the adsorbed oxygen can detach from the surface after absorbing energy amount of energy (photo or thermal). These two reactions can be described by the equation:



Then, conduction electrons from the conduction band could fall into the trap states to form negatively charged oxygen ions. On the other hand, electrons from the valence band could be excited to reach the trapped states to form adsorbed negative oxygen ions. Thus, the concentration of charge carriers varies with the adsorbed oxygen. It changes the electrical conductivity of the ZnSe film. The processes are described as:

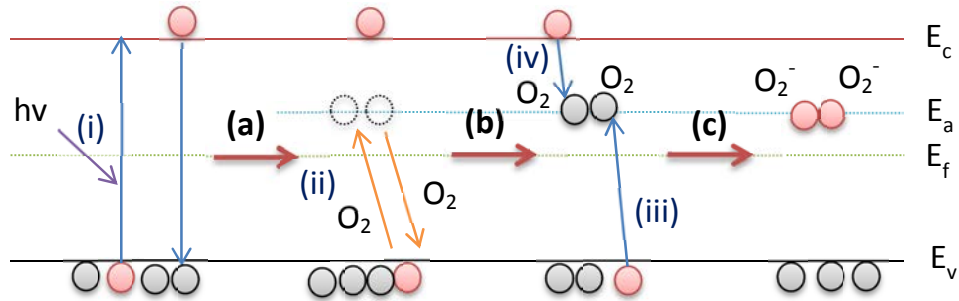
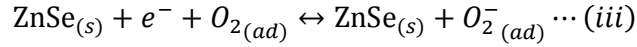


Figure 4-5 Schematic diagram of dynamic interactions involving photo generated electrons and holes, surface sorption and ionization of oxygen species under UV illumination.

4.3.2 Derivation of dynamic (time-dependent) photoconductivity

In this section, we derive the equations for describing the dynamic (time-dependent) change of photoconductivity of photo-assisted ZnSe when reacting with oxygen.

Adsorption-desorption mechanism

The dynamic (time-dependent) change of the surface coverage of adsorption sites $\theta(t)$ can be presented in terms of the ratio of the concentration of the adsorbed oxygen $N_t(t)$ to the concentration of the total absorption sites N_0 , namely $\frac{N_t(t)}{N_0}$. The time dependence of $\theta(t)$ is controlled by the adsorption rate constant $k_a(c)$ which depends on oxygen concentration c , and desorption rate constant k_d , such that:



$$\frac{1}{N_0} \frac{\partial N_t(t)}{\partial t} = \frac{\partial \theta(t)}{\partial t} = k_a(c)(1 - \theta) - k_d\theta \quad \text{Eq. 4.1}$$

Thus, $\theta(t)$ is solved as:

$$\theta(t) = \left(1 - \frac{k_d}{k_A(c)}\right) (1 - e^{-k_A t}) \quad \text{Eq. 4.2}$$

$$k_A(c) = k_a(c) + k_d \quad \text{Eq. 4.3}$$

where $k_A(c)$ is designated as the adsorption-desorption rate constant.

$k_A(c)$ can be further derived by applying adsorption models for different ranges of the detected gas concentration. Boundary conditions in terms of the limit of $\theta(t)$ taken at time approaching infinity are used. First, consider the condition of low concentration. Langmuir adsorption model is used for single layer of oxygen adsorption on the sensor's surface. From Eq. 2.25 and taking the limit of Eq. 4.2 at time $t \rightarrow \infty$, one obtains:

$$\theta_{t=\infty} = \frac{k_L c}{1 + k_L c} = 1 - \frac{k_d}{k_A(c)} \quad \text{Eq. 4.4}$$

Thus, the adsorption-desorption rate constant of Langmuir model $k_{A,L}(c)$ is:

$$k_{A,L}(c) = k_d(1 + k_L)c \quad \text{Eq. 4.5}$$

When the oxygen concentration increases, multilayer adsorption occurs, and the BET adsorption model should be applied. From Eq. 2.26, one obtains:

$$\theta_{t=\infty} = \frac{k_{BET}c}{(1 - c)[1 + c(k_{BET} - 1)]} = 1 - \frac{k_d}{k_A(c)} \quad \text{Eq. 4.6}$$

The corresponding adsorption-desorption rate constant $k_{A,BET}(c)$ is:

$$k_{A,BET}(c) = k_d \cdot \frac{(1 - c)[1 + c(k_{BET} - 1)]}{(1 - c)[1 + c(k_{BET} - 1)] - k_{BET}c} \quad \text{Eq. 4.7}$$



Ionization

It is assumed that only the first layer of oxygen molecules chemisorbed on the sensor's surface is ionized. Electrons from the conduction band are trapped at the trapped states associated with the adsorbed oxygen species. The ratio of the concentration of the adsorbed ionized oxygen species N_t^- to the concentration of adsorbed oxygen N_t would be equal to the ratio of the first layer surface coverage θ_0 to the total surface coverage provided by all the adsorbed gas layers $\sum_{i=0}^{\infty} \theta_i$. The expression is:

$$\frac{N_t^-}{N_t} = \frac{\theta_0}{\sum_{i=0}^{\infty} \theta_i} \quad \text{Eq. 4.8}$$

At low gas concentration, the Langmuir adsorption model is used. Only one layer of adsorbed gas molecules is involved. Eq. 4.8 can thus be simplified to obtain the explicit expression of the concentration of the adsorbed oxygen ions $N_{t,L}^-$:

$$N_{t,L}^- = N_t \quad \text{Eq. 4.9}$$

At high gas concentration, the BET adsorption model is used. The total surface coverage can be derived from Eq. 2.45. Thus, the concentration of the adsorbed oxygen ions in the BET model $N_{t,BET}^-$ is expressed explicitly as:

$$N_{t,BET}^- = \frac{1 - c}{1 - c(1 - k_{BET})} N_t \quad \text{Eq. 4.10}$$

Recombination of photo-generated carrier and hole by potential barrier

When oxygen molecules are adsorbed to form trap states on the sensor's surface, photo generated electrons in the conduction band can drop to the trap states. The process is further limited by the potential barrier E_B at the intergranular region. It affects the transport and population of the charge carriers and thus an



electrical response is generated as a consequence. Assumed that the dynamic (time-dependent) variation of the photo-generated electrons $\Delta n(t)$, is determined by recombination through the trap states. The contribution from direct band-to-band recombination is assumed to be constant and independent to electrons at conduction band. The generation rate constant of direct band-to-band transition and recombination rate constant of trap state are k_g and k_r respectively. The changing rate of $\Delta n(t)$ is modeled as:

$$\frac{\partial \Delta n(t)}{\partial t} = k_g - k_r(E_B) \Delta n \quad \text{Eq. 4.11}$$

The recombination rate constant k_r is a function of the potential energy of barrier E_B . Since the charge carriers require enough energy to across the potential barrier, it is assumed that the rate would follow Maxwell-Boltzmann probability distribution. Thus the recombination rate is estimated by the Maxwell-Boltzmann statistic:

$$k_r(E_B) = k'_r \left(1 - e^{-\frac{E_B}{kT}} \right) + k_{r0} \quad \text{Eq. 4.12}$$

where k'_r and k_{r0} refer to the recombination rate constants of electrons under the influence of the potential barrier and natural recombination associated with the transition of electrons from conduction band to trap states respectively.

The potential barrier energy E_B can be derived from Poisson's equation, which depends on the concentration of adsorption gas N_t , the effective adsorption energy E_{eff} of the adsorbed gas molecules and the grain diameter D :

$$E_B(D, c, t) = \frac{q^2 D^2}{8\epsilon\epsilon_0} E_{\text{eff}} N_t(c, t) \quad \text{Eq. 4.13}$$

At low oxygen concentration, the Langmuir adsorption model is applied. In this



case, only chemisorbed oxygen ions are involved. The effective adsorption energy of these ions is assumed to be equal to the chemisorption energy E_{chem} :

$$E_{eff,L} = \frac{E_{chem}\theta_0}{\theta_0} = E_{chem} \quad \text{Eq. 4.14}$$

At high oxygen concentration, multilayers of oxygen can be physisorbed on top of the first layer, and hence the BET adsorption model is applied. The effective adsorption energy is assigned by the chemisorption energy from the first layer of $i = 0$ and the physisorption energy E_{phy} from other layers of $i > 0$:

$$E_{eff,BET} = \frac{E_{chem}\theta_0 + E_{phy}\sum_{i=1}^{\infty}\theta_i}{\sum_{i=0}^{\infty}\theta_i} \quad \text{Eq. 4.15}$$

According to Eq. 2.26, the effective adsorption energy under BET can be expressed as:

$$E_{eff,BET} = \frac{E_{chem} - c(E_{chem} - E_{phy}k_{BET})}{1 - c(1 - k_{BET})} \quad \text{Eq. 4.16}$$

Therefore, from Eq. 4.12 and Eq. 4.13, the recombination rate constant becomes a time dependent function:

$$k_r(D, c, t) \propto e^{-\frac{q^2 D^2 N_0 E_{eff}}{8\epsilon\epsilon_0 kT} \left(1 - \frac{k_d}{k_A(c)}\right) (1 - e^{-k_A(c)t})} \quad \text{Eq. 4.17}$$

Since the measurement time t is long (in seconds) compared to the adsorption time constant $1/k_A$ (in milliseconds), such that,

$$(1 - e^{-k_A t}) \sim 1 \quad \text{Eq. 4.18}$$

k_r becomes,

$$k_r(D, c) \propto e^{-\frac{q^2 D^2 N_0 E_{eff}}{8\epsilon\epsilon_0 kT} \left(1 - \frac{k_d}{k_A}\right) (1 - e^{-k_A t})} \approx e^{-\frac{q^2 D^2 N_0 E_{eff}}{8\epsilon\epsilon_0 kT} \left(1 - \frac{k_d}{k_A}\right)} \quad \text{Eq. 4.19}$$

Hence, the recombination rate constant is considered to be time independent shortly after the start of a measurement. As a consequence, Eq. 4.11 can be solved to obtain a solution of photo-generated electron concentration as:



$$\Delta n = \frac{k_g}{k_r} (1 - e^{-k_r t}) \quad \text{Eq. 4.20}$$

On the other hand, the potential barrier energy of valance band is assumed to be similar to that of the conduction band. The recombination rate of holes through the trap states behaves similar to that of k_r of electrons derived above. The concentration of photo generated holes $\Delta p(t) \cong \Delta n(t)$, which also obeys the form of Eq. 4.20.

Dynamic photoconductivity

The photoconductivity of a semiconductor is:

$$\sigma = q(n\mu_e + p\mu_h) \quad \text{Eq. 4.21}$$

The total free electron concentration is equal to the sum of the concentrations of intrinsic electrons and photo-generated electrons minus the concentration of the absorbed oxygen ions:

$$n = n_0 + \Delta n - N_t^- \quad \text{Eq. 4.22}$$

The free holes concentration is equal to the sum of intrinsic holes and photo-generated holes:

$$p = p_0 + \Delta p \quad \text{Eq. 4.23}$$

Thus, the electrical conductivity is:

$$\sigma = \sigma_0 + q(\mu_e + \mu_h)\Delta n - q\mu_e N_t^- \quad \text{Eq. 4.24}$$

By putting Eq. 4.8 and Eq. 4.20 into Eq. 4.24, one obtains an expression of σ which is in the form of the sum of two exponential functions:

$$\sigma = A_0 + A_1 e^{-k_r t} + A_2 e^{-k_A t} \quad \text{Eq. 4.25}$$

The explicit form of Eq. 4.25 can be obtained by substituting the following expressions into it according to the concentration range of the oxygen.



When oxygen concentration is low,

$$k_r = k'_r \cdot \left(1 - e^{-\frac{q^2 D^2 N_0 E_{chem}}{8 \epsilon \epsilon_0 k T} \left(1 - \frac{k_d}{k_A} \right)} \right) + k_{r0} \quad \text{Eq. 4.26}$$

$$k_A = k_d k_L c \quad \text{Eq. 4.27}$$

$$A_0 = \sigma_0 - A_1 - A_2 \quad \text{Eq. 4.28}$$

$$A_1 = -q \cdot (\mu_e + \mu_h) \cdot \frac{k_g}{k_r} \quad \text{Eq. 4.29}$$

$$A_2 = q \cdot \mu_e \cdot N_0 \cdot \left(1 - \frac{k_d}{k_A} \right) \quad \text{Eq. 4.30}$$

When oxygen concentration is high,

$$k_r = k'_r \cdot \left(1 - e^{-\frac{q^2 D^2 N_0 E_{chem} - c(E_{chem} - E_{phy} k_{BET})}{8 \epsilon \epsilon_0 k T} \left(1 - \frac{k_d}{k_A} \right)} \right) + k_{r0} \quad \text{Eq. 4.31}$$

$$k_A = k_d \cdot \frac{(1 - c)[1 + c(k_{BET} - 1)]}{(1 - c)[1 + c(k_{BET} - 1)] - k_{BET} c} \quad \text{Eq. 4.32}$$

$$A_0 = \sigma_0 - A_1 - A_2 \quad \text{Eq. 4.33}$$

$$A_1 = -q \cdot (\mu_e + \mu_h) \cdot \frac{k_g}{k_r} \quad \text{Eq. 4.34}$$

$$A_2 = q \cdot \mu_e \cdot N_0 \cdot \frac{1 - c}{1 - c(1 - k_{BET})} \cdot \left(1 - \frac{k_d}{k_A} \right) \quad \text{Eq. 4.35}$$

The corresponding rate constants and coefficients are direct related to the gas sensing and adsorption-desorption mechanisms as shown in Figure 4-6. In this study, the validity of this model is examined by the experimental results of oxygen detection using ZnSe under UV illumination.

This model has the following limitations:

- (i) Photoexcitation is applied to enhance the occurrence of grain size effect,
- (ii) It is only applicable to the case where only one type of gas is detected.

This model has the following assumptions as well:



- (i) Adsorption-desorption mechanism is independent of the charge carrier concentration,
- (ii) Only the first adsorbed gas layer is chemisorbed,
- (iii) The potential barrier at intergranular region resists the transport and assist electron to recombine with holes,
- (iv) The effective recombination rate of charge carriers is dominated by that of photo-generated carriers,
- (v) Recombination rate constant becomes time independent when measuring time is longer than $1/k_A$,
- (vi) Effect of balancing gas (argon) can be ignored.

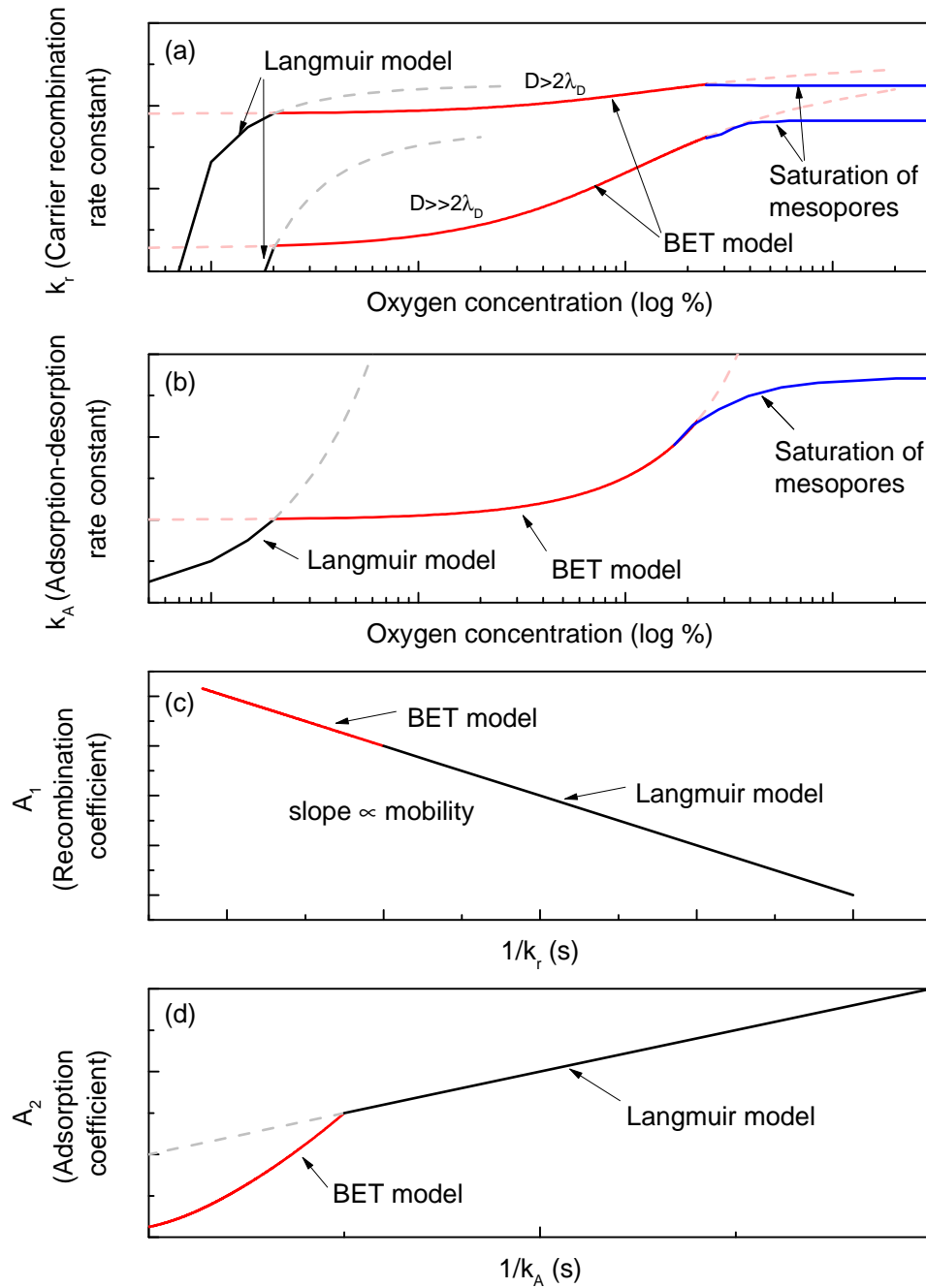


Figure 4-6 (a, b) Recombination and adsorption rate constants k_r and k_A against oxygen concentration, (c, d) recombination and adsorption coefficients A_0 ad A_1 against $1/k_r$ and $1/k_A$, respectively.



4.4 Experimental results and theoretical analysis

4.4.1 Dynamic (time-dependent) photoconductivity at room temperature

The dynamic (time-dependent) photoconductivity of nanocluster-assembled SCBD ZnSe films under UV illumination against oxygen concentration varying from 0.01 % to 20 % at room temperature was measured and shown in Figure 4-7. The experimental data points are plotted with symbols in gray color while the colored fitting curves are derived from Eq. 4.25 of the model. The curves match very well with the experiment data throughout the investigated range of oxygen concentration. The profile of the curves measured at low oxygen concentrations in the range of 0.01 – 0.2 % are different from those measured at higher oxygen concentrations. In the low oxygen concentration range, a curve of measured photoconductivity rises fast monotonically at first and approaches a saturated value asymptotically. In the high oxygen concentration range, a measured curve also rises initially, but after reaching a peak value it drops with time to approach the saturated value. This indicates that there should have a transition of gas sensing mechanism from low to high gas concentration ranges. The dynamic model established in this study is capable of giving a possible physical explanation.

Figure 4-8 shows the saturated sensor response S of nanocluster-assembled SCBD ZnSe film estimated from the dynamic model. The response is the maximum of 306.2 measured at the lowest oxygen concentration of 0.01 % that employed in our tests. It decreases to 0.3 with increasing oxygen concentration to 21 % due to the increased amount of captured electrons and depletion region on the film. A linear relation of saturated sensor response is observed in the oxygen



concentration range from 0.01 % to 0.2 %. The sensitivity $\Delta S/\Delta c$ in this range is about 192 per 1 % change of oxygen concentration. Saturation of response is observed when over 0.2 % of oxygen is detected. This reveals that the dynamic range of oxygen detection by nanocluster-assembled ZnSe gas sensor is 0.01 % to 0.2 %.

The rate constants (k_r and k_A) and coefficients (A_1 and A_2) used to obtain the fitting curve to the experimental data based on Eq. 4.25 are plotted in Figure 4-9. They reproduce the characteristic features of the theoretical functions presented in Figure 4-6. Through comparing these two sets of diagrams, this function able to describe the dominant mechanisms of different stages in the oxygen sensing process.

Figure 4-9a shows that the observed recombination rate constant k_r raises at low oxygen concentration exponentially. Compared with theoretical prediction shown in Figure 4-6a, one concludes that the grain size of the nanocluster-assembled ZnSe may be larger than the depletion region, where $D \gg 2\lambda_D$. The enhanced sensor response due to neck control of grain size effect happens at high oxygen concentration of 0.1 % when BET adsorption is occurred. The recombination rate constants increased noticeably at that condition. It keeps increasing in this regime consistent with the theoretical prediction, until the detected oxygen concentration reaches about 1 %, where physisorption of oxygen commences saturation at the mesoporous surface.

According to theoretical prediction, the recombination coefficient A_1 should drop linearly with $1/k_r$ with slope $-8.9 \times 10^{-7} \text{ M}\Omega^{-1} \text{ cm}^{-1} \text{ s}$ as shown in Figure 4-6c. In fact, experimental result illustrates this prediction as shown in Figure 4-9c. This



further suggests that the photo generation rate and charge carrier mobility are constants throughout the investigated oxygen concentration range.

The adsorption-desorption rate constant k_A controls this process, which is plotted against with the oxygen concentration in Figure 4-9b. The overall profile of the experimental curve of k_A throughout the detected oxygen region matches very well with the one predicted from the model as shown in Figure 4-6b. It increases first until the oxygen concentration reaches 0.04 %. In this low gas concentration region, oxygen molecules are mainly chemisorbed on the film surface based on the Langmuir adsorption mechanism. k_A then ceases to increase, since at this moment the sensor's surface has been mostly covered with the first chemisorbed gas layer. Until the oxygen concentration is further increased starting from 0.5 % to 2 %, k_A starts to increase with oxygen concentration again. This is because further physisorption of oxygen molecules at second or higher layers of sensor's surface starts to take place. At last, k_A saturates again. One suggests that this happens when the surface adsorption site is saturated and the mesopores are even filled up by oxygen adsorbents.

Coefficient of adsorption term A_2 obtained is plotted against $1/k_A$ in Figure 4-9d. This coefficient is closely related to the efficiency of ionization of the adsorbed oxygen. The slope of the curve at high $1/k_A$ region (low oxygen concentration) is constant $2.4 \times 10^{-7} \text{ M}\Omega^{-1} \text{ cm}^{-1} \text{ s}$. However, declines sharply when $1/k_A$ drops to a critical value (high oxygen concentration). This is because excessive oxygen adsorption causes physisorption dominates and enters the BET adsorption regime. The adsorption energy associated with physisorbed oxygen is relatively lower than chemisorbed oxygen. Hence the efficiency of ionizing the adsorbed



species is also lower. These features represent a transition from chemisorption mechanism to physisorption mechanism as indicated in Figure 4-6d.

The sum of two exponential functions *Eq. 4.25* is thereby illustrated to be effective in describing the time dependence of photo-assisted gas sensor response of a direct-bandgap semiconductor film. The relationships between the gas sensor response and adsorption-desorption mechanisms can be achieved by deconvoluting the observed gas sensor response. Note that the method is not restricted to be used for any other grain sizes and gas concentration.

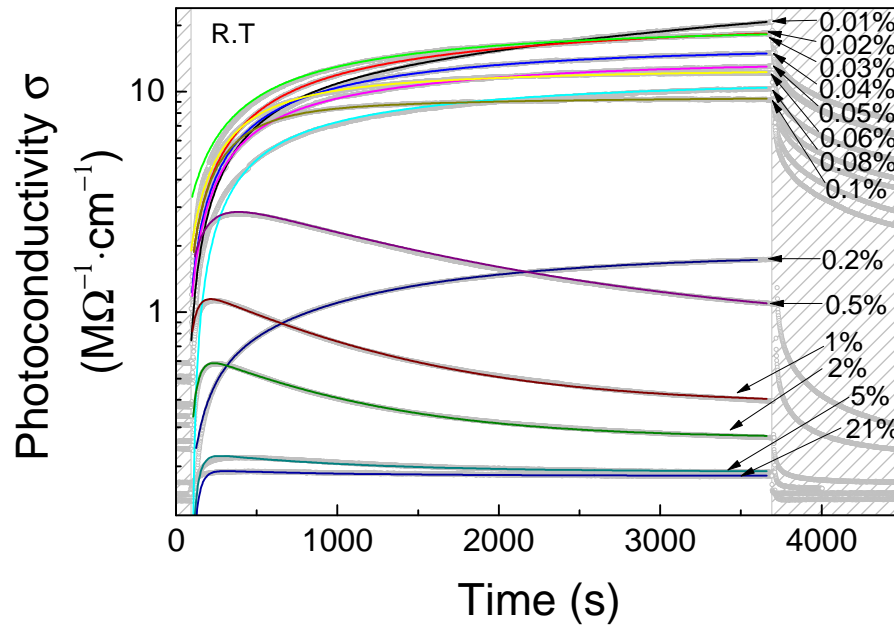


Figure 4-7 Room-temperature photoconductivity of nanocluster-assembled SCBD ZnSe films measured at various oxygen concentrations.

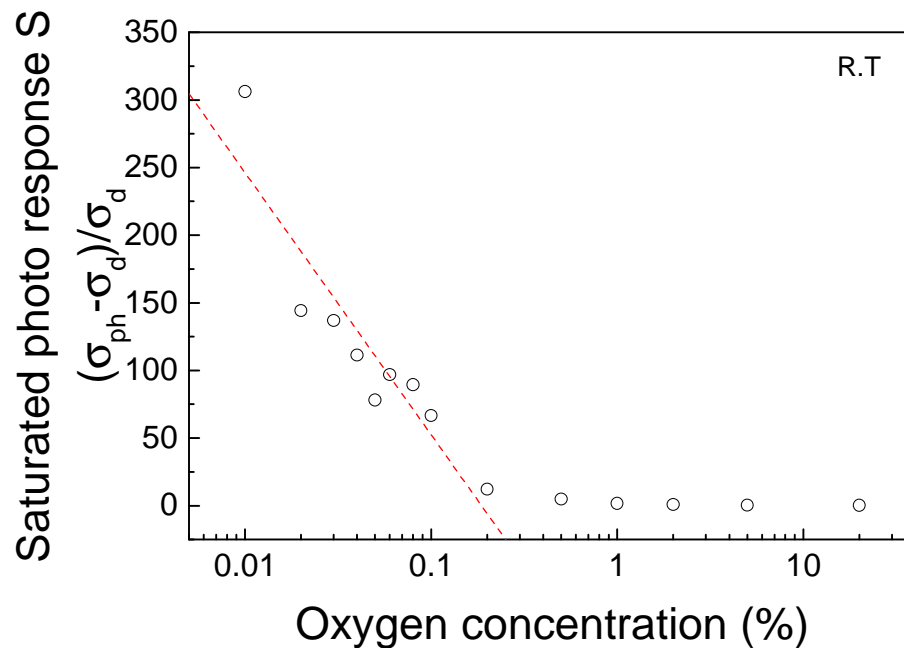


Figure 4-8 Estimated saturated photo response of nanocluster-assembled SCBD ZnSe films against various oxygen concentrations measured at room temperature.

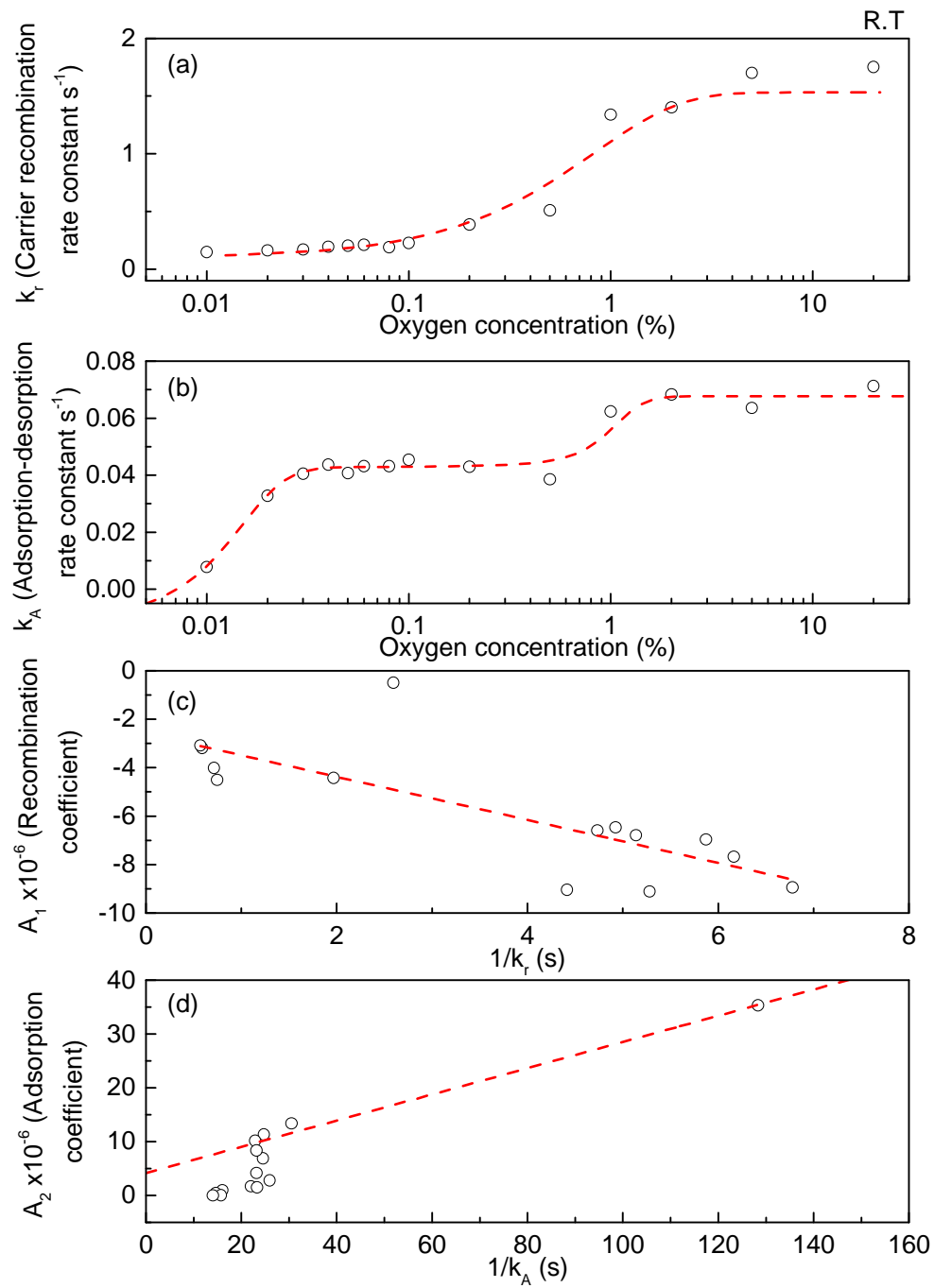


Figure 4-9 (a) Charge carrier recombination rate constant k_r (b) adsorption-desorption rate constant k_A against oxygen concentration, (c) coefficient A_1 against $1/k_r$ and (d) coefficient A_2 against $1/k_A$ measured at room temperature.



4.4.2 Dynamic (time-dependent) photoconductivity at 80 °C

Dynamic (time-dependent) photoconductivity of nanocluster-assembled SCBD ZnSe films against oxygen concentration was also measured at 80 °C in order to determine the influence of thermal energy on the gas sensing mechanism. This temperature was applied in order to prevent moisture condensation and chemical reaction of sensor's material⁵⁰. Figure 4-10 shows the sensor response for oxygen concentration varying in the range from 0.02 % to 10 %. We applied the expression of Eq. 4.25 again to fit the data. Comparison of the results measured at room temperature and 80°C is presented in Table 4-1.

The variation of saturated photo response against oxygen concentration was shown in Figure 4-11. It drops with increasing oxygen concentration first and is saturated when the oxygen concentration exceed about 0.2 %. The slope of the linear part of the profile gives the sensitivity of the sensor, $\Delta S/\Delta c$, which is about 161 per 1 % increment of oxygen concentration. It is slightly lower than that at room temperature. This can be explained by the change of rate constants k_r and k_A , and the coefficients A_1 and A_2 shown in Figure 4-12. The plots exhibit some similarity to those measured at room temperature, but some differences can still be found.

The recombination rate constant k_r , measured at 80 °C is ~8 times higher than that measured at room temperature throughout the range of oxygen concentrations employed in the measurements. This is because scattering of conduction charge carriers by phonons is more severe under higher temperature environment. The neck control mechanism commence at a higher oxygen concentration at 2 %, as the adsorption-desorption rate constant k_A of oxygen



becomes higher that associated with a higher desorption rate.

The coefficient A_1 still exhibits a linear relationship with $1/k_A$. The slope is slightly larger (from -8.9×10^{-7} to $-2.2 \times 10^{-6} \text{ M}\Omega^{-1}\text{cm}^{-1}\text{s}$) than that of the room-temperature one because the average charge carrier mobility increases with temperature.

On the other hand, results of adsorption-desorption rate constant k_A also indicate that the influence of heat to the adsorption mechanisms. Compared with the result obtained at room temperature, the magnitude of the rate is ~ 2 times larger due to the increase of desorption rate and thermal energy gain. Consequently, the saturation of first layer adsorption and mesopores adsorption occur at higher oxygen concentration at 0.2 % and 2 % respectively.

The variation of the coefficient A_2 also shows the adsorption transition from chemisorption to physisorption at higher oxygen concentration. The slope becomes larger (from 2.4×10^{-7} to $3.9 \times 10^{-7} \text{ M}\Omega^{-1}\text{cm}^{-1}\text{s}$) because thermal energy for activation energy of ionization is more readily gained at higher operation temperature.

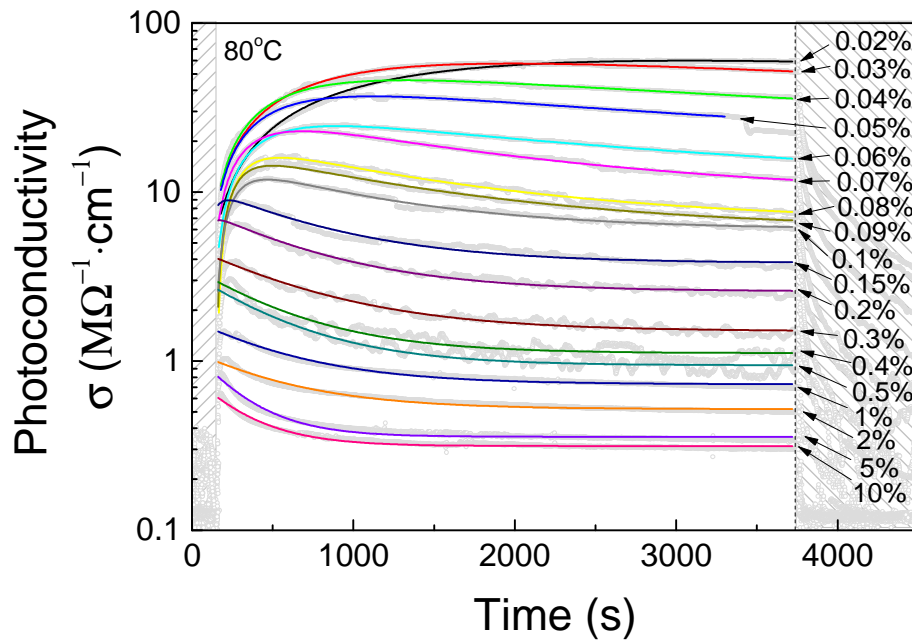


Figure 4-10 Photoconductivity of nanocluster-assembled SCBD ZnSe films against various oxygen concentrations measured at 80 °C.

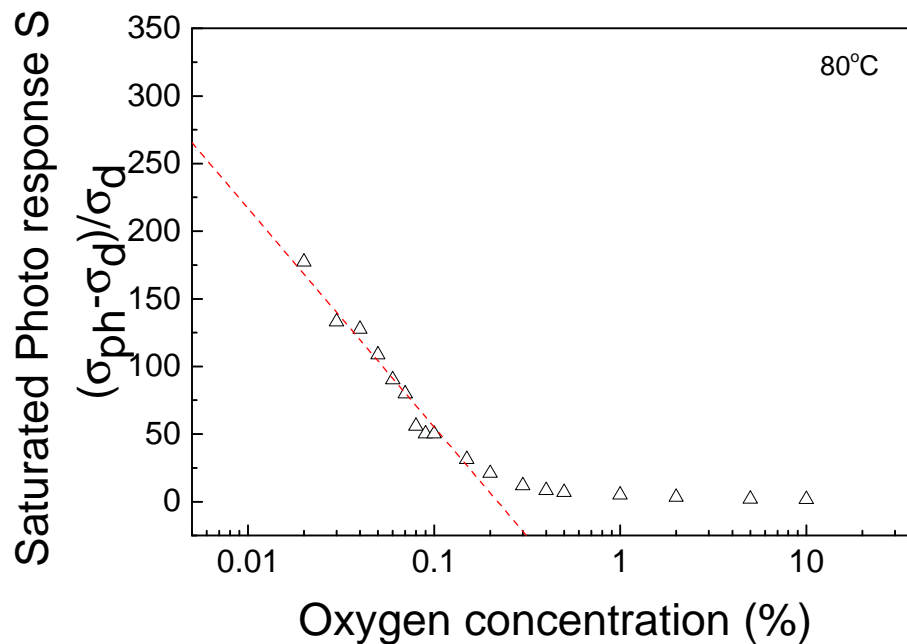


Figure 4-11 Estimated saturated photo response of nanocluster-assembled SCBD ZnSe films against various oxygen concentrations measured at 80 °C.

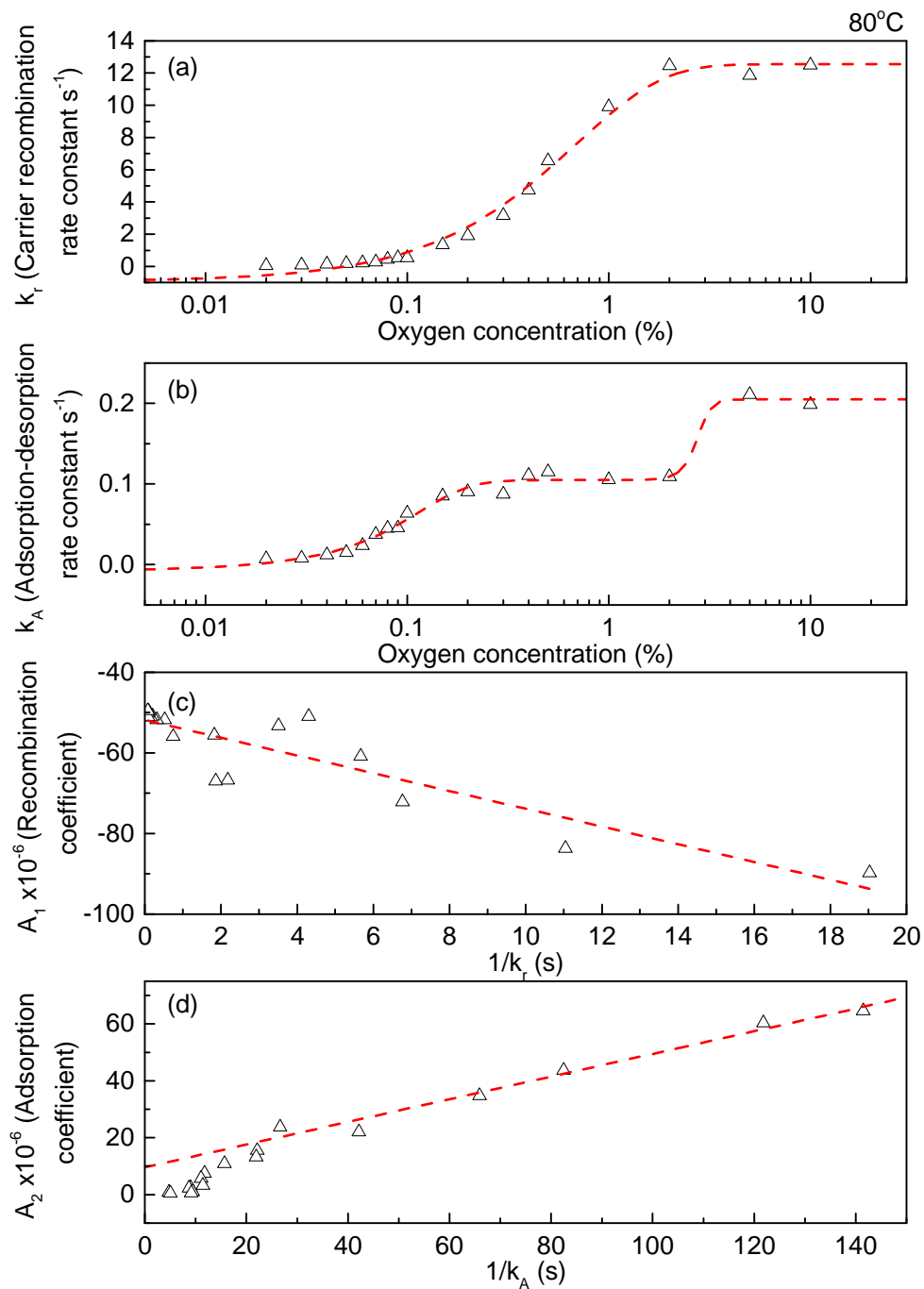


Figure 4-12 (a) Charge carrier recombination rate constant k_r (b) adsorption-desorption rate constant k_A against oxygen concentration, (c) coefficient A_1 against $1/k_r$ and (d) coefficient A_2 against $1/k_A$ measured at 80 °C.



Conditions	S Saturated photo response	$\Delta S/\Delta c$ Sensitivity at linear region	Neck control range	First layer saturation range	A ₁ Slope (mobility factor) $M\Omega^{-1}cm^{-1}s$	A ₂ Slope (ionization factor) $M\Omega^{-1}cm^{-1}s$
R.T.	306.2 - 0.3 [0.01 - 20 %]	192	0.1 - 1 %	0.04 - 0.5 %	-8.9×10^{-7}	2.4×10^{-7}
80°C	177.4 - 1.7 [0.02 - 10 %]	161	0.1 - 2 %	0.2 - 2 %	-2.2×10^{-6}	3.9×10^{-7}

Table 4-1 Lists of parameters used for describing the mechanisms of photo-assisted oxygen sensing properties of nanocluster-assembled ZnSe films at room temperature and 80 °C.

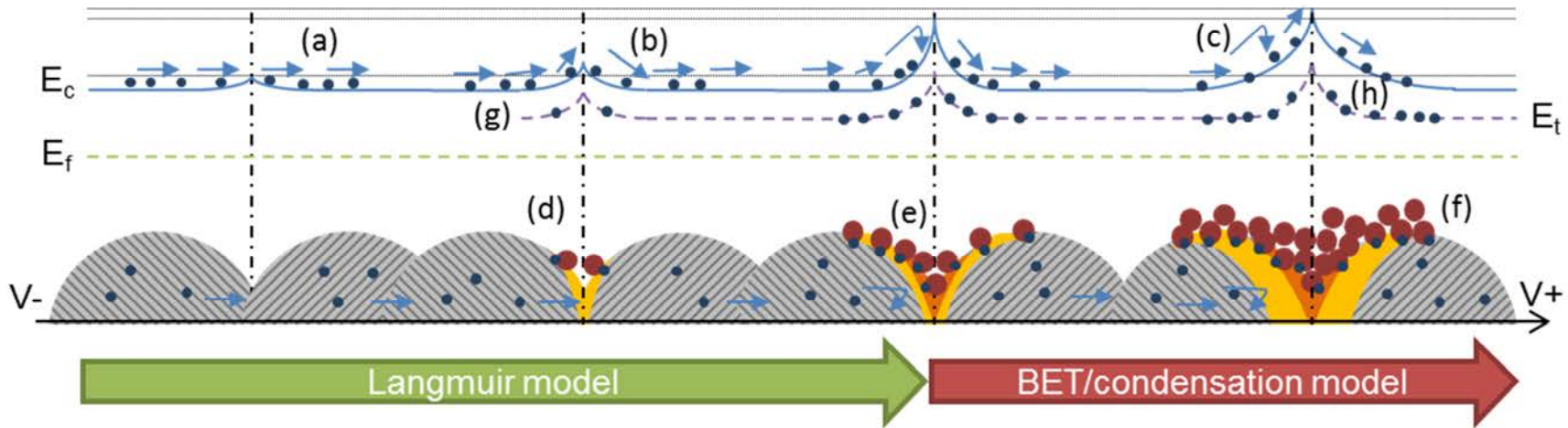


Figure 4-13 Schematic diagram of gas sensing and adsorption-desorption mechanisms controlling the gas detection process. (a-c) grain size effect (d-f) transition of adsorption models (g-h) Ionization.



The dynamic change of photoconductivity of nanocluster-assembled ZnSe against oxygen concentration can be modeled and described by using an expression containing the sum of two exponential functions *Eq. 4.25*. Results illustrated the details about the effect of adsorption-desorption mechanism to the gas sensing process under the illumination of above-bandgap light. Figure 4-13 summarized the three suggested mechanisms involved in the model in schematic view: (i) grain size effect, (ii) transition of adsorption models and (ii) Ionization. Recombination of photo-generated electrons and holes are considered to be affected by grain size effect. The increase of potential barrier energy at the intergranular region results in necking effect, which increases the probability of recombination. It depends on the surface energy absorbed by chemisorption and physisorption of oxygen. Besides, the adsorption models, Langmuir and BET adsorption models, introduced different condition of adsorption surface coverage at different gas concentrations. The dynamic evolution of adsorption process affects the grain size effect and the feasibility of ionization of adsorbed oxygen. This model provides subtle suggestions of the gas sensing mechanisms. It can be applicable to predict the time dependence of the sensor response.



Chapter 5 Gas sensing properties of nanocluster-assembled, multilayer and monolayer MoS₂ films

Transition metal dichalcogenides (TMD) is a material system which has attracted considerable attention in the past decade. Some of them exhibit changes of material properties at ultrathin layered regime. This discovery greatly stimulates recent material research and exploration of new applications. MoS₂ is one of the mostly studied materials due to its intriguing transition of optoelectronic and physical properties when the material thickness is reduce to monolayer⁵⁵. In addition, the electrical properties of monolayer MoS₂ was found to be sensitive to many gases⁶⁹⁻⁷². However, no studies have been reported about its sensing response to hydrogen sulfide (H₂S), which is hazardous to human health. In This chapter, we focus on H₂S and some reducing gases detection such as NH₃ and H₂ in MoS₂ sensor.

Chemical Vapor Deposition (CVD) is one of the most widely used techniques for fabricating monolayer crystalline flakes^{45,59-62}. Although crystalline flakes have been obtained, its lateral dimension is just within a few tens of microns. The thickness of a film sample is not uniform over a large area. This problem has been recognized and stimulates research activities for searching alternative ways to produce monolayer film material in form of large-area, continuous and uniform⁶³⁻⁶⁶. Physical Vapor Deposition (PVD) is possible choice of making large area thin film materials. It has been widely used in industries for long time and is proved to be effective in practical application. Thus, we use PVD method for fabricating monolayer MoS₂ film in our study.



We first present the details of the fabrication processes used for producing MoS₂ films of different characteristic and structural architectures. They include porous nanocluster-assembled MoS₂ film fabricated by SCBD and post-sulfurization, multilayer and monolayer MoS₂ films fabricated by reactive magnetron sputtering. We also present the data of resistive response of the materials against H₂S, NH₃ and H₂. Measurements were done in dark and under above-bandgap UV light illumination. Possible mechanisms responsible for the sensing processes are discussed.

5.1 Porous nanocluster-assembled MoS₂ film

Porous nanocluster-assembled MoS₂ film was prepared using supersonic cluster beam deposition (SCBD) process followed by post-sulfurization at elevated temperature. The film structure is expected to be highly porous. Detected gas molecules could diffuse more readily into the film.

5.1.1 Surface morphology

Figure 5-1 shows the AFM images of an as-deposited Mo film and the film after post-sulfurization. Both images show that the film surface is rough and full of holes, suggesting that the film structure is highly porous. The mean diameter of the as-deposited nanocluster-assembled Mo film is roughly 36.1 nm. It increases to 71.3 nm after sulfurization. The final thickness of the MoS₂ film is about 465 nm.

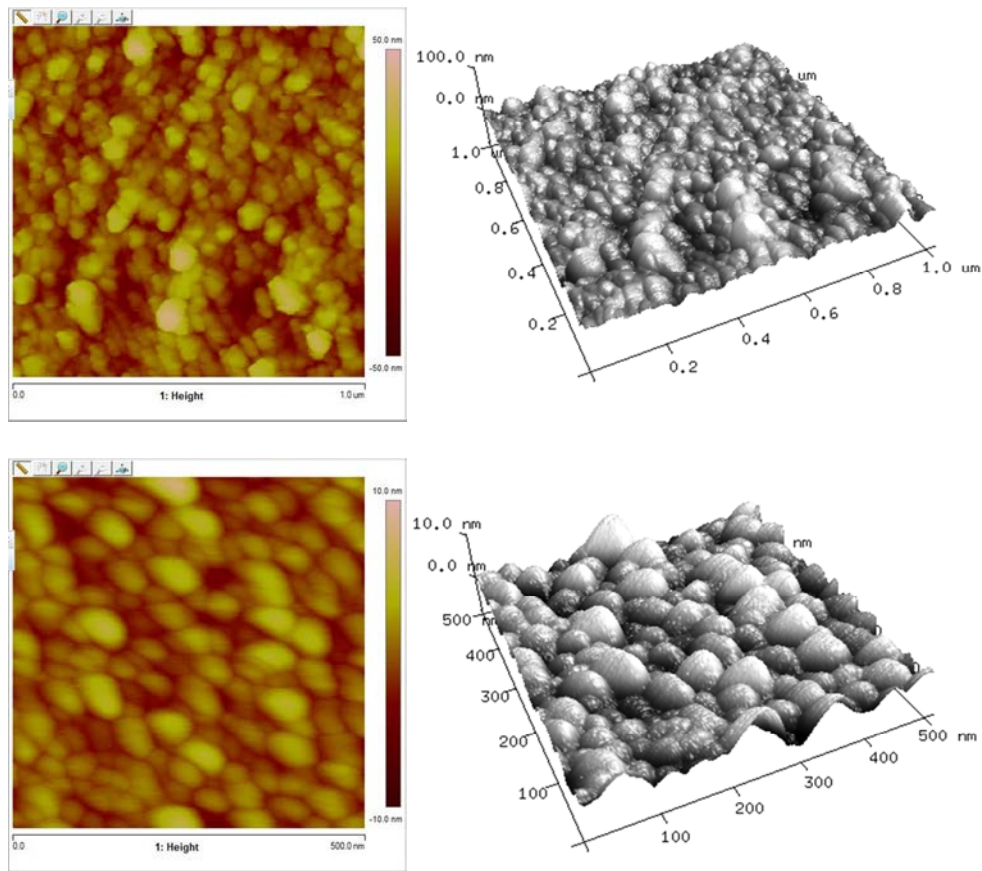


Figure 5-1 AFM image of as-deposited SCBE Mo nanoclusters film over an area of 1 μm x 1 μm (top) and 500 °C post-sulfurized nanocluster-assembled MoS₂ film over an area of 500 nm x 500 nm (bottom).

5.1.2 Confirmation of the formation of the MoS₂ compound

The post-sulfurized nanocluster-assembled SCBD Mo film was characterized using Raman spectroscopy and XRD. Figure 5-2a shows the characteristic Raman peaks of MoS₂ at 382.2 cm⁻¹ and 406.8cm⁻¹. These peaks are attributed to the phonon energy E_{2g}¹ and A_{1g} respectively. Figure 5-2b shows the XRD spectrum of the sample. A weak peak signal at 2θ = 13.96° is observed. It is ascribed to the (002) planes of the MoS₂ phase. These results confirm that the post-sulfurized film is in

form of MoS_2 phase. Suggesting that there are small crystallized MoS_2 grains is formed as well.

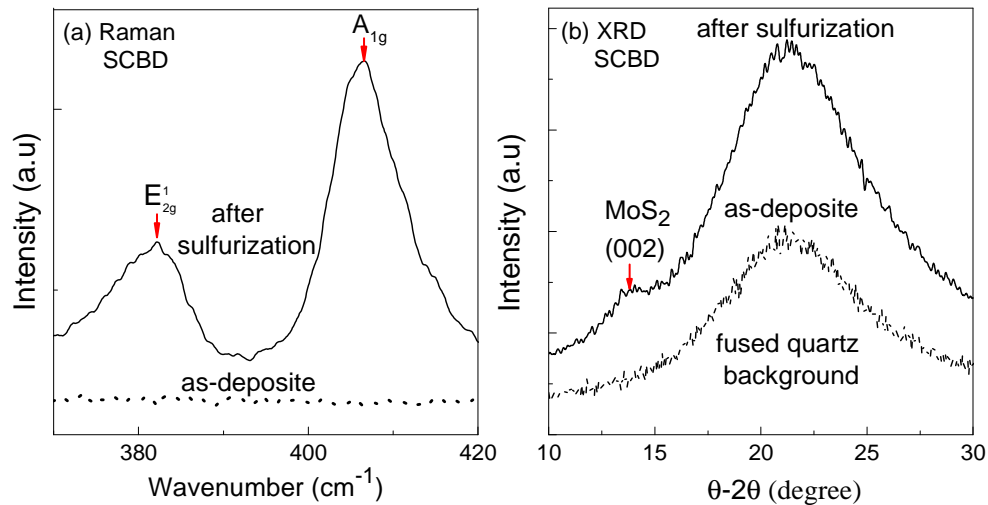


Figure 5-2 (a) Raman and (b) XRD spectra of as-deposited SCBD Mo film and the same film after post-sulfurization at 500 °C.

5.2 Multilayer and monolayer MoS_2 films

Multilayer and monolayer MoS_2 films were synthesized using one-step reactive DC magnetron sputtering process. MoS_2 films were grown on the IDE patterned SiO_2/Si substrate. After the optimum deposition condition for obtaining the best crystallization and phase composition, the deposition time was reduced to control the film thickness to monolayer film. The condition refers to the combination of the concentration of reactive H_2S ($C_{\text{H}_2\text{S}}$), substrate temperature (T_s) and sputtering pressure (P_s).

5.2.1 Effect of H_2S content in the reactant gas

In a sputtering process, plasma is ignited with a reactant gas in a reduced pressure environment to generate ions. The ions are accelerated to bombard a solid



target. The atoms removed from the target are deposited on a substrate. The composition in the deposits may deviate from that of the target material. Sulfur having low melting point could be more readily evaporated from the target, causing the deposits to have lower sulfur content than the target. For this reason, it is important to mix H_2S with the balancing argon gas to form the reactant gas for providing additional S atoms to achieve the desired stoichiometry in the deposits. We started from the settings with a sputtering power = 20 W, operating pressure P_s = 25 mTorr, substrate temperature T_s = 700 °C and a deposition time t = 30 min, whereas the concentration of H_2S in the reactant gas was varied as a parameter for achieving the desired MoS_2 film structure.

The Raman spectra of the as-deposited MoS_2 films prepared with varies of H_2S concentration from 0 % to 9 % is shown in Figure 5-3. All the films show the characteristic peaks of the MoS_2 structure. Importantly, the intensity of peaks increases with increasing H_2S concentration. When the H_2S concentration is increased to 9 %, the intensity of the Raman peak reaches the maximum. This indicates that the content of MoS_2 phase in the specimen is the largest. Since this concentration is the highest level achievable by gas source, we kept 9 % H_2S setting in all other deposition processes.

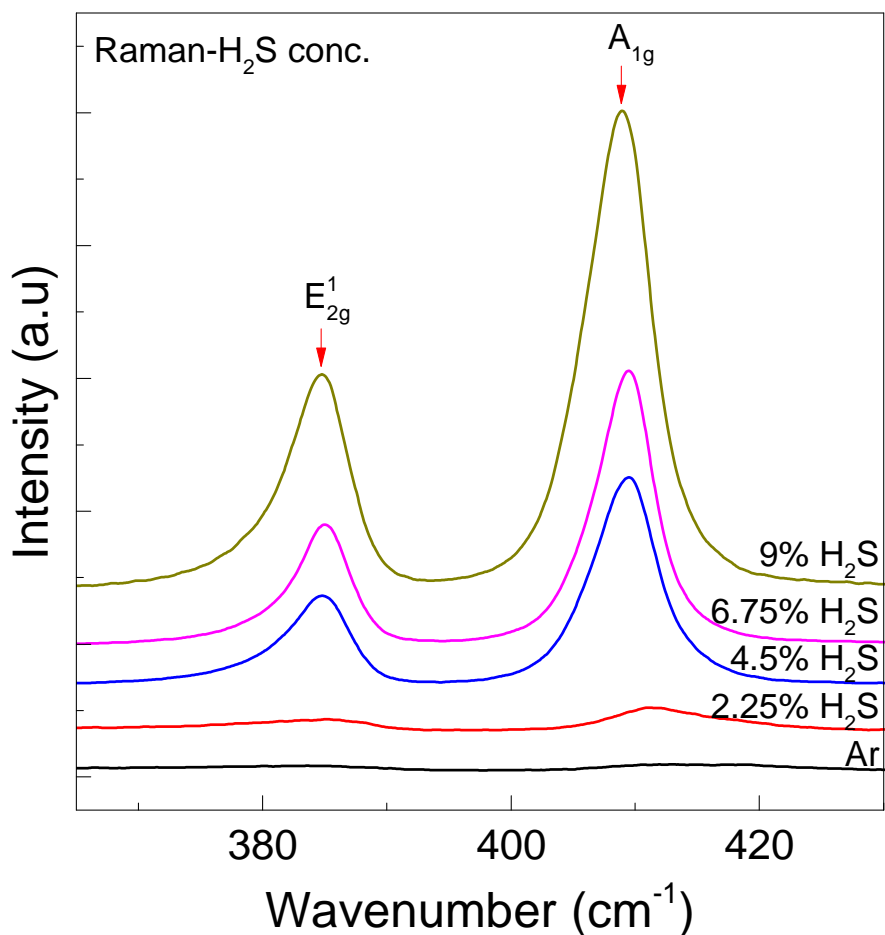


Figure 5-3 Raman spectra of MoS₂ films deposited with various H₂S concentration from 0 % to 9 % in argon.

5.2.2 Substrate temperature

Substrate temperature T_s can significantly affect the crystallization of the film material^{80,81}. On the other hand, it also affects the magnitude of the internal stresses. One possible reason for generating internal stresses is due to the mismatch of thermal expansion coefficients between the substrate material and the deposits. To investigate the influence of T_s and to optimize its setting, we carried out a series of deposition runs by fixing the sputtering power = 20 W, $P_s = 25$ mTorr,



9% H₂S in Ar and deposition time $t = 60$ min, whereas varied T_s was adjusted to vary over a range from 300 °C to 700 °C.

Figure 5-4a shows that the Raman spectra of all MoS₂ films have E_{2g}¹ and A_{1g} peaks. When T_s increases from 300 °C to 700 °C, the wavenumber of the E_{2g}¹ peak exhibits a blue shift of 3.8 cm⁻¹. At the same time, the A_{1g} also shows a blue shift of 2.0 cm⁻¹. This result indicates a change of the stress in the film.

On the other hand, the full-width-at-half-maxima (FWHM) derived from the spectrum lines are plotted in the inset of Figure 5-4a. One sees that the FWHM drops with increasing T_s first up to 500 °C, but then increases when T_s is further increased. These results suggest that the crystallization is enhanced at first that narrowing the peak width⁸². Further rise in T_s after 500 °C results in poor crystallinity due to excessive thermal stress to the film.

The observations of XRD spectra of the films shown in Figure 5-4b further support the crystallization of MoS₂. All the samples deposited at $T_s \geq 300$ °C shows characteristic peaks of the MoS₂ phase, indicating that all of them have been crystallized. Two peaks at $2\theta = 13.6^\circ$ and 44.31° are observed and are attributed to the (002) and (006) planes of MoS₂. They help to reconfirm that the MoS₂ phase dominates the in the structure of the film. In addition, only the peaks associated with the c-planes are discerned in θ - 2θ scans. One suggests that the hexagonal MoS₂ lattice planes are preferentially aligned by stacking one on the other. Based on these findings, we fixed the setting of T_s at 500 °C for all other deposition processes.

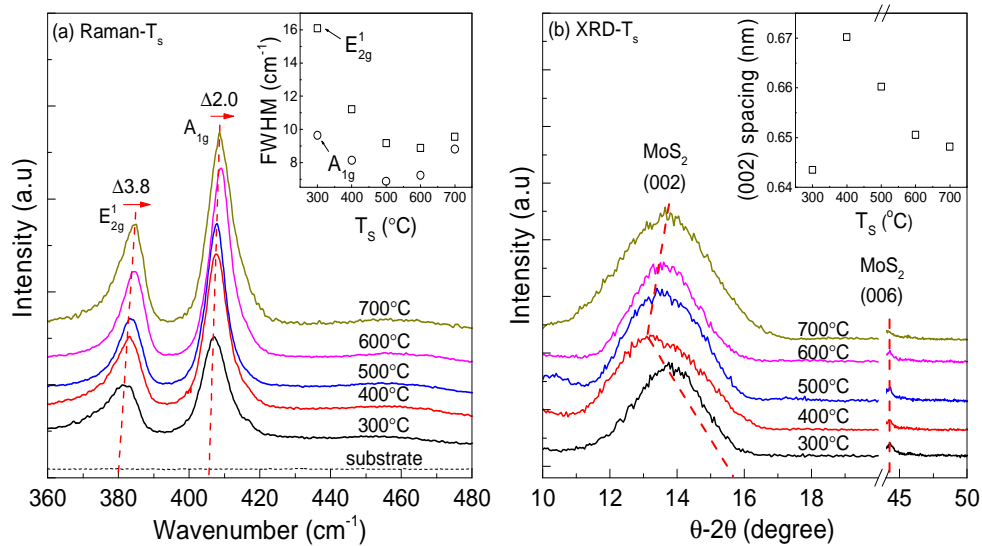


Figure 5-4 (a) Raman and (b) XRD spectra of MoS₂ films deposited at various T_s from 300 °C to 700 °C. Insets: FWHM of Raman peaks and lattice spacing of the (002) planes.

Furthermore, in order to improve the surface roughness and prevent cracking, ramp cooling was introduced to extend the time for annealing and reaction. The surface morphology images of as-deposited MoS₂ film with and without 3 °C/min ramp cooling upon completion of deposition were captured using AFM as shown in Figure 5-5. It shows that the film surface is smooth throughout all locations randomly selected on the film surfaces. The surface roughness Ra of substrate was determined to be 0.132 nm, while the surface roughness of naturally cooled sample is 0.182 nm. The film is slightly rougher than the bare substrate. The film with ramp cooling appears to have lower surface roughness of 0.128 nm, which is fairly close to that of the substrate. Therefore, it concludes that a more uniform MoS₂ film can be obtained by ramp cooling after deposition.

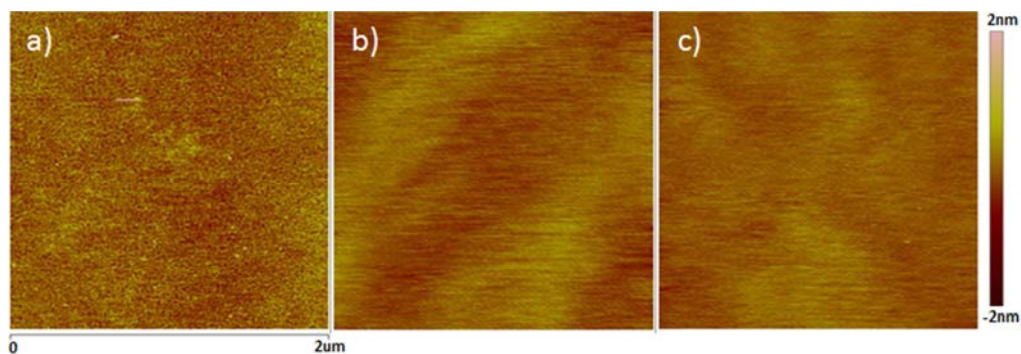


Figure 5-5 AFM image of a) substrate, b) MoS₂ film without ramping, and c) with ramping deposited at P_s=15 mTorr and T_s=500 °C.

5.2.3 Sputtering pressure

The sputtering pressure, P_s, was varied to obtain the best crystallization result of MoS₂ film. Figure 5-6a shows the Raman peaks and its FWHM of the films prepared at P_s varying from 5 mTorr to 25 mTorr. Note that the increase in P_s is accompanied by a small blue shift 1.4 cm⁻¹ for E_{2g}¹ and 1.0 cm⁻¹ for A_{1g}. This result may imply a change of internal stresses in the film^{80,81}. When a larger P_s is used in the deposition, scattering of particles in the chamber is more severe, such that the deposition rate is lowered and the deposited obtained in the specific deposition time is thinner. The effect of the substrate in generating the stresses would become more significant, such that a blue shift of the E_{2g}¹ and A_{1g} is resulted. In addition, we note that the minimum FWHM is detected for a film deposited at 15 mTorr, showing that crystallization is optimized at this deposition condition.

Direct evidence of crystallization of the MoS₂ films is achieved by referring to the θ -2 θ XRD spectra as shown in Figure 5-6b. The diffraction peaks associated only with c-planes of (002) and (006) are observed at 2 θ = 14.03° and 44.31°, respectively. This indicates that the MoS₂ planes are stacked in parallel. The

position of the (002) plane shifts towards the direction corresponding to a larger lattice spacing with increasing P_s . This may be due to the reduction of film thickness as well. Thickness and deposition rate of the film are further investigated by XRR in Figure 5-7. It shows that the thickness of film is in range of nanometer and is reduced from 6.267 nm to 2.486 nm with increasing P_s . Such a range corresponds to the thickness of 11 to 5 monolayers of MoS_2 . The deposition rate at 15 mTorr, which is the optimum condition, is about 0.108 nm/min. Hence the deposition time required for making a monolayer MoS_2 of 0.65 nm thick is estimated to be 6.5 min. We thereby came up with a suggested condition for producing monolayer MoS_2 by 9 % H_2S in Ar, $T_s = 500^\circ\text{C}$ with ramp cooling $3^\circ\text{C}/\text{min}$, $P_s = 15$ mTorr and deposition time of 6.5 min.

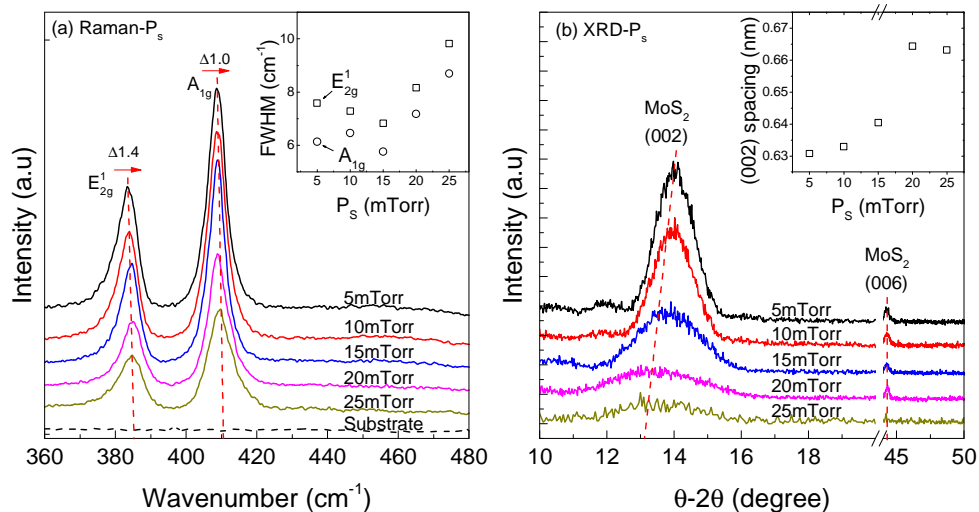


Figure 5-6 (a) Raman and (b) XRD spectra of MoS_2 films deposited at various P_s from 5 to 25 mtorr. Insets: FWHM of Raman peaks and lattice spacing of the (002) planes.



Figure 5-7 (a) XRR spectra and (b) deposition rate of MoS₂ films deposited at various P_s from 5 to 25 mtorr.

5.2.4 Reduction of deposition time for reducing film thickness

Based on the above experiences, the next step was targeted at achieving monolayer MoS₂ film. A direct approach is to reduce the film thickness by reducing deposition time. A series of MoS₂ films was then fabricated by setting the deposition time. The separation between the positions of the two E_{2g}¹ and A_{1g} Raman peaks can be used to indicate the thickness of MoS₂⁸². The peak separation is the smallest if the thickness reaches monolayer⁸³. Therefore, we applied this guideline for preliminary estimation of the film thickness possibly achieved in particular run.

Figure 5-8a shows the Raman spectra of the MoS₂ films with deposition time of 60, 30, 25 and 15 min. The separations of the two Raman peaks are 23.2, 20.6, 19.3 and 19.8cm⁻¹ respectively. We found that the film deposited for 25 min should be the thinnest and the closest thickness of monolayer MoS₂. The estimated deposition time for forming a monolayer MoS₂ film according to the deposition rate



is 6.5 min, which is much shorter than the one in practice. This discrepancy is attributed to the poor adhesion rate of landing species on a clean substrate surface, such that the deposition rate for producing monolayer film is low at the initial stage of deposition. When the deposition time shorter than 25 min is used, the film produced would appear to be discontinuous, in which the deposited material is aggregated into the form of nano-sized islands.

Another indirect evidence of the achievement of a monolayer MoS₂ film is obtained by observing the photoluminescence (PL) emission from the sample. The data are shown in Figure 5-8b. With decreasing deposition time and effectively film thickness, one sees the successive increase in PL intensity and also the increase in the emitted photon energy to ~1.9 eV. Note that the reported indirect bandgap energy of bulk MoS₂ is 1.2 eV. Film of deposition time of 25 min shows a strong PL peak at 1.91 eV, which is consistent with the expected direct bandgap energy of monolayer MoS₂ of 1.9 eV⁸⁴.

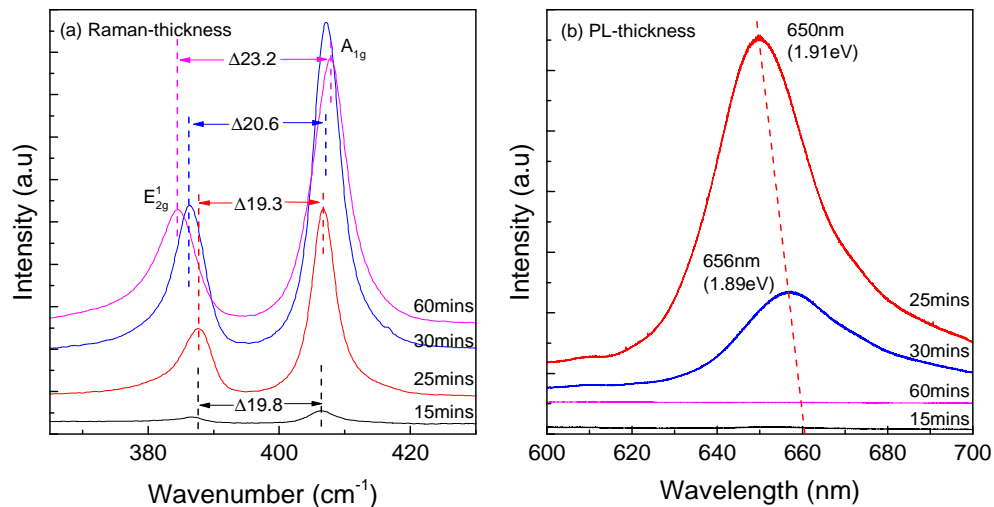
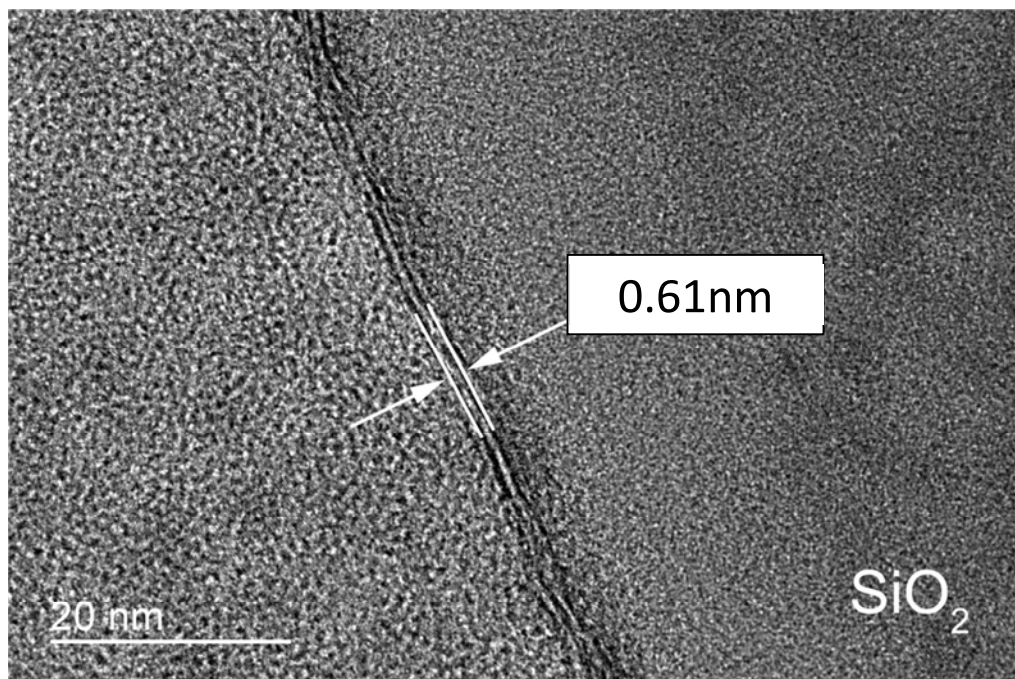


Figure 5-8 (a) Raman and (b) photoluminescence spectra of MoS₂ films deposited with various deposition times from 60min to 15 min at $C_{H_2S} = 9\%$, $T_s = 500\text{ }^\circ\text{C}$ and $P_s = 15\text{ mtorr}$.



The thickness of the MoS₂ film was also directly observed from the XS-TEM image as shown in Figure 5-9. The picture shows the interface between the substrate and the MoS₂ film which deposited for 25 min. A clear monolayer of MoS₂ with thickness about 0.61 nm can be observed at the interface. The corresponding energy dispersive spectroscopy (EDS) shown in Figure 5-10 also confirmed the relative contents of Mo and S are in a ratio of 1 to 2, which should be expected for the MoS₂ phase.

The photoconductivity response of different structured MoS₂ under above-bandgap UV illumination was examined. Results are shown in Figure 5-11. Only the monolayer MoS₂ film exhibits a strong response to the photo excitation. This signal is expected to come from the direct bandgap structure. In the gas sensing measurements, we selected to use the samples deposited for 25min and 60min, which are represented as monolayer and multilayer of MoS₂ films respectively.



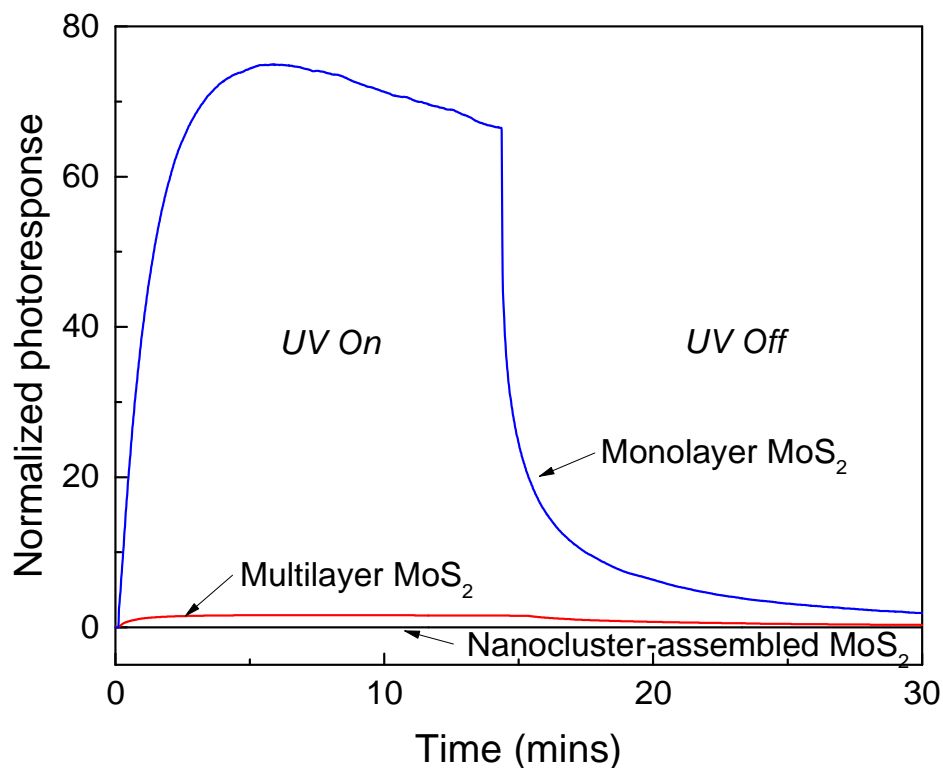


Figure 5-11 Normalized photoconductivity response of nanocluster, multilayer and monolayer MoS₂ measured at ambient condition.

5.3 Gas sensing properties of MoS₂ films

Resistive response of MoS₂ films of different microstructures and thicknesses against H₂S, NH₃ and H₂ were measured. The measurements were conducted at 80 °C. Both sensor responses at dark electrical conductance and above-bandgap UV light assisted photoconductivity were measured.

5.3.1 H₂S sensing properties of MoS₂ films

Figure 5-12 shows the results of the dark sensor response of H₂S in different groups of MoS₂.

Consider the results of nanocluster-assembled MoS₂ film first. The change of the dark electrical conductivity of the films against H₂S with concentration varying



over 30 ppm to 500 ppm is almost unchanged and stays at a level of sensor response about -0.25 %. On the other hand, the sensor response of multilayer MoS₂ films based on the change of dark electrical conductivity is positive and varies in a narrow range from about 0.34 % to 0.58 % for H₂S concentration covering the range from 40 ppm to 500 ppm. These two groups of samples show opposite sensor response to H₂S. To explain this difference, H₂S in these structures is suggested to be suffered from different detection mechanism. When sensor's surface adsorbed H₂S molecules, H₂S molecules are either be ionized into radicals or be reacted with adsorbed oxygen. The electrical conductivity of the prior activity decreases while the later one increases. Nanocluster-assembled MoS₂ film, which has high surface-to-volume ratio and number of adsorption site, is more readily for adsorbing H₂S and dissociate them into radicals. Surface of multilayer MoS₂ is almost fully occupied by oxygen and enhance the adsorbed H₂S is more readily for reacting with oxygen. Thus the sensor response in these two groups of samples is opposite.

On the other hand, the sensor response based on the change of dark electrical conductivity of monolayer MoS₂ film was found to increase from 1.25 % to 25.68 % with increasing H₂S concentration from 10 ppm to 500 ppm. Repeatability of the sensor response of monolayer MoS₂ film was examined by observing the output obtained from repeatedly exposing the sensor alternatively to H₂S with a concentration of 100 ppm and air. Data are shown in Figure 5-12d. The amplitude of the response of the detected gas is very stable throughout all the cycles in the test.

Monolayer MoS₂ film shows remarkable sensor response compared with nanocluster-assembled and multilayer MoS₂ films. The enhanced response should originate from the direct bandgap transition of monolayer MoS₂ film, as the charge



exchange with the surface adsorbed oxygen and H_2S is more effective and faster than indirect bandgap transition of bulk MoS_2 films. Thus, the large surface-to-volume ratio of nanocluster-assembled MoS_2 film or ultrathin multilayer MoS_2 film are not the most critical factor to attain stronger sensor response in MoS_2 species.

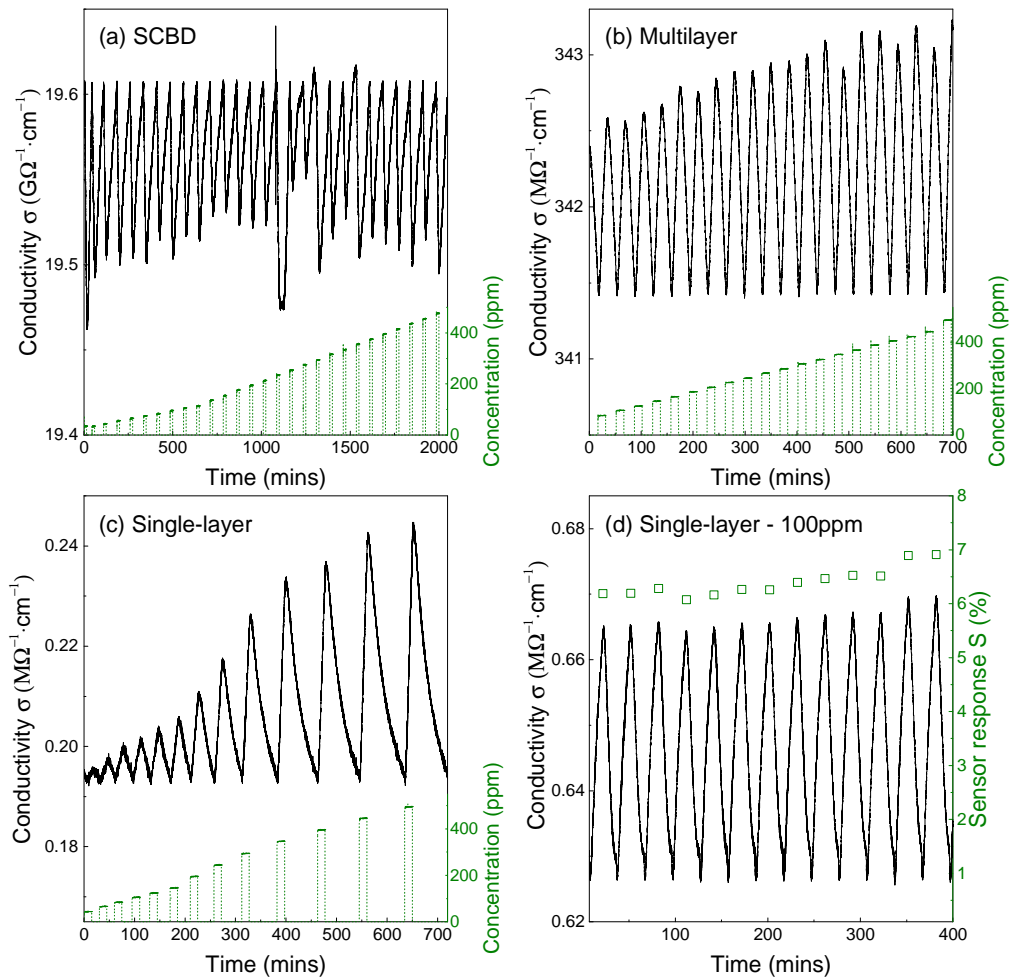


Figure 5-12 Dark electrical conductivity of (a) nanocluster-assembled MoS_2 film for 30 – 500 ppm H_2S (b) multilayer MoS_2 film for 40 – 500 ppm H_2S (c) monolayer MoS_2 for 10 – 500 ppm H_2S at 80 °C and (d) repeatability of the sensor response of monolayer MoS_2 against 100 ppm H_2S .

5.3.2 UV-assisted sensing of monolayer MoS_2

The synthesized monolayer MoS_2 film is found to have a direct bandgap



transition. It greatly facilitates photoexcitation of electron-hole pairs. In this part of test, the film was illuminated with above-bandgap UV light and used to detect H_2S , NH_3 and H_2 again. The data are shown in Figure 5-13. The sensor response was found to increase from 4.04 % to 52.07 % for H_2S concentration increased from 10 ppm to 500 ppm. The overall response is doubled to that obtained in dark. This result is attributed to the increase in adsorption site of oxygen and the increase in photo-assisted charge transfer between the adsorbed oxygen radicals and H_2S molecules (also see discussion presented in Section 2.3.3 of Chapter 2).

The sensor response of photo-assisted monolayer MoS_2 to NH_3 with the concentration varying from 10 ppm to 500 ppm is range from 53.8 % to 247.4 %. It is found to be prominently larger than that to H_2S . On the contrary, the sensor response to H_2 is found to be much smaller, which is about 0.4 % to 6.3 % in range of concentration from 40 ppm to 500 ppm.

Figure 5-14 summarizes the sensor response of nanocluster-assembled MoS_2 film, multilayer MoS_2 film, and monolayers MoS_2 film against H_2S in dark. The figure also shows the UV-assisted gas sensor response of monolayer MoS_2 film against H_2S , NH_3 and H_2 with the concentration covering a broad range. The monolayer MoS_2 film exhibits the stronger sensor response over the whole range of the gas concentration under investigation compared to those of the MoS_2 films having other types of structures. Monolayer MoS_2 film exhibits many advantages to be used for detecting H_2S . Other than having a strong sensor response, MoS_2 does not react with H_2S and hence is not easily poisoned by the gas. Furthermore, MoS_2 under UV illumination at ambient temperature is stable. One concern is the poor selectivity. It also gives strong response to NH_3 and could generate undesired

interference when it is used to detect H_2S with the presence of some amount of NH_3 . The problem of selectivity could be solved by some other means such as adding an appropriate catalyst into the sensor material for suppressing the unwanted interference.

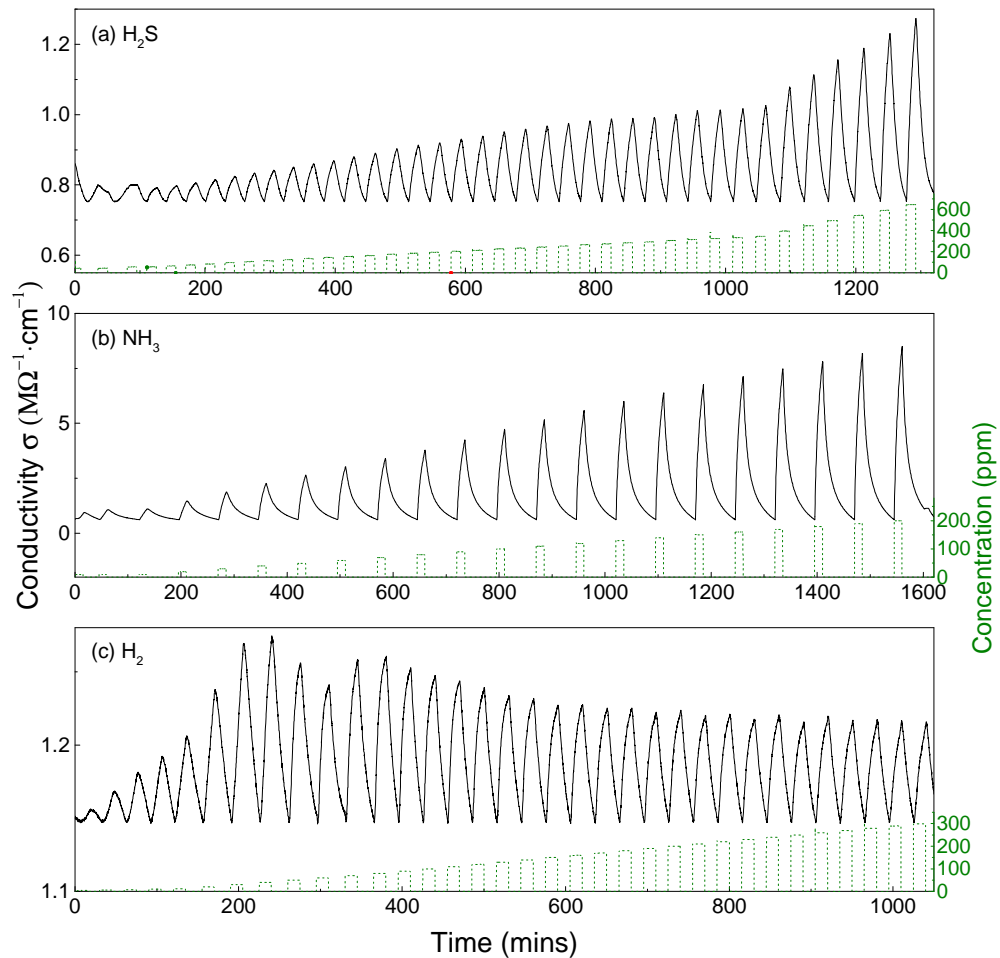


Figure 5-13 Photo-assisted electrical conductivity of monolayer MoS₂ for (a) 10 – 500 ppm H₂S at 80°C (b) 10 – 200 ppm NH₃ at 80 °C and (c) 40 – 2800 ppm H₂ at 80 °C.

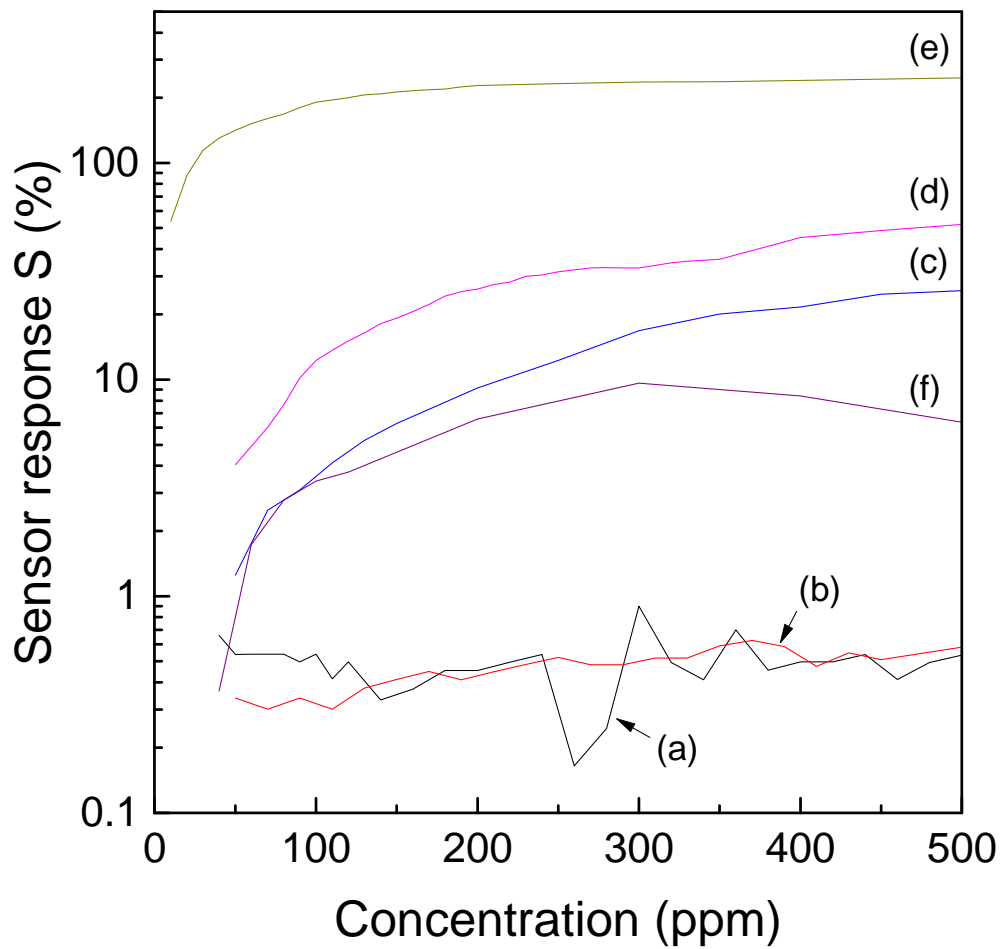


Figure 5-14 Dark sensor response of (a-c) nanocluster, multilayer, and monolayer MoS₂ films against H₂S, and (d-f) photo-assisted sensor response of monolayer MoS₂ film against H₂S, NH₃ and H₂ at 80 °C.



Chapter 6 Conclusion

6.1 Summary

The dynamic gas sensing mechanism and gas sensing properties of transition metal chalcogenides had been studied using two groups of materials, ZnSe and MoS₂. The correlation of adsorption and gas sensing mechanism was explained using a time dependent model based on the experimental results of the photo-assisted oxygen sensing of nanocluster-assembled SCBD ZnSe films. The model provides the ideal of gas sensing mechanism and the dependence of dynamic adsorption. On the other hand, the sensor response of monolayer MoS₂ against H₂S was determined. This part of study illustrates a new method for fabricating large-scale uniform monolayer MoS₂ film. Results were compared with the sensor response of multilayer MoS₂ film and nanocluster-assembled SCBD MoS₂ film. UV-assisted gas sensing performance of monolayer MoS₂ against H₂S, NH₃ and H₂ was also conducted.

6.1.1 Study of dynamic gas sensing model

Adsorption of gas, grain size effect and ionization are the main considerations for building up the model of gas sensing process. Development of a theoretical model is useful for explaining the relationship between the sensing mechanisms and output, as so to help in designing new gas sensor of improved performance. For the sake of simplicity, some limitations were made in the derivation for demonstrating the key principles. Photo illumination is applied for increasing the concentration of charge carriers such that the grain size effect originating from the



intergranular potential barrier can be manifested and be observed. In addition, this model only available in one type of detected gas. The change of sensor's conductance was deduced and the time-dependent photoconductivity was formulated with a function in form of:

$$\sigma = A_0 + A_1 e^{-k_r t} + A_2 e^{-k_A t}$$

The rate constants (k_r and k_A) and the coefficients (A_1 and A_2) contain the information on the mechanism of grain size effect, the type of adsorption mechanism, electron and hole mobility of sensor material, and ionization efficiency of the adsorbed gas molecules.

Nanocluster-assembled SCBD ZnSe films were chosen for this part of study because it has a direct bandgap and the potential of giving a strong gas sensor response. The diameter of nanoclusters composing the film structure is about 69.2 nm and the film thickness is about 145nm. Oxygen was used as the detected gas because it is readily adsorbed on the material surface and form radicals. Hence, the study of oxygen sensing effect would generate very rich information exploring the mechanisms involved in the related physiochemical processes.

For investigating the gas sensing mechanism, we measured the dynamic (time-dependent) photoconductivity immediately after turning on the light source, whereas the oxygen concentration was varied over a broad range. At room temperature, the data can be described by using a function containing a sum of two exponential functions. The saturated photo response decreased from 306 to 0.3 with increasing oxygen concentration from 0.01 % to 20 %. The sensor response exhibits a linear dependence on the oxygen concentration from 0.01 % to 0.2 %, with a sensitivity of 192 per 1 % change in gas concentration. We assert that the



recombination is controlled by necking effect at the intergranular region, which further affects the observed photoconductivity. The recombination rate constant in the function is associated with a potential barrier gain from the adsorbed gas molecules. Necking effect of sensor occurs in the range of gas concentration of 0.1 - 1 %. The pre-exponential recombination factor against the reciprocal of the recombination rate constant is constant, which related to the assumption of constant drift mobility of electrons and holes. Besides, the adsorption part of the model demonstrated the adsorption-desorption mechanism and ionization. Adsorption rate constant followed the trend of Langmuir and BET adsorption models, where the adsorption of the first gas layer was saturated at concentration 0.04 - 0.5 % and multilayer adsorption commences and dominates for higher gas concentration. The slope of pre-exponential adsorption factor to the reciprocal of adsorption rate constant describes the ionization process of adsorbed oxygen. The slope decreased at high oxygen concentration due to low adsorption energy of physisorbed oxygen. These observations demonstrated the dependence of adsorption-desorption mechanism on gas sensing mechanism.

The effect of thermal energy to the model was also determined. The gas sensing effect of the SCBD ZnSe films was measured at 80°C. A weaker photo-assisted gas sensor response in the range of 177.4 - 1.7 was observed for the oxygen concentration varying in the range of 0.02 - 10 %. The sensitivity at linear region was 161 in range of oxygen concentration of 0.02 - 0.2 %. The reason can also be explained by the rate constants and coefficients of the model. The amplitude of recombination and adsorption rate constants increased due to high phonon scattering and increase of desorption rate respectively. Observed from the



recombination part, neck control range increased to 0.1 - 2 %. The coefficient showed the increase of carrier and hole mobility factor because of reduction of ionized impurity scattering by thermal energy gain. From adsorption part, the first layer saturation range of adsorption increased to 0.2 - 2 %. Ionization factor increased due to the gain of ionization energy adsorbed oxygen from thermal energy. Integral of these phenomenon reduced the photoconductivity and resulted lower sensor response against oxygen at 80 °C.

The complete dynamic gas sensing model was, therefore, proved by experimental data with nanocluster-assembled ZnSe gas sensor detected with oxygen under UV illumination. A schematic of mechanism was illustrated to explain the model. It would be useful to estimate the sensor response before it is saturated, and determine the best gas sensing condition.

6.1.2 Gas sensing properties of MoS₂ film

In this part of study, we investigated the reducing gas sensing properties of large-area uniform monolayer MoS₂ film, multilayer MoS₂ film, and nanocluster-assembled SCBD MoS₂ film. The reducing gases to be detected include H₂S, NH₃ and H₂. The focus was put on finding the influences of the nano-scaled structural features and indirect-to-direct bandgap transition of MoS₂ films (as possessed by the three sample types) on the gas properties.

In particular, nanocluster-assembled MoS₂ was synthesized by SCBD. The diameter of nanoclusters is about 71.3 nm and the film is about 465 nm thick. The high porosity and surface-to-volume ratio was expected to have enhanced sensor response due to necking effect.



Monolayer and multilayer MoS₂ were found to be able to synthesize with a one-step reactive DC sputtering process on an IDE patterned SiO₂/Si substrate. The optimized sputtering condition was found to have reactant gas 9 % H₂S in Ar, substrate temperature of 500 °C with ramp cooling 3 °C/min and sputtering pressure of 15 mTorr. The deposition time of monolayer and multilayer MoS₂ were 25 min and 60 min respectively. The Raman spectrum, XS-TEM image and EDX spectrum verified the achievement of monolayer MoS₂ film structure. PL peak at 1.91 eV of monolayer MoS₂ showed that the transition of indirect-to-direct bandgap is clearly manifested.

The sensor response of the MoS₂ film samples against H₂S with concentration varying from 10 ppm to 500 ppm at 80 °C was measured. The nanocluster-assembled MoS₂ film samples showed very weak negative sign sensor response - 0.25 %. Besides, the multilayer MoS₂ film also showed very weak but positive sensor response in the range of 0.34 - 0.58 %. The opposed response of this two types of MoS₂ film is due to sensing mechanism dominated by ionization of adsorbed H₂S in the prior one or reaction with adsorbed oxygen in the later one. On the other hand, the monolayer MoS₂ film exhibits a notable sensor response from 1.25 % to 25.68 %. As a consequence, it is verified that the gas sensor response of MoS₂ can be greatly enhanced if its thickness is reduced to monolayer thick, where a transition to direct band structure occurs. The sensor response of monolayer MoS₂ film was also found to be highly repeatable in a cyclic test.

In addition, the gas sensing measurement was repeated with photo-assist on monolayer MoS₂ film. The sensor response was doubled at the same range of concentration and varied from 4.04 % to 52.07 %. It was also sensitive to NH₃ with



sensor response 53.8 % to 247.4 %. However, for H₂ detection, it is found to be much smaller, which is about 0.4 % to 6.3 %. In conclude, a remarkable enhanced sensor response against H₂S can be observed only in monolayer MoS₂ film. There is selectivity concern. It could be solved by some other means such as adding an appropriate catalyst into the sensor material for suppressing the unwanted interference.

6.2 Further work

According to the results achieved, further work in several aspects can be followed up in future. They include the attempts in improving the model for explaining the gas sensing effect, exploring the gas sensing properties of more other TMD materials and designing new gas sensors by using these materials.

6.2.1 Improvement of gas sensing model

The proposed model that describes the time-dependent conductance of photo-assisted gas sensor is restricted by some limitations and assumptions. This model could be further modified to make it more generally applicable. These limitations would be released by some ideas on other types of model:

(i) Limitation 1: The need of photo-assist

→ The intergranular potential barrier determined by the grain size effect can be determined by measuring the carrier mobility instead of photoconductivity. Photo-assist, which is in purpose of enhancing the effect to the conductivity change, will be no longer necessary. Thus the sensor response obtained from carrier mobility can be measured by Hall Effect measurements (e.g. Van der Pauw method).



(ii) Limitation 2: Only a one detected gas is involved

→ Sensor response to a gas mixture composed of more than one detected gas can be derived base on linearly superposition of individual response from the gas components. We anticipate that the model would become complicated since the reactions order among gases on the sensor's surface is unpredictable. Hence some additional assumptions would be required such as statistic models describing the chaos of reactions.

6.2.2 Gas sensing with other TMD material

The study on monolayer MoS₂ film illustrates an interesting example for attaining enhanced gas sensing properties accompanied by an indirect-to-direct bandgap transition when film thickness is reduced to monolayer thick. This sheds light on the possibility of finding more other ultrathin 2D TMD materials to exhibit similar gas sensing properties. For example, WS₂ is a potential candidate to be investigated. One possible explanation for this observation is that the electronic configuration of a transition metal may exhibit a change of valence state due to redistribution of electrons in the d-orbitals when electron band structure experiences a transition. More theoretical work can be done to analyze the correlation between the electron states of the element and sensor response using first principle calculation.

6.2.3 Design of gas sensor

Conventional gas sensors of improved properties can be achieved by using new materials of different compositions, surface morphology, or applying different



operation modes. Recalling from the adsorption mechanism, one expects that low adsorption sites density and excessive layers of coverage on the sensor's surface by oxygen is unfavorable for obtaining a strong gas sensor response of a reducing gas. The ideal condition for detecting reducing gas is to pre-adsorbed only one single layer of oxygen on the sensor's surface. This can be achieved by using more defective sensor's surface to increase the defect states, such as creating dangling bonds on the sensor's surface by etching. On the other hand, controlling the operation temperature or higher-power light beam-assist may alleviate the excessive layers of adsorption.



Reference

- [1] Seiyama, T.; Kato, A.; Fujiishi, K.; Nagatani, M. A New Detector for Gaseous Components Using Semiconductive Thin Films. *Analytical Chemistry* **1962**, *34* (11), 1502.
- [2] Neri, G. First fifty years of chemoresistive gas sensors. *Chemosensors* **2015**, *3* (1), 1.
- [3] Shaver, P. Activated tungsten oxide gas detectors. *Applied Physics Letters* **1967**, *11* (8), 255.
- [4] Yamazoe, N.; Kurokawa, Y.; Seiyama, T. Effects of additives on semiconductor gas sensors. *Sensors and Actuators* **1983**, *4*, 283.
- [5] Bochenkov, V.; Sergeev, G. Sensitivity, selectivity, and stability of gas-sensitive metal-oxide nanostructures. *Metal oxide nanostructures and their applications* **2010**, *3*, 31.
- [6] Wang, C.; Yin, L.; Zhang, L.; Xiang, D.; Gao, R. Metal oxide gas sensors: sensitivity and influencing factors. *Sensors* **2010**, *10* (3), 2088.
- [7] Korotcenkov, G. Metal oxides for solid-state gas sensors: What determines our choice? *Materials Science and Engineering: B* **2007**, *139* (1), 1.
- [8] Kurtin, S.; McGill, T.; Mead, C. Fundamental transition in the electronic nature of solids. *Physical Review Letters* **1969**, *22* (26), 1433.
- [9] Liu, H.; Gong, S.; Hu, Y.; Liu, J.; Zhou, D. Properties and mechanism study of SnO₂ nanocrystals for H₂S thick-film sensors. *Sensors and Actuators B: Chemical* **2009**, *140* (1), 190.
- [10] Zhu, C.; Chen, Y.; Wang, R.; Wang, L.; Cao, M.; Shi, X. Synthesis and enhanced ethanol sensing properties of α -Fe₂O₃/ZnO heteronanostructures. *Sensors and Actuators B: Chemical* **2009**, *140* (1), 185.
- [11] Barsan, N.; Weimar, U. Conduction model of metal oxide gas sensors. *Journal of Electroceramics* **2001**, *7* (3), 143.
- [12] Yamazoe, N. New approaches for improving semiconductor gas sensors. *Sensors and Actuators B: Chemical* **1991**, *5* (1-4), 7.
- [13] Xu, C.; Tamaki, J.; Miura, N.; Yamazoe, N. Grain size effects on gas sensitivity



- of porous SnO₂-based elements. *Sensors and Actuators B: Chemical* **1991**, *3* (2), 147.
- [14] Chadwick, A.; Geatches, R.; Wright, J. The effect of carbon monoxide and methane on the electrical conductivity of TiO₂ single crystals. *Philosophical Magazine A* **1991**, *64* (5), 999.
- [15] Morrison, S. R. Selectivity in semiconductor gas sensors. *Sensors and actuators* **1987**, *12* (4), 425.
- [16] Smulko, J. M.; Trawka, M.; Granqvist, C. G.; Ionescu, R.; Annanouch, F.; Llobet, E.; Kish, L. B. New approaches for improving selectivity and sensitivity of resistive gas sensors: a review. *Sensor Review* **2015**, *35* (4), 340.
- [17] Seiyama, T.; Futata, H.; Era, F.; Yamazoe, N. Gas detection by activated semiconductive sensor. *Denki Kagaku* **1972**, 244.
- [18] Lu, Y.; Li, J.; Han, J.; Ng, H.-T.; Binder, C.; Partridge, C.; Meyyappan, M. Room temperature methane detection using palladium loaded single-walled carbon nanotube sensors. *Chemical Physics Letters* **2004**, *391* (4), 344.
- [19] Wang, D.; Ma, Z.; Dai, S.; Liu, J.; Nie, Z.; Engelhard, M. H.; Huo, Q.; Wang, C.; Kou, R. Low-temperature synthesis of tunable mesoporous crystalline transition metal oxides and applications as Au catalyst supports. *The Journal of Physical Chemistry C* **2008**, *112* (35), 13499.
- [20] Bond, G. C.; Molloy, L. R.; Fuller, M. J. Oxidation of carbon monoxide over palladium–tin (IV) oxide catalysts: an example of spillover catalysis. *Journal of the Chemical Society, Chemical Communications* **1975**, (19), 796.
- [21] Harris, L. A titanium dioxide hydrogen detector. *Journal of the Electrochemical Society* **1980**, *127* (12), 2657.
- [22] Yamazoe, N.; Miura, N. Some basic aspects of semiconductor gas sensors. *Chemical sensor technology* **1992**, *4*, 19.
- [23] Lee, A. P.; Reedy, B. J. Temperature modulation in semiconductor gas sensing. *Sensors and Actuators B: Chemical* **1999**, *60* (1), 35.
- [24] Gupta, V.; Menon, R.; Sreenivas, K. Optoelectronic and Microelectronic Materials and Devices, 2008. COMMAD 2008. Conference on, 2008; p 55.
- [25] Peng, L.; Zhao, Q.; Wang, D.; Zhai, J.; Wang, P.; Pang, S.; Xie, T. Ultraviolet-



- assisted gas sensing: a potential formaldehyde detection approach at room temperature based on zinc oxide nanorods. *Sensors and Actuators B: Chemical* **2009**, *136* (1), 80.
- [26] Kobayashi, A.; Kawaji, S. Adsorption and Photoexcited Adsorption of Oxygen on Zinc Sulfide. *The Journal of Chemical Physics* **1956**, *24* (4), 907.
- [27] Fukutani, K.; Murata, Y. Photoexcited processes at metal and alloy surfaces: electronic structure and adsorption site. *Surface science* **1997**, *390* (1-3), 164.
- [28] Geng, Q.; He, Z.; Chen, X.; Dai, W.; Wang, X. Gas sensing property of ZnO under visible light irradiation at room temperature. *Sensors and Actuators B: Chemical* **2013**, *188*, 293.
- [29] Coldren, L. A.; Corzine, S. W.; Mashanovitch, M. L. *Diode lasers and photonic integrated circuits*; John Wiley & Sons, 2012.
- [30] Lantto, V.; Romplainen, P.; Leppävuori, S. A study of the temperature dependence of the barrier energy in porous tin dioxide. *Sensors and Actuators* **1988**, *14* (2), 149.
- [31] Rothschild, A.; Komem, Y. The effect of grain size on the sensitivity of nanocrystalline metal-oxide gas sensors. *Journal of Applied Physics* **2004**, *95* (11), 6374.
- [32] Bonasewicz, P.; Hirschwald, W.; Neumann, G. Influence of surface processes on electrical, photochemical, and thermodynamical properties of zinc oxide films. *Journal of the Electrochemical Society* **1986**, *133* (11), 2270.
- [33] Madel, M.; Huber, F.; Mueller, R.; Amann, B.; Dickel, M.; Xie, Y.; Thonke, K. Persistent photoconductivity in ZnO nanowires: Influence of oxygen and argon ambient. *Journal of Applied Physics* **2017**, *121* (12), 124301.
- [34] Clifford, P. K.; Seiyama, T. In *Proc. Int. Meet. on Chemical Sensors* Fukuoka, Japan, 1983.
- [35] Thomas, J. M. The existence of endothermic adsorption. *J. Chem. Educ* **1961**, *38* (3), 138.
- [36] Foo, K.; Hameed, B. Insights into the modeling of adsorption isotherm systems. *Chemical Engineering Journal* **2010**, *156* (1), 2.



- [37] Henry, W. Experiments on the quantity of gases absorbed by water, at different temperatures, and under different pressures. *Philosophical Transactions of the Royal Society of London* **1803**, 93, 29.
- [38] Freundlich, H. Über die adsorption in lösungen. *Zeitschrift für physikalische Chemie* **1907**, 57 (1), 385.
- [39] Dubinin, M. The potential theory of adsorption of gases and vapors for adsorbents with energetically nonuniform surfaces. *Chemical Reviews* **1960**, 60 (2), 235.
- [40] Polanyi, M. Neuere über adsorption und ursache der adsorptionskräfte. *Berichte der Bunsengesellschaft für physikalische Chemie* **1920**, 26 (17-18), 370.
- [41] Langmuir, I. The evaporation, condensation and reflection of molecules and the mechanism of adsorption. *Physical Review* **1916**, 8 (2), 149.
- [42] Brunauer, S.; Emmett, P. H.; Teller, E. Adsorption of gases in multimolecular layers. *Journal of the American chemical society* **1938**, 60 (2), 309.
- [43] Zhang, X.; Ji, W.; Tang, S. Determination of optical nonlinearities and carrier lifetime in ZnO. *JOSA B* **1997**, 14 (8), 1951.
- [44] Wang, H.; Zhang, C.; Rana, F. Surface recombination limited lifetimes of photoexcited carriers in few-layer transition metal dichalcogenide MoS₂. *Nano Lett.* **2015**, 15 (12), 8204.
- [45] Dolui, K.; Rungger, I.; Sanvito, S. Origin of the n-type and p-type conductivity of MoS₂ monolayers on a SiO₂ substrate. *Physical review B* **2013**, 87 (16), 165402.
- [46] Singh, S. K.; Neek-Amal, M.; Costamagna, S.; Peeters, F. Rippling, buckling, and melting of single-and multilayer MoS₂. *Phys. Rev. B* **2015**, 91 (1), 014101.
- [47] Park, S.; An, S.; Ko, H.; Lee, C. Effects of annealing on the photoluminescence of ZnSe nanorods coated with Au. *Materials Chemistry and Physics* **2014**, 143 (2), 735.
- [48] Mirov, S. B.; Fedorov, V.; Graham, K.; Moskalev, I.; Badikov, V.; Panyutin, V. Erbium fiber laser-pumped continuous-wave microchip Cr²⁺: ZnS and Cr



- 2+: ZnSe lasers. *Optics letters* **2002**, 27 (11), 909.
- [49] Chang, S.-J.; Su, Y.-K.; Chen, W.; Chen, J.-F.; Lan, W.-H.; Lin, W.-J.; Cherng, Y.; Liu, C.-H.; Liaw, U. ZnSTeSe metal-semiconductor-metal photodetectors. *IEEE Photonics Technology Letters* **2002**, 14 (2), 188.
- [50] Tomashyk, V.; Feychuk, P.; Shcherbak, L. *Ternary alloys based on II-VI semiconductor compounds*; CRC Press, 2013.
- [51] Park, S.; Kim, S.; Lee, W. I.; Kim, K.-K.; Lee, C. Room temperature, ppb-level NO₂ gas sensing of multiple-networked ZnSe nanowire sensors under UV illumination. *Beilstein journal of nanotechnology* **2014**, 5, 1836.
- [52] Radisavljevic, B.; Kis, A. Mobility engineering and a metal–insulator transition in monolayer MoS₂. *Nat Mater* **2013**, 12 (9), 815.
- [53] RadisavljevicB; RadenovicA; BrivioJ; GiacomettiV; KisA. Single-layer MoS₂ transistors. *Nat Nano* **2011**, 6 (3), 147.
- [54] Shih, C.-J.; Wang, Q. H.; Son, Y.; Jin, Z.; Blankschtein, D.; Strano, M. S. Tuning On–Off Current Ratio and Field-Effect Mobility in a MoS₂–Graphene Heterostructure via Schottky Barrier Modulation. *ACS Nano* **2014**, 8 (6), 5790.
- [55] Li, X.; Zhu, H. Two-dimensional MoS₂: Properties, preparation, and applications. *Journal of Materiomics* **2015**, 1 (1), 33.
- [56] Wang, Q. H.; Kalantar-Zadeh, K.; Kis, A.; Coleman, J. N.; Strano, M. S. Electronics and optoelectronics of two-dimensional transition metal dichalcogenides. *Nat Nano* **2012**, 7 (11), 699.
- [57] Lopez-Sanchez, O.; Lembke, D.; Kayci, M.; Radenovic, A.; Kis, A. Ultrasensitive photodetectors based on monolayer MoS₂. *Nat Nano* **2013**, 8 (7), 497.
- [58] Huang, Y.; Guo, J.; Kang, Y.; Ai, Y.; Li, C. M. Two dimensional atomically thin MoS₂ nanosheets and their sensing applications. *Nanoscale* **2015**, 7 (46), 19358.
- [59] Coleman, J. N.; Lotya, M.; O’Neill, A.; Bergin, S. D.; King, P. J.; Khan, U.; Young, K.; Gaucher, A.; De, S.; Smith, R. J. et al. Two-Dimensional Nanosheets Produced by Liquid Exfoliation of Layered Materials. *Science* **2011**, 331



- (6017), 568.
- [60] Eda, G.; Yamaguchi, H.; Voiry, D.; Fujita, T.; Chen, M.; Chhowalla, M. Photoluminescence from Chemically Exfoliated MoS₂. *Nano Letters* **2011**, *11* (12), 5111.
- [61] Lee, Y. H.; Zhang, X. Q.; Zhang, W.; Chang, M. T.; Lin, C. T.; Chang, K. D.; Yu, Y. C.; Wang, J. T.; Chang, C. S.; Li, L. J. et al. Synthesis of large-area MoS₂ atomic layers with chemical vapor deposition. *Adv Mater* **2012**, *24* (17), 2320.
- [62] Lee, Y.; Lee, J.; Bark, H.; Oh, I. K.; Ryu, G. H.; Lee, Z.; Kim, H.; Cho, J. H.; Ahn, J. H.; Lee, C. Synthesis of wafer-scale uniform molybdenum disulfide films with control over the layer number using a gas phase sulfur precursor. *Nanoscale* **2014**, *6* (5), 2821.
- [63] Ho, Y. T.; Yen, T. C.; Luong, T. T.; Wei, L. L.; Tu, Y. Y.; Chu, Y. C.; Hsu, H. R.; Chang, E. Y. 2016 China Semiconductor Technology International Conference (CSTIC), 2016; p 1.
- [64] Hussain, S.; Singh, J.; Vikraman, D.; Singh, A. K.; Iqbal, M. Z.; Khan, M. F.; Kumar, P.; Choi, D. C.; Song, W.; An, K. S. et al. Large-area, continuous and high electrical performances of bilayer to few layers MoS₂ fabricated by RF sputtering via post-deposition annealing method. *Sci Rep* **2016**, *6*, 30791.
- [65] Xiongfei, S.; Wu, Z.; Hu, X.; Shijin, D.; Peng, Z.; Wenzhong, B.; David Wei, Z. A novel synthesis method for large-area MoS₂ film with improved electrical contact. *2D Materials* **2017**, *4* (2), 025051.
- [66] Tao, J.; Chai, J.; Lu, X.; Wong, L. M.; Wong, T. I.; Pan, J.; Xiong, Q.; Chi, D.; Wang, S. Growth of wafer-scale MoS₂ monolayer by magnetron sputtering. *Nanoscale* **2015**, *7* (6), 2497.
- [67] Novoselov, K. S.; Jiang, D.; Schedin, F.; Booth, T. J.; Khotkevich, V. V.; Morozov, S. V.; Geim, A. K. Two-dimensional atomic crystals. *Proc Natl Acad Sci U S A* **2005**, *102* (30), 10451.
- [68] Yang, W.; Gan, L.; Li, H.; Zhai, T. Two-dimensional layered nanomaterials for gas-sensing applications. *Inorganic Chemistry Frontiers* **2016**, *3* (4), 433.
- [69] Miremedi, B. K.; Singh, R. C.; Morrison, S. R.; Colbow, K. A highly sensitive and selective hydrogen gas sensor from thick oriented films of MoS₂.



- Applied Physics A* **1996**, 63 (3), 271.
- [70] Late, D. J.; Huang, Y.-K.; Liu, B.; Acharya, J.; Shirodkar, S. N.; Luo, J.; Yan, A.; Charles, D.; Waghmare, U. V.; Dravid, V. P. et al. Sensing Behavior of Atomically Thin-Layered MoS₂ Transistors. *ACS Nano* **2013**, 7 (6), 4879.
- [71] Cho, B.; Hahm, M. G.; Choi, M.; Yoon, J.; Kim, A. R.; Lee, Y.-J.; Park, S.-G.; Kwon, J.-D.; Kim, C. S.; Song, M. et al. Charge-transfer-based Gas Sensing Using Atomic-layer MoS₂. *Scientific reports* **2015**, 5, 8052.
- [72] Perkins, F. K.; Friedman, A. L.; Cobas, E.; Campbell, P. M.; Jernigan, G. G.; Jonker, B. T. Chemical Vapor Sensing with Monolayer MoS₂. *Nano Letters* **2013**, 13 (2), 668.
- [73] Garcia, V.; Nair, M.; Nair, P. Formation of a ZnSe: heterostructure by air annealing ZnSe-In thin film. *Semicond. Sci. Tech.* **1999**, 14 (4), 366.
- [74] Tauc, J. Optical properties and electronic structure of amorphous Ge and Si. *Materials Research Bulletin* **1968**, 3 (1), 37.
- [75] Zhao, M.; Huang, J.; Wong, M.; Tang, Y.; Ong, C. Versatile computer-controlled system for characterization of gas sensing materials. *Review of scientific instruments* **2011**, 82 (10), 105001.
- [76] Seiyama, T.; Kagawa, S. Study on a Detector for Gaseous Components Using Semiconductive Thin Films. *Analytical chemistry* **1966**, 38 (8), 1069.
- [77] Kierlik, E.; Monson, P.; Rosinberg, M.; Sarkisov, L.; Tarjus, G. Capillary condensation in disordered porous materials: Hysteresis versus equilibrium behavior. *Physical review letters* **2001**, 87 (5), 055701.
- [78] Milani, P.; Barborini, E.; Piseri, P.; Bottani, C. E.; Ferrari, A. C.; Li Bassi, A. Nanostructured carbon films from supersonic cluster beam deposition: structure and morphology. *The European Physical Journal D - Atomic, Molecular, Optical and Plasma Physics* **1999**, 9 (1), 63.
- [79] Repetto, P., Università degli Studi di Genova, 2008.
- [80] Materne, A.; Moriceau, H.; Blanchard, B.; Florestan, J. Changes in stress and coercivity after annealing of amorphous Co (Zr, Nb) thin films deposited by RF sputtering. *IEEE transactions on magnetics* **1988**, 24 (2), 1752.
- [81] Zywitzki, O.; Hoetzsch, G.; Fietzke, F.; Goedicke, K. Effect of the substrate



- temperature on the structure and properties of Al₂O₃ layers reactively deposited by pulsed magnetron sputtering. *Surface and Coatings Technology* **1996**, *82* (1-2), 169.
- [82] Zhang, X.; Qiao, X.-F.; Shi, W.; Wu, J.-B.; Jiang, D.-S.; Tan, P.-H. Phonon and Raman scattering of two-dimensional transition metal dichalcogenides from monolayer, multilayer to bulk material. *Chemical Society Reviews* **2015**, *44* (9), 2757.
- [83] Zhan, Y.; Liu, Z.; Najmaei, S.; Ajayan, P. M.; Lou, J. Large-area vapor-phase growth and characterization of MoS₂ atomic layers on a SiO₂ substrate. *Small* **2012**, *8* (7), 966.
- [84] Splendiani, A.; Sun, L.; Zhang, Y.; Li, T.; Kim, J.; Chim, C.-Y.; Galli, G.; Wang, F. Emerging photoluminescence in monolayer MoS₂. *Nano letters* **2010**, *10* (4), 1271.